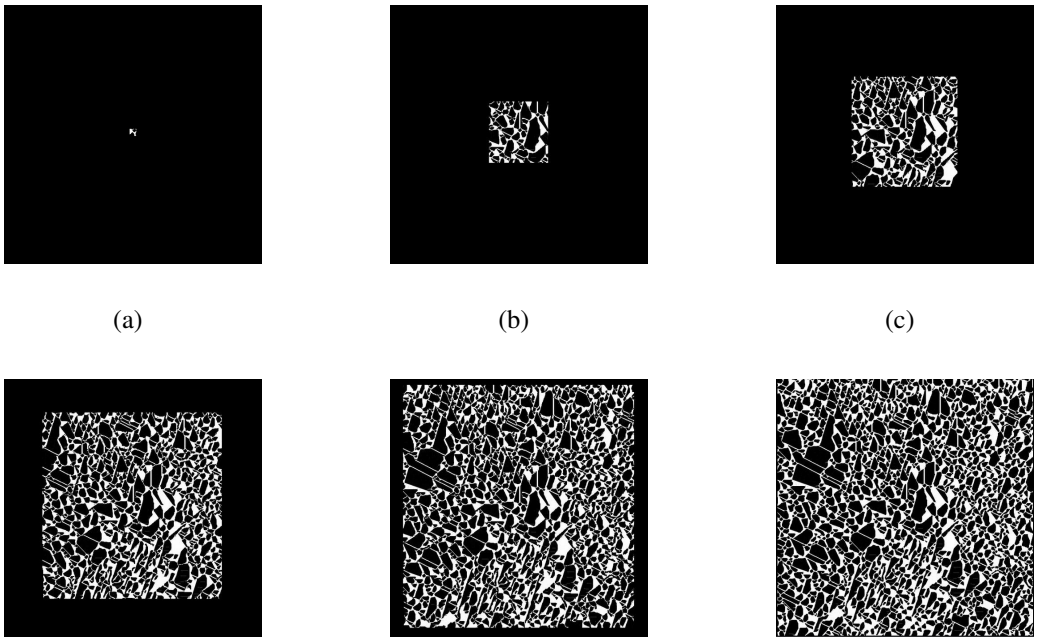

(a) (b) (c)

(d) (e) (f)

Figure 4.4: Various iterations of the sampling scheme described in Section 4.1.2. The algorithm initiates at the center of the synthetic microstructure, building outward layer by layer.

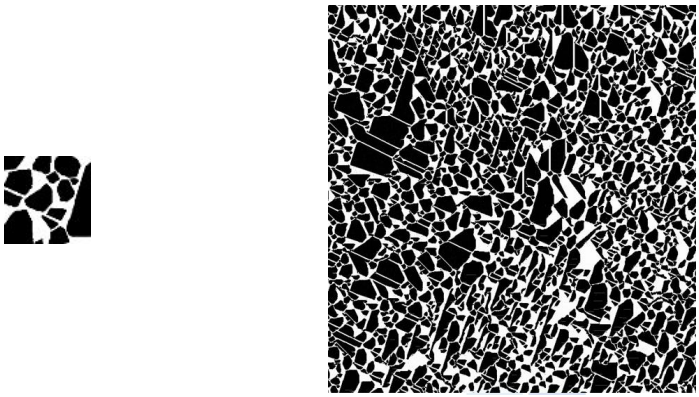

Figure 4.5: Input 64^2 seed image(left) with a height of $0.5mm$ compared to final synthetic 640^2 microstructure(right) with a height of $5.0mm$. Figures are not to scale.

In order to test the physical features and properties of the synthesized microstructure, the following criteria are considered:

- The synthetic microstructure must 'look like' the seed image; e.g grain size/shape

distribution.

- Physical properties of the synthetic microstructure such as volume fraction/density must be within reasonable bounds to the properties of the original microstructure.

It is clear from Figure 4.6 that the first criteria is met. Multiple cuts from the synthetic microstructure are compared with the seed image show in the center. Distinct features, such as HMX particle size and orientation are well captured. In fact, it it may be difficult to distinguish the seed image from the synthetic cuts. For the second criteria, the synthetic microstructure has a volume fraction of approximately $\eta = 0.63$ corresponding to the fraction of the seed image. The volume fraction is adjusted to better capture the material systems studied in this work. For instance, a volume fraction of $\eta = 0.93$ is required to reach the bulk density of PBX 9501 ($\rho = 1.844 g/cm^3$) given the reference densities for HMX and binder reported on 3.1. The aim of this work is to study the effects of the microstructure on shock loading of PBXs; therefore, three volume fractions are considered. These microstructures are plotted on Figures 4.7(a)- 4.7(c)below, where the image is inverted for visualization purposes. The lowest fraction $\eta = 0.75$ is shown on Figure 4.7(a) corresponding to bulk density of $\rho = 1.73 g/cm^3$. The volume fraction is increased to $\eta = 0.85$, shown on Figure 4.7(b) corresponding to bulk density of $\rho = 1.80 g/cm^3$. Finally a fraction of $\eta = 0.95$, shown on Figure 4.7(c) corresponding to bulk density of $\rho = 1.86 g/cm^3$. The bulk density of PBX 9501 is captured between $\eta = 0.85 - 0.95$. In this treatment, it is assumed that all microstructures produce a bulk density of of PBX 9501; therefore reference densities are made to be $\rho = 1.844 g/cm^3$.

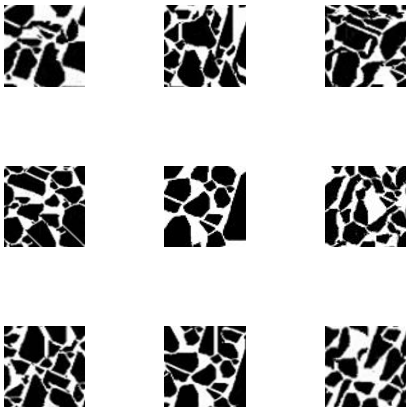

Figure 4.6: Seed image (center) compared with various cuts of synthetic microstructure

(a) $\eta = 0.75$

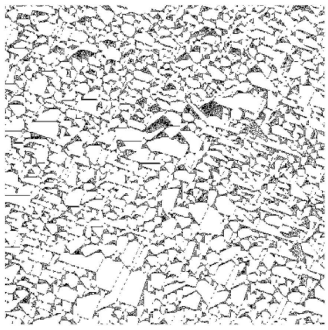

(b) $\eta = 0.85$

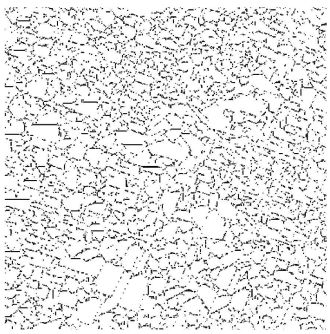

(c) $\eta = 0.95$

Figure 4.7: Synthetic microstructures at various mass fractions. Images are inverted for visualization purposes, where white pixels represent HMX and black pixels represent binder.

Similarly, the process is repeated to generate a 3D microstructure using the algorithm described in Section 4.1.3. However, in this case the synthetic microstucture size is not increased. The final size 64^3 corresponds to a length of the original seed image $0.5mm$. The length scale is fixed due to computational cost of both generating the synthetic microstructure and fidelity required for shock loading of the sample. The final synthetic sample is shown on Figures 4.8(a) and 4.8(b). The first Figure shows the outside surfaces of the volume element with a quarter cut, showing the variability within the micorstructure. Again, the microstructural features are well captured. Figure 4.8(b) shows the Iso-surfaces of HMX crystals.

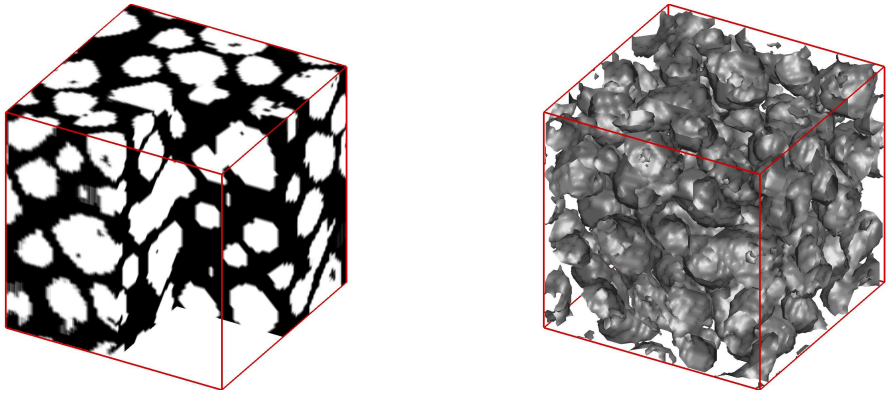

(a) (b)

Figure 4.8: 3D synthetic microstructures generated using the algorithm described in Section 4.1.3. Image are inverted for visualization purposes, where white pixels represent HMX and black pixels represent binder. Iso-surfaces(b) plotted show 3D HMX crystals.

4.2 Initial Shock Loading

This section considers shock loading of various material systems. Initiation of shock loading is not trivial; heterogeneous material systems have different responses for the same initiation conditions. The goal here is to compare material responses of continuum model to heterogeneous materials (synthetic microstructures); therefore, the average material response is considered. Here, the input parameters are density ρ and specific total energy E. These input parameters are uniformly distributed within a designated space within the material system. The output is measured in volume averages of pressure and temperature. All sample material systems are $5.0mm \times 5.0mm$ in area.

A $r = 1.0mm$ hot spot located at the center of the sample is considered. This loading condition is shown on Figure 4.9, where density and energy are uniformly distributed

within the hotspot. Outside the hotspot, the material is at inert reference conditions where $\rho = \rho_0$ and $E = 0.0(Mbar - cm^3/g)$. This produces a "hot" volume ratio of $V_{hot}/V = 12.56\%$. This loading condition is henceforth known as C_1. Similarly, C_2 shown on Figure 4.10(a) is a $r = 0.75mm$ hot spot located at the center of the sample. This loading condition produces a "hot" volume ratio of $V_{hot}/V = 7.06\%$ a decrease from the previous loading condition. A binary loading condition, B_y is considered to study the interaction of two hotspots and is shown on Figure 4.10(b). These hotspots have radii of $r_1 = 0.45mm$ and $r_2 = 0.55mm$ located at $O_1 = [0.42, 0.42]mm$ and $O_2 = [-0.50, 0.00]mm$ respectively. The binary loading condition produces a "hot" volume ratio $V_{hot}/V = 6.34\%$ near half of C_1 and near C_2. The final loading condition considered is 100 randomly distributed(uniform) hotspots of $r = 0.10mm$. This loading condition, appropriately named R_m, produces a "hot" volume ratio $V_{hot}/V = 10.95\%$ close the initial loading condition.

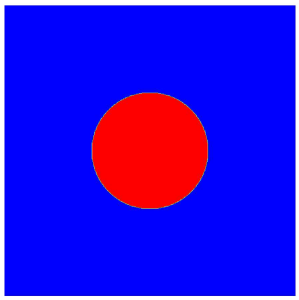

Figure 4.9: C_1: A $r = 1.0mm$ hot spot with uniformly distributed density and energy, producing a "hot" volume ratio of $V_{hot}/V = 12.56\%$.

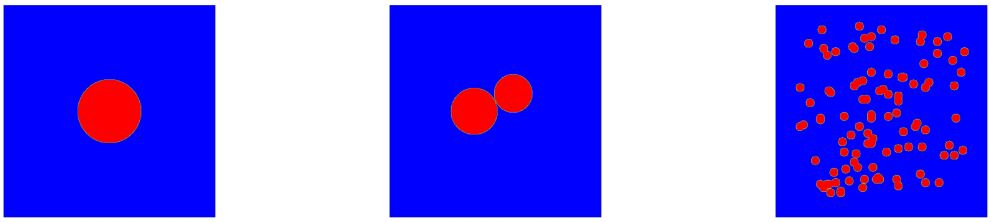

(a) C_2:$V_{hot}/V = 7.06\%$ (b) B_y:$V_{hot}/V = 6.34\%$ (c) R_m:$V_{hot}/V = 10.95\%$

Figure 4.10: Various loading conditions, where density and energy are uniformly distributed within hot(red) regions.

Next, density and total specific energy is varied to study the effects on average pressure and temperature over the entire domain. The effects are studied for each loading condition and for each material system, starting with the continuum model. This work specifically considers regimes where detonation occurs; therefore, sufficiently high average pressures and temperatures are needed. However, great care must be used when selecting the appropriate target average values. When selecting input densities and energies, prohibitively high local pressures and temperatures may be produced. The material Hugoniots described in Section 3.2.1 must be considered. Detonation occurs in flat-topped shock experiments above $2GPa$, therefore the target values are $P_{avg} = 5GPa$ and $T_{avg} = 500K$ are considered in this work. These conditions are sufficient to cause chemical reaction.

4.2.1 Initial Conditions: Continuum

This section considers initiation of a continuum material system where material properties are constant spatially. Specifically, PBX9501 is considered, where 95% of the material is HMX and the remaining is polymeric binder. Each of the components are not explicitly modeled, and the effects of the composite material system are incorporated into the empirical constants within the equations of state. To find the average target values of $P_{avg} = 5GPa$ and $T_{avg} = 500K$ a wide search is performed. Density is varied from $\rho = 1.844 - 3.0\, g/cm^3$ and specific total energy is varied from $E = 0.0 - 0.1\, Mbar - cm^3/g$, where the lower bounds produce the ambient conditions of $P_0 = 0.0GPa$ and $T_0 = 295K$. Since material properties are invariant spatially the average values produced by the input pressure density and energy can be found using volume fractions; i.e.

$$P_{avg} = P(V_{hot}/V) + P_0(1 - V_{hot}/V) \tag{4.6}$$

$$T_{avg} = T(V_{hot}/V) + T_0(1 - V_{hot}/V) \tag{4.7}$$

where the volume ratio V_{hot}/V varies by loading condition. The values of local pressure and temperature(P,T) are found from Equations 2.7-2.9, where the material is a pure solid. It is only necessary to calculate the local pressures and temperatures once, since they are uniform within the hot volume. Results for average pressure and temperature for the continuum are reported for all loading conditions on Figures 4.11(a)-4.14(c). Each figure shows the loading condition (a), the average pressure (b) and the average temperature (c). Average pressure and temperature are represented by contour plots where the x-axis is density and the y-axis is specific energy; for an input density and energy a corresponding average pressure/temperature over the entire domain is represented by the contour map. Although the

average target values of $P_{avg} = 5GPa$ and $T_{avg} = 500K$ are considered in this work, these plots can be used in future work to find other desired average values. Furthermore, optimization techniques can be implemented to find the desired average values by minimizing the difference between the desired values and Equations 4.6-4.7.

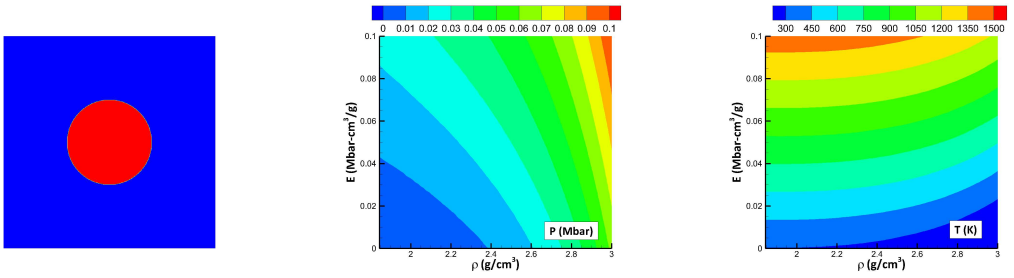

(a) Loading condition: C_1 (b) Average pressure (c) Average temperature

Figure 4.11: Average pressure P_{avg}(b) and temperature T_{avg}(c) contours for the continuum subjected to C_1 loading condition. The input density(x-axis) and energy(y-axis) produce the corresponding average value(contour) over the entire domain.

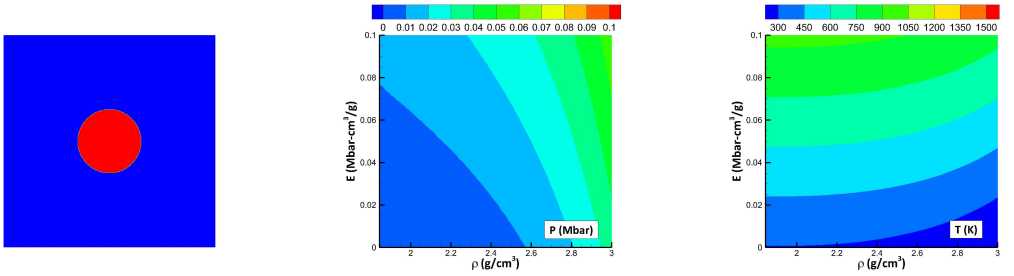

(a) Loading condition: C_2 (b) Average pressure (c) Average temperature

Figure 4.12: Average pressure P_{avg}(b) and temperature T_{avg}(c) contours for the continuum subjected to C_2 loading condition. The input density(x-axis) and energy(y-axis) produce the corresponding average value(contour) over the entire domain.

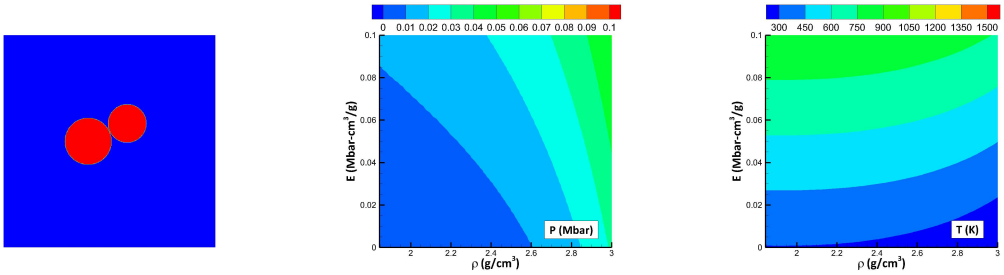

(a) Loading Condition: B_y (b) Average pressure (c) Average temperature

Figure 4.13: Average pressure P_{avg}(b) and temperature T_{avg}(c) contours for the continuum subjected to B_y loading condition. The input density(x-axis) and energy(y-axis) produce the corresponding average value(contour) over the entire domain.

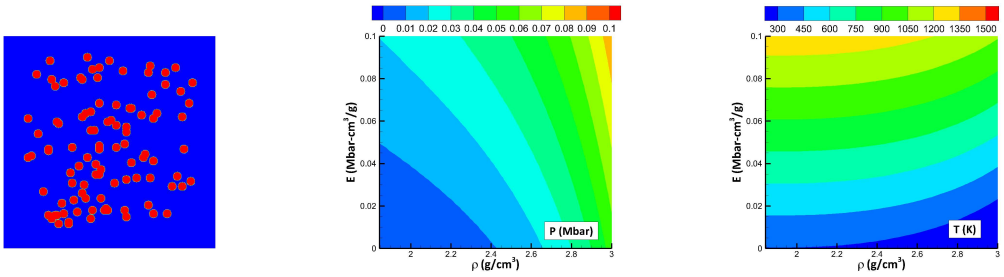

(a) Loading condition: R_M (b) Average pressure (c) Average temperature

Figure 4.14: Average pressure P_{avg}(b) and temperature T_{avg}(c) contours for the continuum subjected to R_m loading condition. The input density(x-axis) and energy(y-axis) produce the corresponding average value(contour) over the entire domain.

To further study these contours and the effects of loading conditions on the continuum material system, a 45° cut is taken across each contour. The cut is take from $[1.844, 0.0]$ to $[3.0, 0.1]$ in density-energy space. Although these plots may not lead to the desired average values, they are important in understanding the response of the material system. Figure 4.15(a) shows pressure slices of contours from Figures 4.11(b) 4.12(b) 4.13(b) 4.14(b), where the x-axis represents energy per unit volume (ρE) and the y-axis represents the corresponding average pressure in $Mbar$. For all loading conditions, trends initiate from the ambient condition ($P = P_0$) and pressure increases with energy per unit volume. The rate at which pressure changes, increases with energy. As energy increases, the first loading condition C_1 requires the least amount of energy per unit volume to produce any pressure when compared to all other loading conditions. The binary condition B_y, on the other hand, requires the most. Intuitively, this makes sense as the hot volume for C_1 is almost

twice as much as the hot volume of B_y; i.e. $V_{hot}/V = 12.54$ to $V_{hot}/V = 6.34$ respectively. As an example, for an energy per unit volume value of $\rho E = 0.2Mbar - cm^3/g$ loading condition C_1 produces $P_{avg} \approx 0.60Mbar$ while the loading condition B_y produces a $P_{avg} \approx 0.20Mbar$, a substantial difference. In other words, it takes more input energy per unit volume into the binary loading condition due to the percentage of hot volume. The other loading conditions fall in between these two extremes. However, the C_1 and R_m loading conditions exhibit similar behavior. This is due to their similar percentages of hot volume; i.e. $V_{hot}/V = 12.54$ to $V_{hot}/V = 10.95$. Similarity, the C_2 and B_y loading conditions follow the same trends due to their corresponding percentages of hot volume.

For the temperature profiles shown on Figure 4.15(b), similar observations are made. For all loading conditions, trends initiate from the ambient condition ($T = T_0$) and Temperature increases with energy per unit volume. However, the rate at which temperature changes decreases with energy; i.e. temperature plateaus, unlike pressure. Again, the loading condition C_1 requires the least amount of energy per unit volume while the binary condition B_y, requires the most. As an example, for an energy per unit volume value of $\rho E = 0.2Mbar - cm^3/g$ loading condition C_1 produces $T_{avg} \approx 1100K$ while the loading condition B_y produces a $T_{avg} \approx 600K$, a substantial difference. Loading conditions C_1 and R_m follow similar paths as do C_2 and B_y. As expected, percentages of hot volume V_{hot}/V for each loading condition significantly affect the desired average values for both pressure and temperature; more energy per unit volume is required for loading conditions with smaller hot volumes. Adding more energy per unit volume to each system will increase the pressure but will have less of an impact on temperature.

To find the desired average values, density and energy values were manually selected through trial and error process, by probing the contour plots for each loading condition. These values were adjusted until a $P_{avg} \approx 5GPa$ and $T_{avg} \approx 500K$ and are reported on Table 4.1. The values reported on Table 4.1 include values for density ρ, specific energy E, volume percentages V_{hot}/V, average energy per unit volume ρE, average pressure P_{avg} and average temperature T_{avg} for each loading condition. The input values (ρ,E) presented on the table are uniformly distributed within each hot region and produce the corresponding target values. For each case, the average energy per unit volume was calculated and is presented on Figure 4.16. For the target values, the average energy per unit volume does not change significantly, however they do change as a result of hot volume percentages. In an average sense, the pairs C_1/R_m and C_2/B_y perform similarly much like the trends observed from the contours. Initial shock loading of the continuum material system provides a baseline from which to compare heterogeneous material systems examined in the following sections.

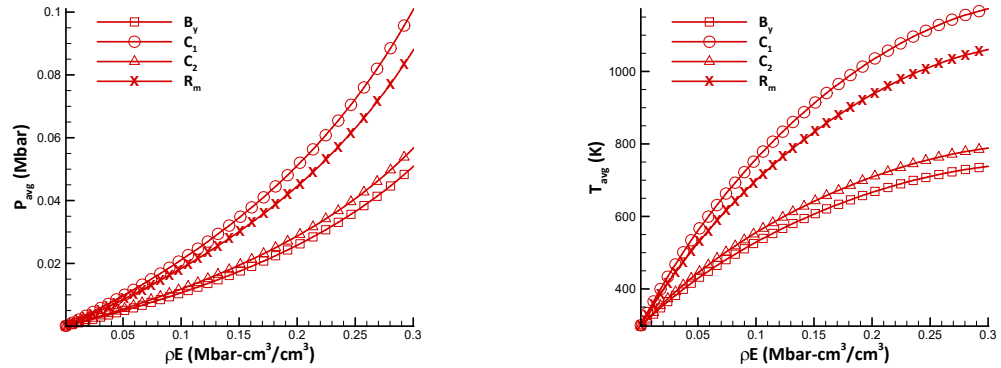

(a) Pressure $(Mbar)$ (b) Temperature (K)

Figure 4.15: A $45°$ slice across pressure(a) and temperature(b) contours for each loading condition on the continuum. More energy per unit volume is required for loading conditions with smaller hot volumes.

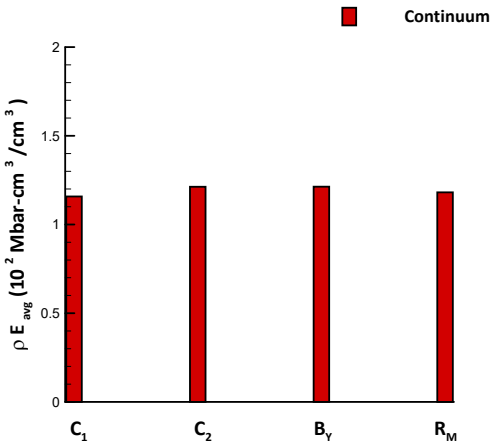

Figure 4.16: Average energy per unit volume of the continuum for each loading condition where $P_{avg} = 5GPa$ and $T_{avg} = 500K$.

4.2.2 Initial Conditions: $\eta = 0.75$

This section considers the initiation of the heterogeneous material system shown in Figure 4.7(a) where the mass fraction of HMX is $\eta = 0.75$. Here the microstructure is explicitly modeled and a binary representation is considered, where each pixel represents either pure HMX or polymeric binder. Unlike the continuum, material properties vary spatially; equations of state for both HMX and binder are necessary. To find the average target values of $P_{avg} = 5GPa$ and $T_{avg} = 500K$ a wide search is performed.

Density is varied from $\rho = 1.844 - 3.0\, g/cm^3$ and specific total energy is varied from $E = 0.0 - 0.1\, Mbar - cm^3/g$, where the lower bounds produce the ambient conditions of $P_0 = 0.0GPa$ and $T_0 = 295K$. Equations 4.6 and 4.7 no longer hold as material properties vary spatially; V_{hot} contains both HMX and binder. However, within each individual material system, pressure values and temperature values do not change and the following equations are used

$$P_{avg} = (P_H(V_{hotH}) + P_B(V_{hotB}))/V + P_0(1 - V_{hot}/V) \tag{4.8}$$

$$T_{avg} = (T_H(V_{hotH}) + T_B(V_{hotB}))/V + T_0(1 - V_{hot}/V) \tag{4.9}$$

where subscript with H and B denote HMX and binder respectively. Here volumes of hot HMX and binder make up the total hot volume; i.e. $V_{hot} = V_{hotH} + V_{hotB}$. The values of local pressure and temperature($P_{H,B}$,$T_{H,B}$) are found from Equations 2.7-2.9, where the materials are pure solids. Results for average pressure and temperature of the heterogeneous material where $\eta = 0.75$ are reported for all loading conditions on Figures 4.17(a)-4.20(c). Each figure shows the loading condition (a), the average pressure (b) and the average temperature (c). Average pressure and temperature are represented by contour plots where the x-axis is density and the y-axis is specific energy; for an input density and energy a corresponding average pressure/temperature over the entire domain is represented by the contour map. Again, optimization techniques may be exploited to find the target values using Equations 4.8-4.9.

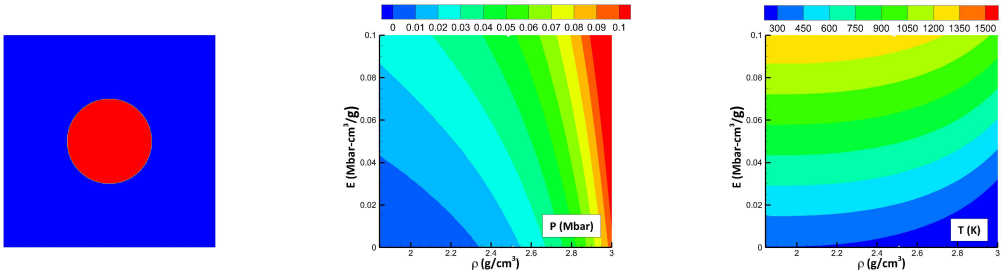

(a) Loading Condition: C_1 (b) Average pressure (c) Average temperature

Figure 4.17: Average pressure P_{avg}(b) and temperature T_{avg}(c) contours for heterogeneous material where $\eta = 0.75$ subjected to C_1 loading condition. The input density(x-axis) and energy(y-axis) produce the corresponding average value(contour) over the entire domain.

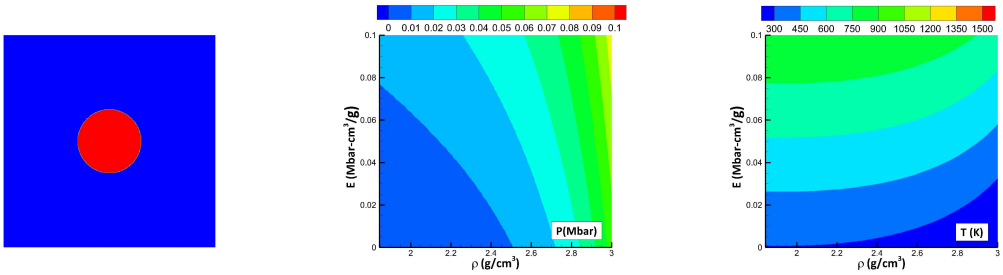

(a) Loading Condition: C_2 (b) Average pressure (c) Average temperature

Figure 4.18: Average pressure P_{avg}(b) and temperature T_{avg}(c) contours for heterogeneous material where $\eta = 0.75$ subjected to C_2 loading condition. The input density(x-axis) and energy(y-axis) produce the corresponding average value(contour) over the entire domain.

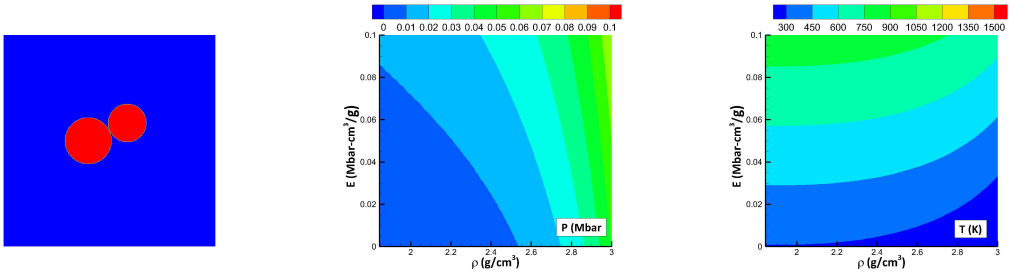

(a) Loading Condition: B_y (b) Average pressure (c) Average temperature

Figure 4.19: Average pressure P_{avg}(b) and temperature T_{avg}(c) contours for heterogeneous material where $\eta = 0.75$ subjected to B_y loading condition. The input density(x-axis) and energy(y-axis) produce the corresponding average value(contour) over the entire domain.

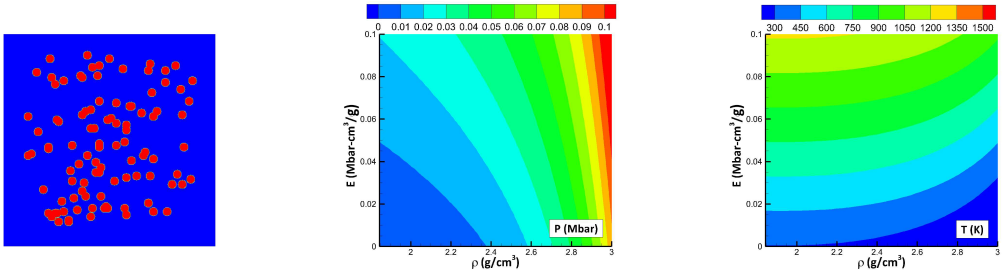

(a) Loading Condition: R_m (b) Average pressure (c) Average temperature

Figure 4.20: Average pressure P_{avg}(b) and temperature T_{avg}(c) contours for heterogeneous material where $\eta = 0.75$ subjected to R_m loading condition. The input density(x-axis) and energy(y-axis) produce the corresponding average value(contour) over the entire domain.

The same study is performed where a 45° cut taken from $[1.844, 0.0]$ to $[3.0, 0.1]$ in density-energy space is taken across each contour. Figure 4.21(a) shows pressure slices of contours from Figures 4.17(b), 4.18(b), 4.19(b), and 4.20(a), where the x-axis represents energy per unit volume (ρE) and the y-axis represents the corresponding average pressure in $Mbar$. For all loading conditions, trends initiate from the ambient condition ($P = P_0$) and pressure increases with energy per unit volume. The rate at which pressure changes, increases with energy. Similar to the previous material system, the first loading condition C_1 requires the least amount of energy per unit volume to produce any pressure while the binary condition B_y requires the most. The pairs C_1/R_m and C_2/B_y perform similarly due to their similar hot volume percentages. For an energy per unit volume value of $\rho E = 0.2Mbar - cm^3/g$ loading conditions C_1/R_m produces $P_{avg} \approx 0.60Mbar$ while the loading condition C_2/B_y produces a $P_{avg} \approx 0.30Mbar$, a substantial difference. These trends will be compared with all material systems in Section 4.2.5

For the temperature profiles shown on Figure 4.21(b), similar observations are made. For all loading conditions, trends initiate from the ambient condition ($T = T_0$) and Temperature increases with energy per unit volume. However, the rate at which temperature changes, decreases with energy; i.e. temperature plateaus, unlike pressure. Again, the loading condition pairs C_1/R_m require the least amount of energy per unit volume while the C_2/B_y pair requires the most. For an energy per unit volume value of $\rho E = 0.2Mbar - cm^3/g$ loading condition C_1 produces $T_{avg} \approx 900K$ while the loading condition B_y produces a $T_{avg} \approx 600K$, a substantial difference. Percentages of hot volume V_{hot}/V for each loading condition significantly affect the desired average values for both pressure and temperature; more energy per unit volume is required for loading conditions with smaller hot volumes. Further increasing energy per unit volume of each system will increase pressure but will have less of an effect on temperature.

To find the desired average values, density and energy values were manually selected through trial and error process, by probing the contour plots for each loading condition. These values were adjusted until a $P_{avg} \approx 5GPa$ and $T_{avg} \approx 500K$ and are reported on Table 4.1. Initial pressure contours for each loading condition are shown on Figures 4.22(a)- 4.22(d). From these plots the microstructure is visible through the contour showing the variability in pressure values between HMX and binder. Figure 4.22(a) shows the C_1 loading condition where local pressures for HMX and binder are $P \approx 0.40Mbar$ and $P \approx 0.25Mbar$ respectively. Figures 4.22(b) and 4.22(c) show the C_2/B_y loading conditions where the local HMX pressure is $P \approx 0.5Mbar$ and the local binder pressure is $P \approx 0.35Mbar$. The R_m loading condition is similar to the C_1 condition, with slightly higher values needed to make up for the difference in volume. Initial temperature contours for each

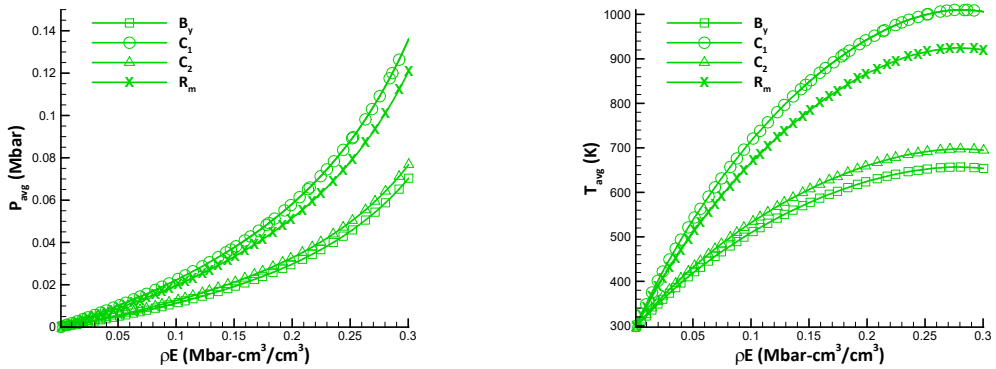

(a) Pressure $(Mbar)$ (b) Temperature (K)

Figure 4.21: A $45°$ slice across pressure(a) and temperature(b) contours for each loading condition on the heterogeneous material where $\eta = 0.75$. More energy per unit volume is required for loading conditions with smaller hot volumes.

loading condition are shown on Figures 4.23(a)- 4.23(d). Unlike the pressure contours, the microstructure is not visible in the current color map ranges, and the temperature is nearly uniform. Figure 4.23(a) shows the C_1 loading condition with temperature values $T \approx 1800K$. Figures 4.23(b) and 4.23(c) show values of $T \approx 3000K$ and above. The R_m loading condition has local temperature values near $T \approx 2100K$. For each case, the average energy per unit volume was calculated and is presented on Figure 4.24. For the target values, the average energy per unit volume does not change significantly, however they do change as a result of hot volume percentages. In an average sense, the pairs C_1/R_m and C_2/B_y perform similarly much like the trends observed from the contours. All material systems are compared in Section 4.2.5.

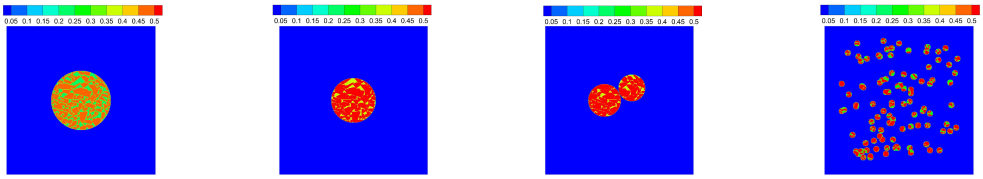

(a) C_1 (b) C_2 (c) B_y (d) R_m

Figure 4.22: Initial pressure (Mbar) contours of $\eta = 0.75$ material for all loading conditions where $P_{avg} = 5GPa$ and $T_{avg} = 500K$. Local pressures within hotspots appear to vary spatially.

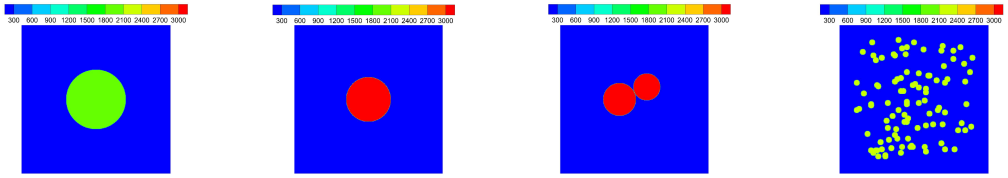

(a) C_1 (b) C_2 (c) B_y (d) R_m

Figure 4.23: Initial temperature (K) contours of $\eta = 0.75$ material for all loading conditions where $P_{avg} = 5GPa$ and $T_{avg} = 500K$. Local temperatures within hotspots appear uniform.

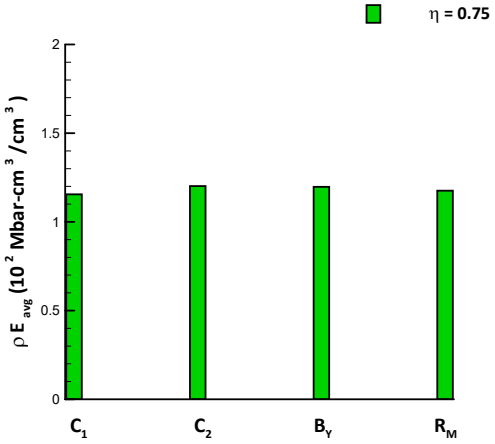

Figure 4.24: Average energy per unit volume of $\eta = 0.75$ heterogeneous material for each loading condition where $P_{avg} = 5GPa$ and $T_{avg} = 500K$.

4.2.3 Initial Conditions: $\eta = 0.85$

This section considers the initiation of the heterogeneous material system shown in Figure 4.7(b) where the mass fraction of HMX is $\eta = 0.85$. Here the microstructure is explicitly modeled and material properties vary spatially. Equations of state for both HMX and binder are necessary. The same wide search is performed where density and energy are varied with lower bounds producing ambient conditions. Again, V_{hot} contains both HMX and binder and, therefore, average pressure and temperature are calculated using equations 4.8 and 4.9. The values of local pressure and temperature($P_{H,B}$,$T_{H,B}$) are found from Equations 2.7-2.9, where the materials are pure solids. Results for average pressure and temperature are reported for all loading conditions on Figures 4.25(a)-4.28(c). Each figure shows the loading condition (a), the average pressure (b) and the average temperature

(c). Average pressure and temperature are represented by contour plots where the x-axis is density and the y-axis is specific energy; for an input density and energy a corresponding average pressure/temperature over the entire domain is represented by the contour map.

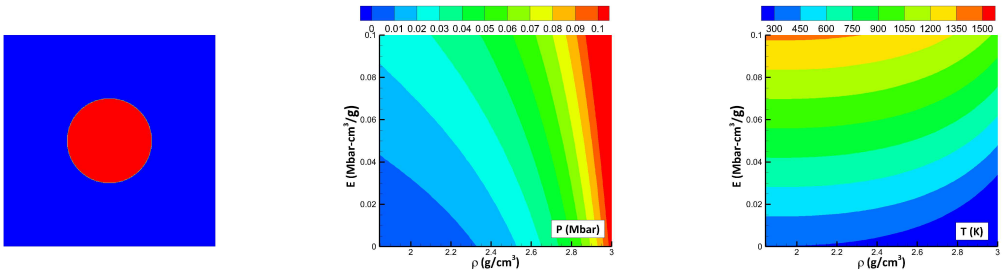

(a) Loading Condition: C_1 (b) Average pressure (c) Average temperature

Figure 4.25: Average pressure P_{avg}(b) and temperature T_{avg}(c) contours for heterogeneous material where $\eta = 0.85$ subjected to C_1 loading condition. The input density(x-axis) and energy(y-axis) produce the corresponding average value(contour) over the entire domain.

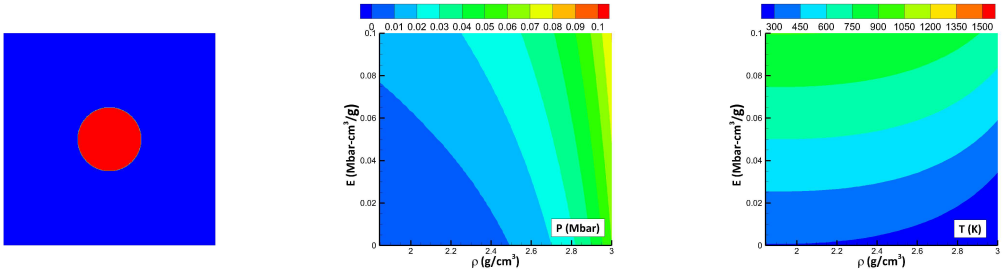

(a) Loading Condition: C_2 (b) Average pressure (c) Average temperature

Figure 4.26: Average pressure P_{avg}(b) and temperature T_{avg}(c) contours for heterogeneous material where $\eta = 0.85$ subjected to C_2 loading condition. The input density(x-axis) and energy(y-axis) produce the corresponding average value(contour) over the entire domain.

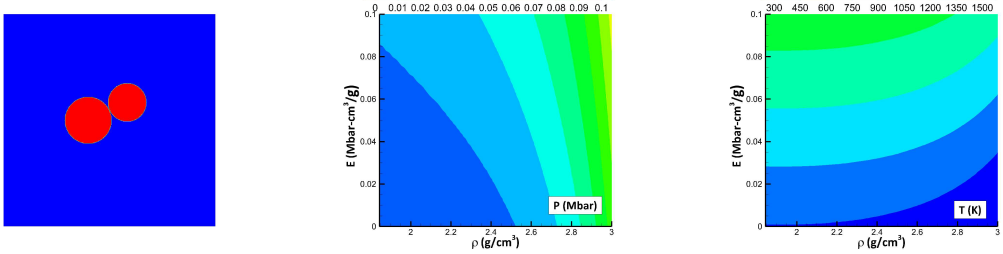

(a) Loading Condition: B_y (b) Average pressure (c) Average temperature

Figure 4.27: Average pressure P_{avg}(b) and temperature T_{avg}(c) contours for heterogeneous material where $\eta = 0.85$ subjected to B_y loading condition. The input density(x-axis) and energy(y-axis) produce the corresponding average value(contour) over the entire domain.

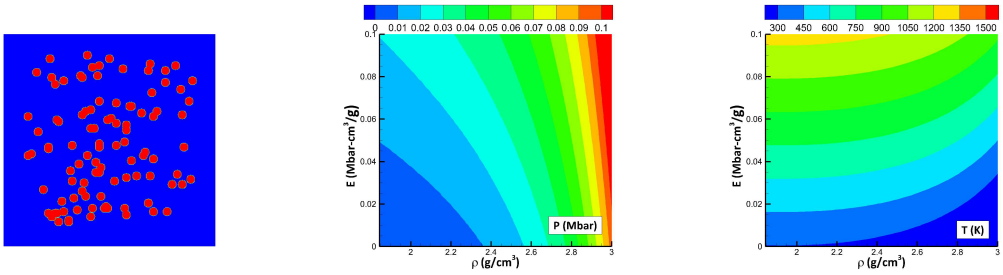

(a) Loading Condition: R_m (b) Average pressure (c) Average temperature

Figure 4.28: Average pressure P_{avg}(b) and temperature T_{avg}(c) contours for heterogeneous material where $\eta = 0.85$ subjected to R_m loading condition. The input density(x-axis) and energy(y-axis) produce the corresponding average value(contour) over the entire domain.

The same study is performed where a $45°$ cut taken from $[1.844, 0.0]$ to $[3.0, 0.1]$ in density-energy space is taken across each contour. Figure 4.29(a) shows pressure slices of contours from Figures 4.25(b), 4.26(b), 4.27(b), and 4.28(a), where the x-axis represents energy per unit volume (ρE) and the y-axis represents the corresponding average pressure in $Mbar$. For all loading conditions, trends initiate from the ambient condition ($P = P_0$) and pressure increases with energy per unit volume. The rate at which pressure changes, increases with energy. Similar to the previous material system, the first loading condition C_1 requires the least amount of energy per unit volume to produce any pressure while the binary condition B_y requires the most. The pairs C_1/R_m and C_2/B_y perform similarly due to their similar hot volume percentages. For an energy per unit volume value of $\rho E = 0.2 Mbar - cm^3/g$ loading conditions C_1/R_m produces $P_{avg} \approx 0.60 Mbar$ while the loading

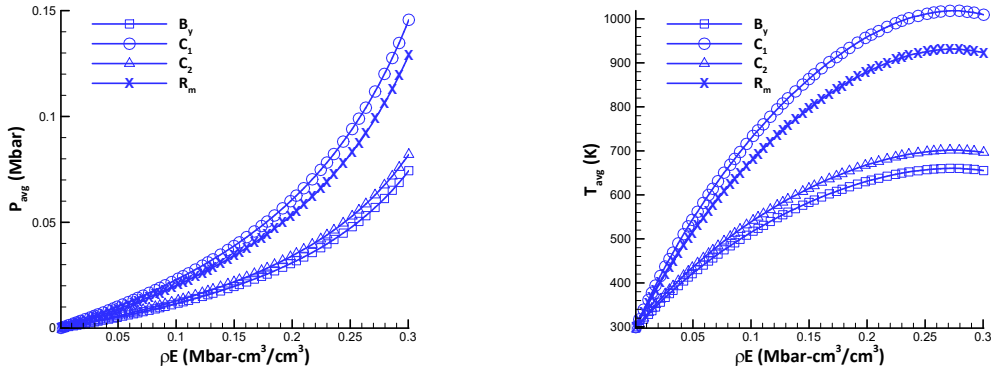

(a) Pressure $(Mbar)$

(b) Temperature (K)

Figure 4.29: A $45°$ slice across pressure(a) and temperature(b) contours for each loading condition on the heterogeneous material where $\eta = 0.85$. More energy per unit volume is required for loading conditions with smaller hot volumes.

condition C_2/B_y produces a $P_{avg} \approx 0.20Mbar$, a substantial difference. These trends will be compared with all material systems in Section 4.2.5

For the temperature profiles shown on Figure 4.29(b), similar observations are made. For all loading conditions, trends initiate from the ambient condition ($T = T_0$) and Temperature increases with energy per unit volume. However, the rate at which temperature changes, decreases with energy; i.e. temperature plateaus, unlike pressure. Again, the loading condition pairs C_1/R_m require the least amount of energy per unit volume while the C_2/B_y pair requires the most. For an energy per unit volume value of $\rho E = 0.2Mbar - cm^3/g$ loading condition C_1 produces $T_{avg} \approx 900K$ while the loading condition B_y produces a $T_{avg} \approx 600K$, a substantial difference. The same conclusions are made; percentages of hot volume V_{hot}/V for each loading condition significantly affect the desired average values for both pressure and temperature. Additional energy per unit volume of each system will increase pressure but these gains are not observed in temperature.

The same trial and error process was used to find the target average values of $P_{avg} \approx 5GPa$ and $T_{avg} \approx 500K$ with initial conditions reported on Table 4.1. Initial pressure contours for each loading condition are shown on Figures 4.30(a)- 4.30(d). From these plots the microstructure is visible through the contour showing the variability in pressure values between HMX and binder. Figure 4.30(a) shows the C_1 loading condition where local pressures for HMX and binder are $P \approx 0.45Mbar$ and $P \approx 0.25Mbar$ respectively. Figures 4.30(b) and 4.30(c) show the C_2/B_y loading conditions where the local HMX pressure is $P \approx 0.5Mbar$ and the local binder pressure is $P \approx 0.35Mbar$. The R_m loading condi-

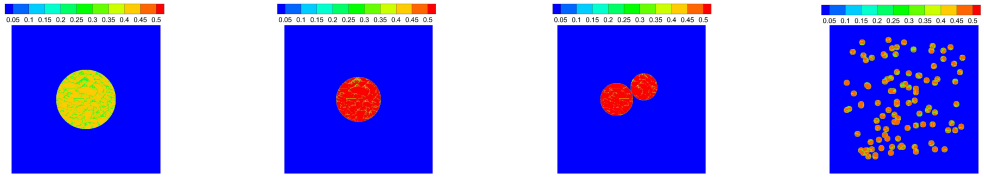

(a) C_1 (b) C_2 (c) B_y (d) R_m

Figure 4.30: Initial pressure (Mbar) contours of $\eta = 0.85$ material for all loading conditions where $P_{avg} = 5GPa$ and $T_{avg} = 500K$. Local pressures within hotspots appear to vary spatially

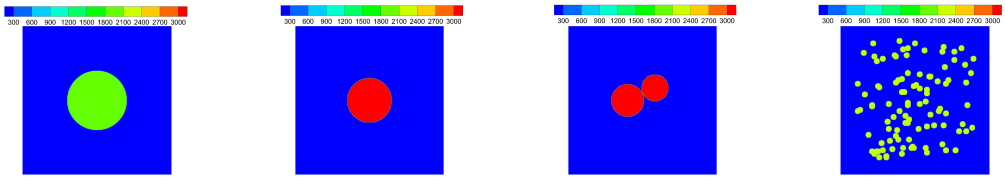

(a) C_1 (b) C_2 (c) B_y (d) R_m

Figure 4.31: Initial temperature (K) contours of $\eta = 0.85$ material for all loading conditions where $P_{avg} = 5GPa$ and $T_{avg} = 500K$. Local temperatures within hotspots appear uniform.

tion is similar to the C_1 condition, with slightly higher values needed to make up for the difference in volume. Initial temperature contours for each loading condition are shown on Figures 4.31(a)- 4.31(d). Unlike the pressure contours, the microstructure is not visible in the current color map ranges, and the temperature is nearly uniform. Figure 4.31(a) shows the C_1 loading condition with temperature values $T \approx 1800K$. Figures 4.31(b) and 4.31(c) show values of $T \approx 3000K$ and above. The R_m loading condition has local temperature values near $T \approx 2100K$. For each case, the average energy per unit volume was calculated and is presented on Figure 4.32. For the target values, the average energy per unit volume does not change significantly, however they do change as a result of hot volume percentages. In an average sense, the pairs C_1/R_m and C_2/B_y perform similarly much like the trends observed from the contours. All material systems are compared in Section 4.2.5.

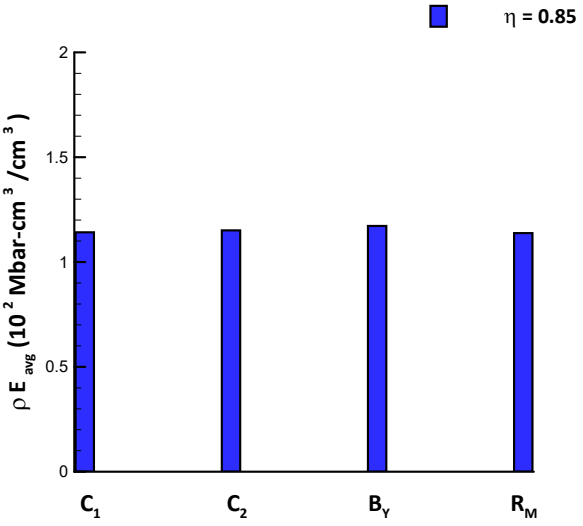

Figure 4.32: Average energy per unit volume of $\eta = 0.85$ heterogeneous material for each loading condition where $P_{avg} = 5GPa$ and $T_{avg} = 500K$.

4.2.4 Initial Conditions: $\eta = 0.95$

This section considers the initiation of the heterogeneous material system shown in Figure 4.7(c) where the mass fraction of HMX is $\eta = 0.95$. Here the microstructure is explicitly modeled and material properties vary spatially. Average pressure and temperature are calculated using equations 4.8 and 4.9. Results for average pressure and temperature are reported for all loading conditions on Figures 4.33(a)-4.36(c). Each figure shows the loading condition (a), the average pressure (b) and the average temperature (c). Average pressure and temperature are represented by contour plots where the x-axis is density and the y-axis is specific energy; for an input density and energy a corresponding average pressure/temperature over the entire domain is represented by the contour map.

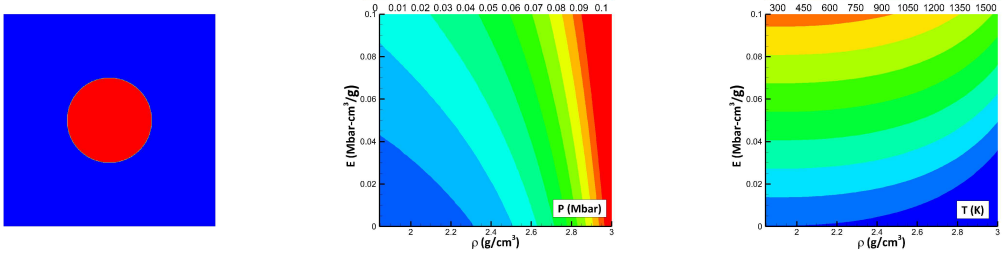

(a) Loading Condition: C_1 (b) Average pressure (c) Average temperature

Figure 4.33: Average pressure P_{avg}(b) and temperature T_{avg}(c) contours for heterogeneous material where $\eta = 0.95$ subjected to C_1 loading condition. The input density(x-axis) and energy(y-axis) produce the corresponding average value(contour) over the entire domain..

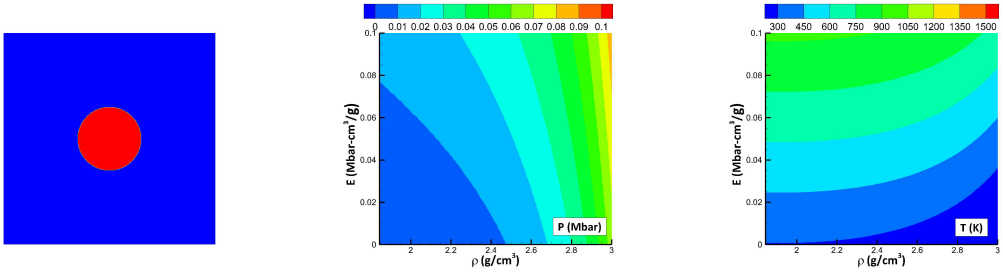

(a) Loading Condition: C_2 (b) Average pressure (c) Average temperature

Figure 4.34: Average pressure P_{avg}(b) and temperature T_{avg}(c) contours for heterogeneous material where $\eta = 0.95$ subjected to C_2 loading condition. The input density(x-axis) and energy(y-axis) produce the corresponding average value(contour) over the entire domain.

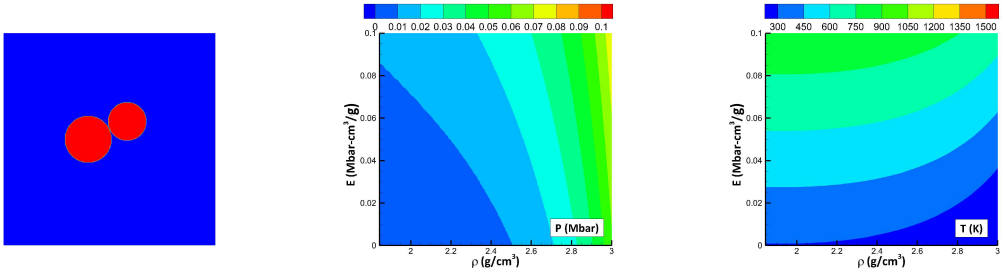

(a) Loading Condition: B_y (b) Average pressure (c) Temp

Figure 4.35: Average pressure P_{avg}(b) and temperature T_{avg}(c) contours for heterogeneous material where $\eta = 0.95$ subjected to B_y loading condition. The input density(x-axis) and energy(y-axis) produce the corresponding average value(contour) over the entire domain.

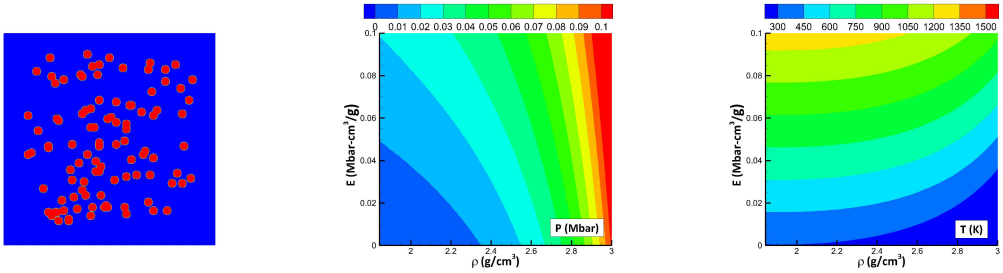

(a) Loading Condition: R_m (b) Average pressure (c) Temp

Figure 4.36: Average pressure P_{avg}(b) and temperature T_{avg}(c) contours for heterogeneous material where $\eta = 0.95$ subjected to R_m loading condition. The input density(x-axis) and energy(y-axis) produce the corresponding average value(contour) over the entire domain.

Slices are taken across each contour, where Figures 4.37(a) and 4.37(b) show pressure and temperature respectively. Here, the x-axis represents energy per unit volume (ρE) and the y-axis represents the corresponding average pressure or temperature values. Similar to all previous material systems, the first loading condition C_1 requires the least amount of energy per unit volume while the binary condition B_y requires the most. The pairs C_1/R_m and C_2/B_y perform similarly due to their similar hot volume percentages. Additional energy per unit volume of each system will increase pressure but these gains are not observed in temperature. Initial conditions needed to achieve average values of $P_{avg} \approx 5GPa$ and $T_{avg} \approx 500K$ are reported on Table 4.1. Initial pressure contours for each loading condition are shown on Figures 4.38(a)- 4.38(d). From these plots the microstructure is visible through the contour showing the variability in pressure values between HMX and binder. Figure 4.38(a) shows the C_1 loading condition where local pressures for HMX and binder are $P \approx 0.40Mbar$ and $P \approx 0.25Mbar$ respectively. Figures 4.38(b) and 4.38(c) show the C_2/B_y loading conditions where the local HMX pressure is $P \approx 0.5Mbar$ and the local binder pressure is $P \approx 0.35Mbar$. The R_m loading condition is similar to the C_1 condition, with slightly higher values needed to make up for the difference in volume. Initial temperature contours for each loading condition are shown on Figures 4.39(a)- 4.39(d), where temperature is nearly uniform. Figure 4.39(a) shows the C_1 loading condition with temperature values $T \approx 1800K$. Figures 4.39(b) and 4.39(c) show values of $T \approx 3000K$ and above. The R_m loading condition has local temperature values near $T \approx 2100K$. For each case, the average energy per unit volume was calculated and is presented on Figure 4.40. For the target values, the average energy per unit volume does not change significantly, however they do change as a result of hot volume percentages. In an average sense, the pairs C_1/R_m and C_2/B_y perform similarly much like the trends observed from the con-

tours. Next, all material systems are compared in Section 4.2.5.

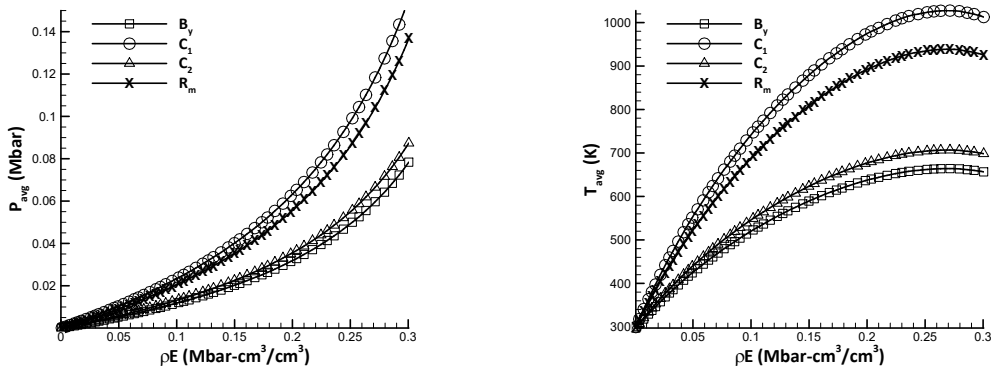

(a) Pressure $(Mbar)$ (b) Temperature (K)

Figure 4.37: A 45° slice across pressure(a) and temperature(b) contours for each loading condition on the heterogeneous material where $\eta = 0.95$. More energy per unit volume is required for loading conditions with smaller hot volumes.

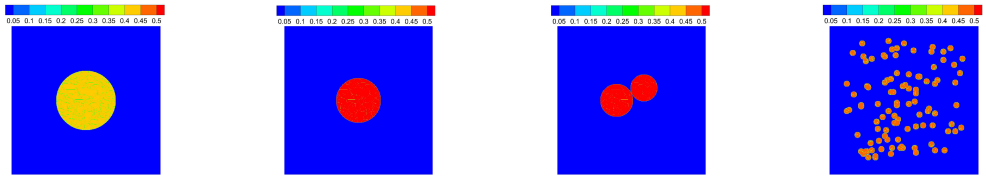

(a) Pressure $(Mbar)$ (b) Pressure $(Mbar)$ (c) Pressure $(Mbar)$ (d) Pressure $(Mbar)$

Figure 4.38: Initial pressure (Mbar) contours of $\eta = 0.95$ material for all loading conditions where $P_{avg} = 5GPa$ and $T_{avg} = 500K$. Local pressures within hotspots appear to vary spatially.

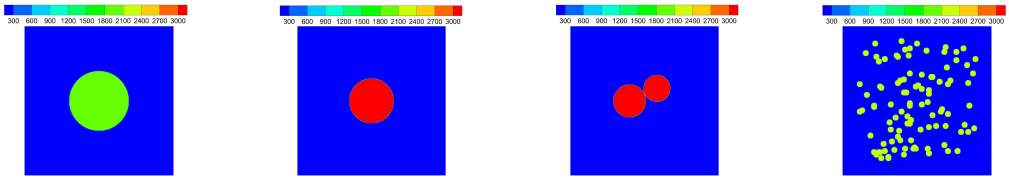

(a) Temperature (K) (b) Temperature (K) (c) Temperature (K) (d) Temperature (K)

Figure 4.39: Initial temperature (K) contours of $\eta = 0.95$ material for all loading conditions where $P_{avg} = 5GPa$ and $T_{avg} = 500K$. Local temperatures within hotspots appear uniform.

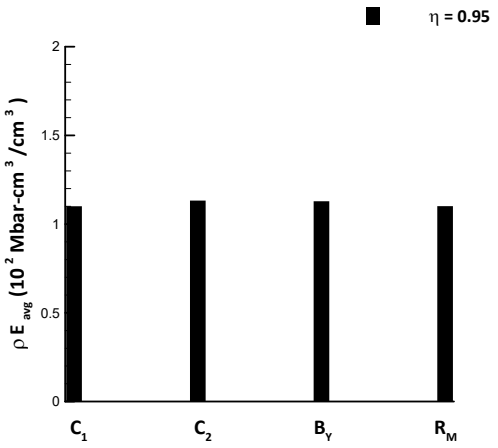

Figure 4.40: Average energy per unit volume of $\eta = 0.95$ heterogeneous material for each loading condition where $P_{avg} = 5GPa$ and $T_{avg} = 500K$.

4.2.5 Initial Conditions: All Material Systems

In this section, initiation of material system from the previous sections are compared. The continuum and heterogeneous systems, with mass fractions of $\eta = 0.75, 0.85, 0.95$, are considered for all loading conditions. Average values in density -energy space are compared by taking a $45°$ cut taken from $[1.844, 0.0]$ to $[3.0, 0.1]$ across each pressure and temperature contour. First, the C_1 loading condition is investigated on Figures 4.41(a) and 4.41(b), where each color corresponds to a different material system. Figures 4.41(a) shows average pressure as a function of energy per unit volume. All material systems on this plot follow the same trend; increasing energy per unit volume increases average pressure, and the rate at which average pressure changes. All curves originate from the ambient condition ($P = 0.0\,Mbar$) and align at low energies per unit volume. However, as energy per unit volume increases, the curves begin to deviate from one another with the greatest deviation from the continuum material system. The heterogeneous material systems deviate but are tightly bound. From these trends, the effects of including microstructural information are apparent; explicitly modeling the microstructure plays a significant role in initial shock loading of PBXs. Heterogeneous material systems produce higher average pressure values when compared to the continuum material system. By including microstructural information, the material system is more sensitive in an average sense. As an example, for $\rho E = 0.25\,Mbar - cm^3/cm^3$, the continuum media produces $P_{avg} \approx 0.07\,Mbar$, while the heterogeneous media is near $P_{avg} \approx 0.09\,Mbar$. Thus, the continuum material systems require more energy per unit volume to achieve the same average pressure values of

heterogeneous material systems.

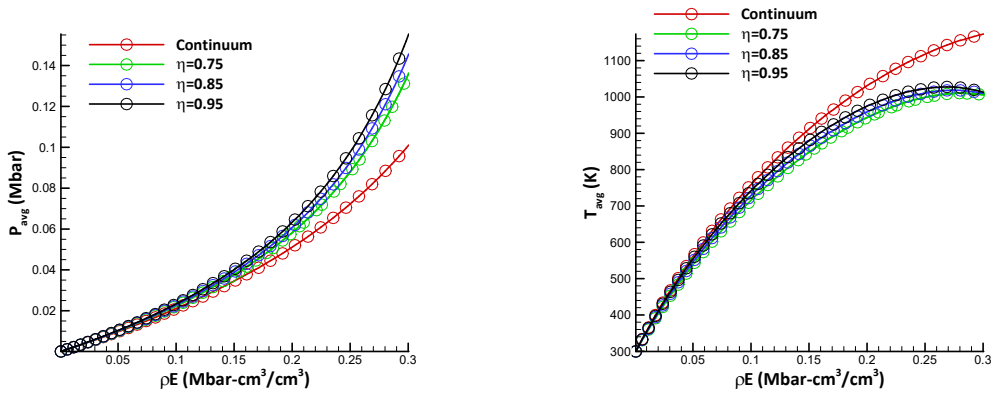

(a) Pressure $(Mbar)$ (b) Temperature (K)

Figure 4.41: A 45° slice across pressure(a) and temperature(b) contours for C_1 loading condition for all material systems. The effects of the microstructure grow with increasing energy per unit volume.

In comparing the heterogeneous material systems, material systems deviate at larger energies per unit volume. The differences in response can be attributed to binder content; materials with larger percentages of binder content require more energy to produce the same output as those with less binder content. In this sense, increasing binder content decreases the sensitivity of the average pressure material response. As an example, for $\rho E = 0.25\, Mbar - cm^3/cm^3$, the $\eta = 0.75$ material system produces $P_{avg} = 0.087\, Mbar$. Increasing the percentage of HMX by 10% increases the average response $P_{avg} = 0.092\, Mbar$. For the maximum HMX content, where $\eta = 0.95$, $P_{avg} = 0.097\, Mbar$, a 12% increase from the $\eta = 0.75$ material system. The relationship between average response and binder content is linear for a give energy per unit volume.

Figures 4.41(b) shows average temperature as a function of energy per unit volume. All material systems on this plot follow the same trend; increasing energy per unit volume increases average temperature, However, the rate at which average temperature changes decreases, unlike pressure. All curves originate from the ambient condition ($T = 295\, K$) and align at low energies per unit volume. However, as energy per unit volume increases, the curves begin to deviate from one another with the greatest deviation from the continuum material system.

The heterogeneous material systems deviate but are tightly bound and converge to the final value $T_{avg} \approx 655\, K$. From these trends, the effects of including microstructural information are apparent; explicitly modeling the microstructure plays a significant role in

initial shock loading of PBXs. However, the opposite effect is observed when compare to average pressure. Heterogeneous material systems produce lower average temperature values when compared to the continuum material system. By including microstructural information, the material system is less sensitive in an average sense. As an example, for $\rho E = 0.25\, Mbar - cm^3/cm^3$, the continuum media produces $T_{avg} \approx 709\, K$, while the heterogeneous media is near $T_{avg} \approx 655 K$. Thus, continuum material systems require less energy per unit volume to achieve the same average temperature values of heterogeneous material systems. Furthermore, due to the declining rate of increase, the heterogeneous material systems plateau and may never be able to achieve the same average temperature ranges as the continuum.

In comparing the heterogeneous material systems, material systems deviate at larger energies per unit volume. The differences in response can be attributed to binder content; materials with larger percentages of binder content require more energy to produce the same output as those with less binder content. In this sense, increasing binder content decreases the sensitivity of the average temperature material response. As an example, for $\rho E = 0.25\, Mbar - cm^3/cm^3$, the $\eta = 0.75$ material system produces $T_{avg} = 651\, K$. Increasing the percentage of HMX by 10% increases the average response $T_{avg} = 656\, K$. For the maximum HMX content, where $\eta = 0.95$, $T_{avg} = 661\, K$, a 1% increase from the $\eta = 0.75$ material system. The relationship between average response and binder content is linear for a give energy per unit volume. Plots 4.42(a)-4.44(b) show results for the other loading conditions (C_2,B_y,R_m) and follow the same trends and observations of the first case. They will not be discussed in further detail

In general, from these plots, the continuum performs much like the heterogeneous material systems at lower energies per unit volume. As more energy is put into each system, the curves begin to deviate. The continuum is less sensitive in average pressure space but more sensitive in average temperature space. Note, that the continuum material system includes binder effects through manipulation of material constants. These effects, however, are significantly different when explicitly modeling the microstructure where material heterogeneity heavily influences the loading conditions. Among heterogeneous material systems binder content reduces sensitivity. The continuum material most closely follows the $\eta = 0.75$ system for average pressure and the higher HMX content $\eta = 0.95$ system for temperature. Note, that the desired average values of $P_{avg} = 5GPa$ and $T_{avg} = 500K$ are not achieved on this plane for all material systems and loading conditions. To reach the desired temperature a much higher energy per unit volume is needed than for the desired average pressure.

The desired averages for all loading conditions and all materials are reported on Table

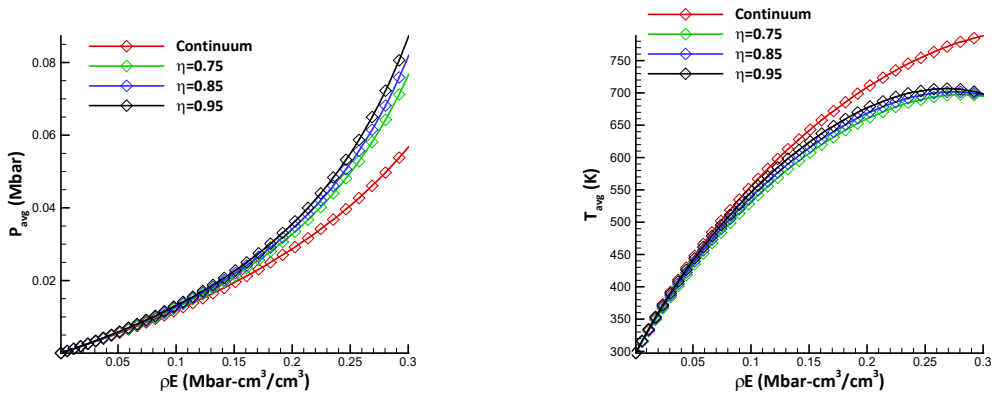

(a) Pressure $(Mbar)$ (b) Temperature (K)

Figure 4.42: A 45° slice across pressure(a) and temperature(b) contours for C_2 loading condition for all material systems. The effects of the microstructure grow with increasing energy per unit volume.

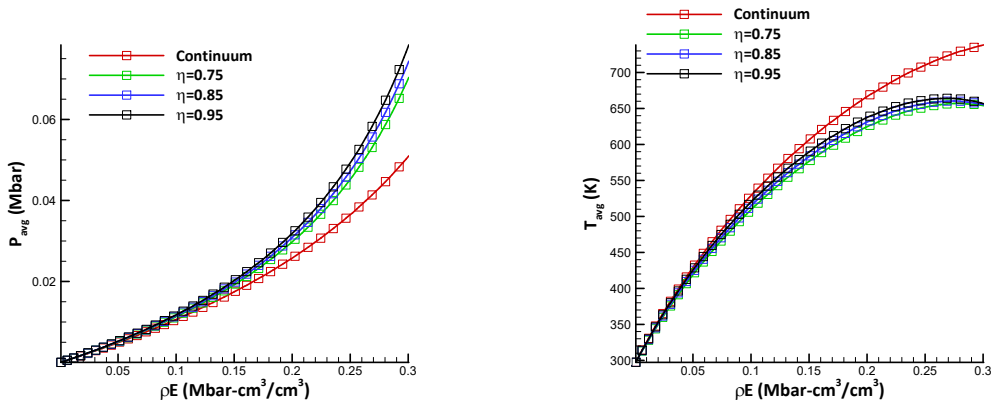

(a) Pressure $(Mbar)$ (b) Temperature (K)

Figure 4.43: A 45° slice across pressure(a) and temperature(b) contours for B_y loading condition for all material systems. The effects of the microstructure grow with increasing energy per unit volume.

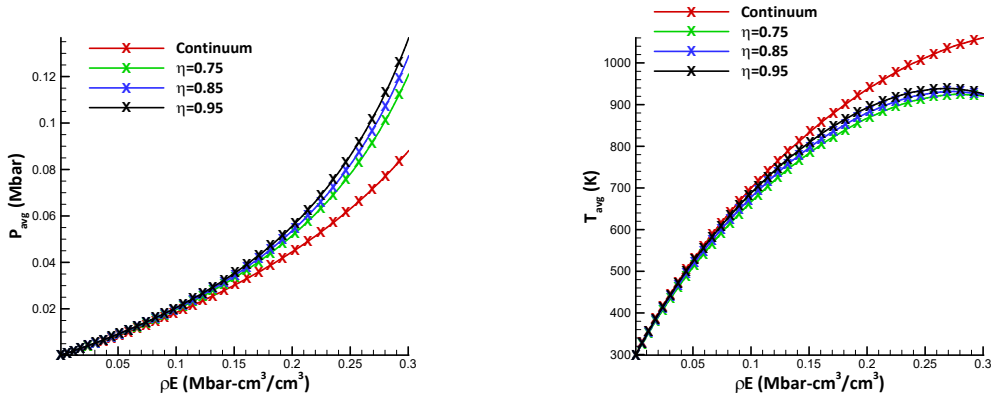

(a) Pressure $(Mbar)$ (b) Temperature (K)

Figure 4.44: A 45° slice across pressure(a) and temperature(b) contours for R_m loading condition for all material systems. The effects of the microstructure grow with increasing energy per unit volume.

4.1. The average energy per unit volume is reported on Figure 4.45. The continuum performs most like the $\eta = 0.75$ material in an average sense. As expected, percentages of hot volume V_{hot}/V for each loading condition significantly affect the desired average values for both pressure and temperature; more energy per unit volume is required for loading conditions with smaller hot volumes. Next, numerical simulation is performed for all material systems and all loading conditions.

Loading Condition	ρ (g/cm^3)	E $(Mbar-cm^3/g)$	$10^2 \frac{V_{hot}}{V_{total}}$	ρE_{avg} $(Mbar)$	P_{avg} (GPa)	T_{avg} (K)
Continuum						
C_1	2.838	0.0325	12.56	0.0115	5.00	500.41
C_2	3.025	0.0568	7.06	0.0121	5.00	503.04
B_y	3.061	0.0627	6.34	0.0121	5.01	501.08
R_m	2.884	0.0372	10.95	0.0118	5.04	501.78
$\boldsymbol{\eta = 0.75}$						
C_1	2.747	0.0335	12.56	0.0116	5.04	499.55
C_2	2.910	0.0585	7.06	0.0120	5.07	500.31
B_y	2.931	0.0646	6.34	0.0119	5.06	502.13
R_m	2.781	0.0384	10.95	0.0117	5.03	504.22
$\boldsymbol{\eta = 0.85}$						
C_1	2.731	0.0333	12.56	0.0114	5.08	504.71
C_2	2.881	0.0566	7.06	0.0115	4.97	500.83
B_y	2.915	0.0636	6.34	0.0117	5.06	503.52
R_m	2.764	0.0374	10.95	0.0113	5.05	502.06
$\boldsymbol{\eta = 0.95}$						
C_1	2.713	0.0323	12.56	0.0110	5.09	501.79
C_2	2.870	0.0559	7.06	0.0113	5.05	501.17
B_y	2.897	0.0616	6.34	0.0112	5.02	499.66
R_m	2.747	0.0364	10.95	0.0110	5.04	500.30

Table 4.1: Summary of initial conditions for all material systems and all loading conditions needed to achieve a $P_{avg} = 5GPa$ and a $T_{avg} = 500K$.

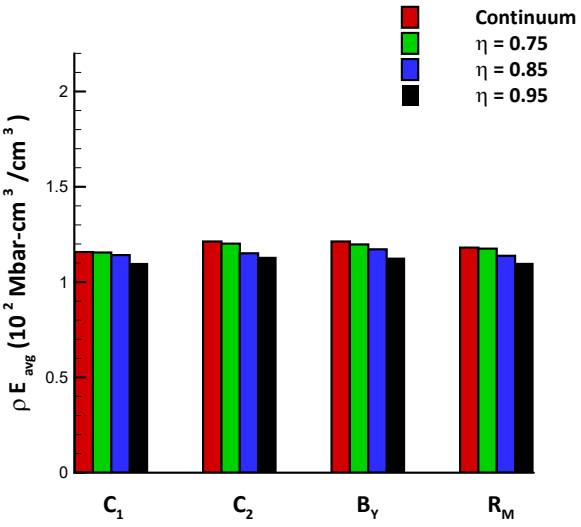

Figure 4.45: Average energy per unit volume of all material systems for each loading condition where $P_{avg} = 5GPa$ and $T_{avg} = 500K$.

4.3 Numerical Results

In this section Direct Numerical Simulation (DNS) results are presented for shock loading on heterogeneous material systems. For DNS, the Euler Equations 2.18 are numerically solved using the Taylor-Galerkin Scheme described in Chapter 2.2. The microstructure is explicitly modeled and four species exist: solid HMX, fully reacted gaseous HMX, solid polymeric binder and gaseous polymeric binder. Therefore, additional transport equations for each species are required and the 2D DNS equations in vector form are written as

$$\mathbf{U} = \begin{bmatrix} \rho \\ \rho u \\ \rho v \\ \rho E \\ \rho Y_{hs} \\ \rho Y_{hg} \\ \rho Y_{bs} \\ \rho Y_{bg} \end{bmatrix}, \qquad \boldsymbol{F_1} = \begin{bmatrix} \rho u \\ \rho u^2 + p \\ \rho uv \\ (\rho E + p)u \\ \rho u Y_{hs} \\ \rho u Y_{hg} \\ \rho u Y_{bs} \\ \rho u Y_{bg} \end{bmatrix}, \qquad \boldsymbol{F_2} = \begin{bmatrix} \rho v \\ \rho vu \\ \rho v^2 + p \\ (\rho E + p)v \\ \rho v Y_{hs} \\ \rho v Y_{hg} \\ \rho v Y_{bs} \\ \rho v Y_{bg} \end{bmatrix},$$

$$and \quad \mathbf{S} = \begin{bmatrix} 0 \\ 0 \\ 0 \\ \rho(q_{hs}\dot{Y_{hs}} + q_{hg}\dot{Y_{hg}} + q_{bs}\dot{Y_{bs}} + q_{bg}\dot{Y_{bg}}) \\ \rho\dot{Y_{hs}} \\ \rho\dot{Y_{hg}} \\ \rho\dot{Y_{bs}} \\ \rho\dot{Y_{bg}} \end{bmatrix} \tag{4.10}$$

where the first subscript denotes the material (HMX/Binder) and the second denotes the state (solid/gas). Reaction rates for each species are first order Arrhenius models with parameters taken from Table 3.3. Here, the rates $\dot{Y}_{hs} = -\dot{Y}_{hg}$ and $\dot{Y}_{bs} = -\dot{Y}_{bg}$ where energy release $q_{hs} = q_{hg}$ and $q_{bs} = q_{bg}$. Given the Eulerian description of the solution procedure, all four species may be present at one point in space and time. A uniform mesh, using 3-noded constant strain triangle elements, is considered with a mesh density of $2,000 ELM/cm$. With 8 local degrees of freedom, and $251,001$ nodes the global number of degrees of freedom is $\approx 2million$. A constant time step of $\Delta t = 1 \times 10^{-5} \mu s$ for a duration of $t = 0.16 \mu s$. Computationally, the solution procedure for all results used 8 computational nodes with 16 cores each for a total number of 128 processes. Computational cost information for each study will be investigated in the following Chapter. Additional contour plots for the following material systems are shown in Appendix E.

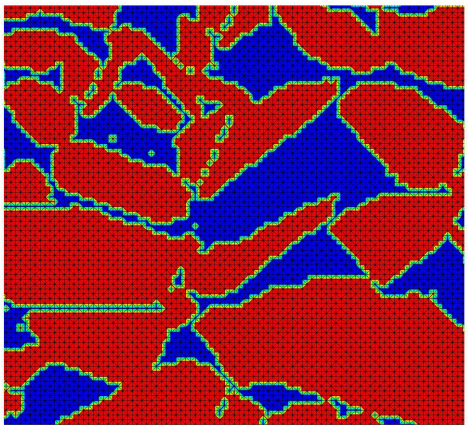

Figure 4.46: Uniform mesh, using 3-noded constant strain triangle elements. Material interfaces captured where red represents HMX and blue represents binder.

4.3.1 Numerical Results: $\eta = 0.75$

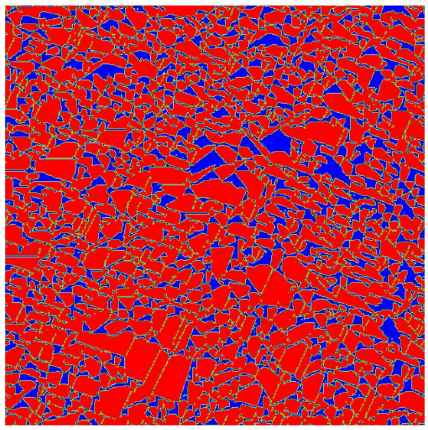

Figure 4.47: Computational representation of heterogeneous $\eta = 0.75$ material system where red represents HMX and blue represents binder.

In this section, DNS results are presented for shock loading on the heterogeneous material system with a HMX mass fraction of $\eta = 0.75$. Contour plots of pressure, temperature, HMX mass fraction and binder fraction are shown on Figures 4.48(a)-4.63(d). These figures show the material response within $t = 0.01\mu s$ for all loading conditions. Contour plots for the remaining duration of the simulation are found in Appendix E.1.

Figures 4.48(a) through 4.51(d) show shock loading for loading condition C_1. Figure 4.48(a) through 4.49(d) show contours for temperature and pressure respectively. From these figures, it is apparent that the materials heterogeneity contributes to the material response. Hot spots form in each contour with peak pressures near $50GPa$ and peak temperatures above $3000K$. Figures 4.50(a) through 4.51(d) show species mass fractions. Initially both HMX and binder are present in solid form within the shocked region. However, as the solution progresses both HMX and binder burn up becoming pure gaseous products. These plots show that binder burns faster than HMX.

Figures 4.52(a) through 4.55(d) show material response to the C_2 loading condition. Similar to C_1 the pressure Contour shown on Figure 4.52(a) shows the material heterogeneity. Peak pressures reach $50GPa$, however, for temperature the response for the initial displayed time step is near $3000K$ and is uniformly distributed. Figure 4.54(a) through 4.55(d) show species mass fractions of the material. Unlike the previous loading condition

HMX and binder are fully burnt up at the initial displayed time step. For the B_y loading condition contour plots are shown on 4.56(a) through 4.59(d). Contour plots of pressure reach values near $50GPa$ and display non-uniform pressure distributions. Similar to the previous condition the binary loading contour for temperature has a uniform distribution and the mass fraction content is fully reacted within the shock region for both HMX and binder.

Finally, the R_m loading condition is considered on 4.60(a) through 4.63(d). Both contour plots for pressure and temperature shown on Figures 4.60(a) through 4.61(d) respectively. Each show material heterogeneity as both display non-uniform pressure and temperature distributions with peak values again near $50GPa$ and $3000K$ within the shocked region. Similar to the first loading case, HMX is present during the first displayed time step and is fully burnt up as a solution progresses. Solid binder, on the other hand is not present in the initial displayed time step and is fully burnt up. These results are studied in an average sense in the following plots.

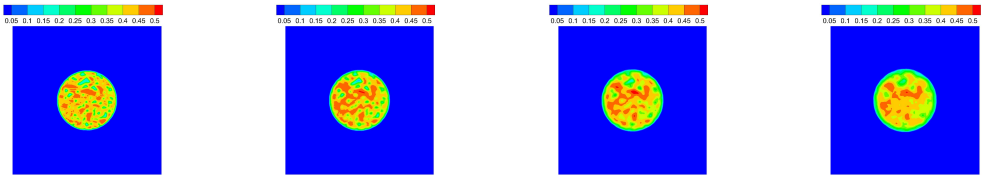

(a) t= 0.0025 (b) t= 0.0050 (c) t= 0.0075 (d) t= 0.0100

Figure 4.48: Pressure contours at initial shock loading of $\eta = 0.75$ heterogeneous material system at various time steps under C_1 loading condition

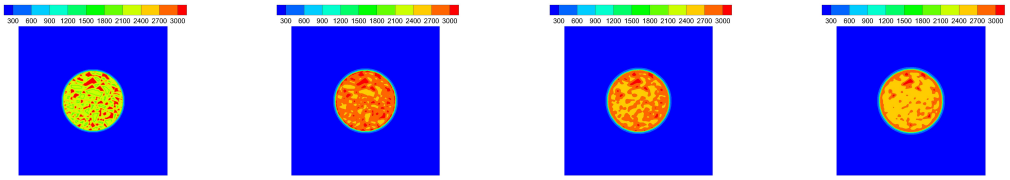

(a) t= 0.0025 (b) t= 0.0050 (c) t= 0.0075 (d) t= 0.0100

Figure 4.49: Temperature contours at initial shock loading of $\eta = 0.75$ heterogeneous material system at various time steps under C_1 loading condition

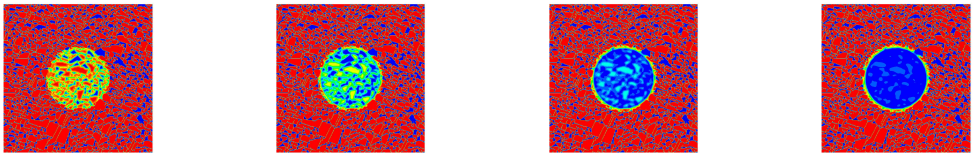

(a) t= 0.0025 (b) t= 0.0050 (c) t= 0.0075 (d) t= 0.0100

Figure 4.50: Solid HMX mass fraction contours at initial shock loading of $\eta = 0.75$ heterogeneous material system at various time steps under C_1 loading condition

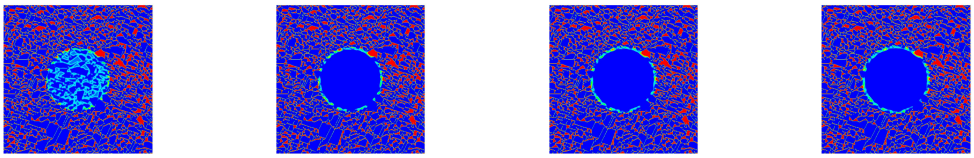

(a) t= 0.0025 (b) t= 0.0050 (c) t= 0.0075 (d) t= 0.0100

Figure 4.51: Solid binder contours at initial shock loading of $\eta = 0.75$ heterogeneous material system at various time steps under C_1 loading condition.

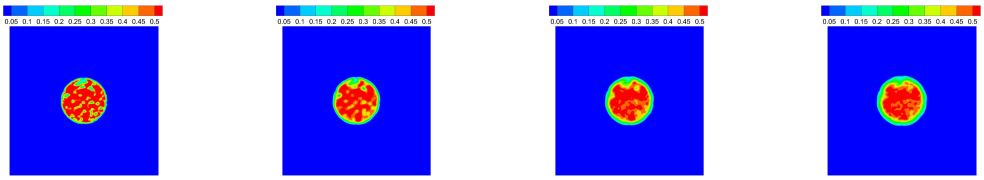

(a) t= 0.0025 (b) t= 0.0050 (c) t= 0.0075 (d) t= 0.0100

Figure 4.52: Pressure contours at initial shock loading of $\eta = 0.75$ heterogeneous material system at various time steps under C_2 loading condition

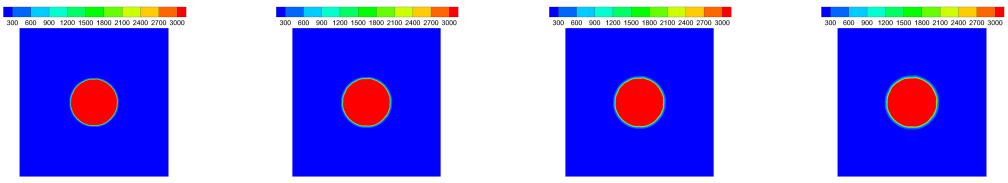

(a) t= 0.0025 (b) t= 0.0050 (c) t= 0.0075 (d) t= 0.0100

Figure 4.53: Temperature contours at initial shock loading of $\eta = 0.75$ heterogeneous material system at various time steps under C_2 loading condition

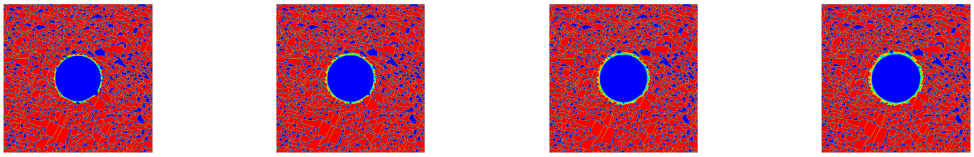

(a) t= 0.0025 (b) t= 0.0050 (c) t= 0.0075 (d) t= 0.0100

Figure 4.54: Solid HMX mass fraction contours at initial shock loading of $\eta = 0.75$ heterogeneous material system at various time steps under C_2 loading condition

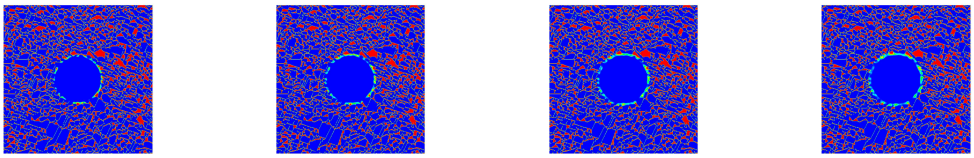

(a) t= 0.0025 (b) t= 0.0050 (c) t= 0.0075 (d) t= 0.0100

Figure 4.55: Solid binder contours at initial shock loading of $\eta = 0.75$ heterogeneous material system at various time steps under C_2 loading condition.

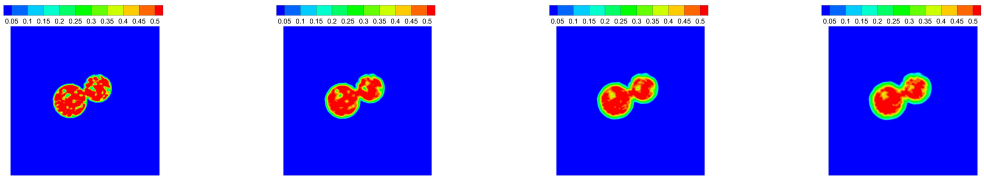

(a) t= 0.0025 (b) t=0.0050 (c) t= 0.0075 (d) t= 0.0100

Figure 4.56: Pressure contours at initial shock loading of $\eta = 0.75$ heterogeneous material system at various time steps under B_Y loading condition

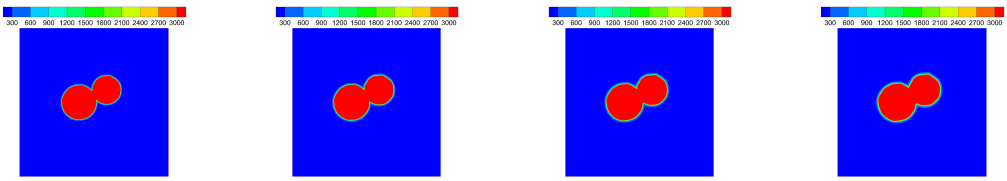

(a) t= 0.0025 (b) t= 0.0050 (c) t= 0.0075 (d) t= 0.0100

Figure 4.57: Temperature contours at initial shock loading of $\eta = 0.75$ heterogeneous material system at various time steps under B_Y loading condition

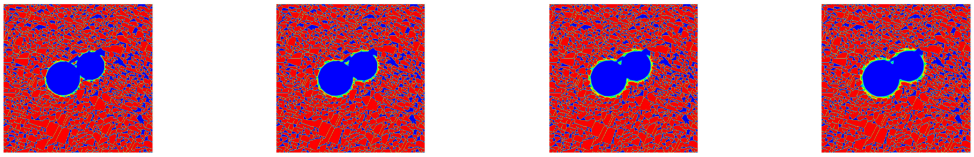

(a) t= 0.0025 (b) t= 0.0050 (c) t= 0.0075 (d) t= 0.0100

Figure 4.58: Solid HMX mass fraction contours at initial shock loading of $\eta = 0.75$ heterogeneous material system at various time steps under B_Y loading condition

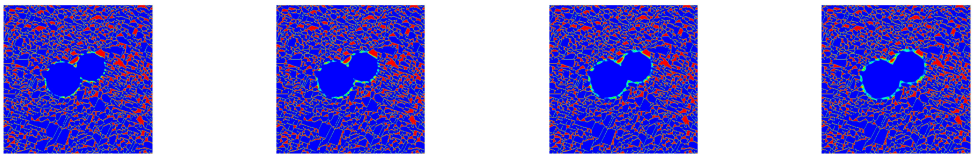

(a) t= 0.0025 (b) t= 0.0050 (c) t= 0.0075 (d) t= 0.0100

Figure 4.59: Solid binder contours at initial shock loading of $\eta = 0.75$ heterogeneous material system at various time steps under B_Y loading condition.

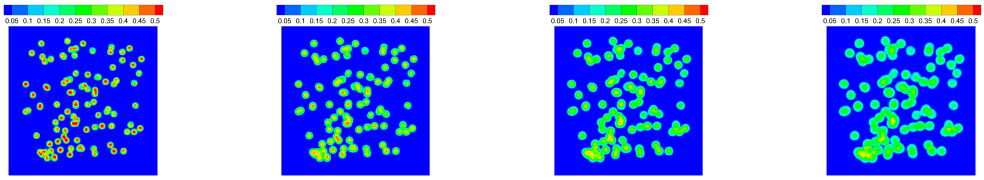

(a) t= 0.0025 (b) t=0.0050 (c) t= 0.0075 (d) t= 0.0100

Figure 4.60: Pressure contours at initial shock loading of $\eta = 0.75$ heterogeneous material system at various time steps under R_M loading condition

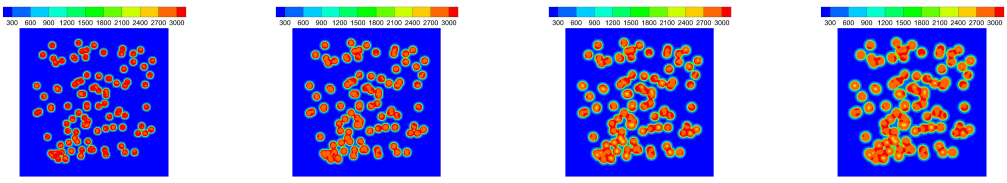

(a) t= 0.0025 (b) t= 0.0050 (c) t= 0.0075 (d) t= 0.0100

Figure 4.61: Temperature contours at initial shock loading of $\eta = 0.75$ heterogeneous material system at various time steps under R_M loading condition

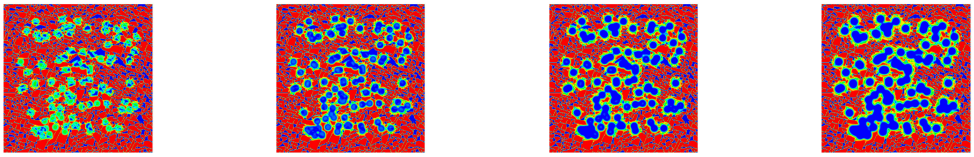

(a) t= 0.0025 (b) t= 0.0050 (c) t= 0.0075 (d) t= 0.0100

Figure 4.62: Solid HMX mass fraction contours at initial shock loading of $\eta = 0.75$ heterogeneous material system at various time steps under R_M loading condition

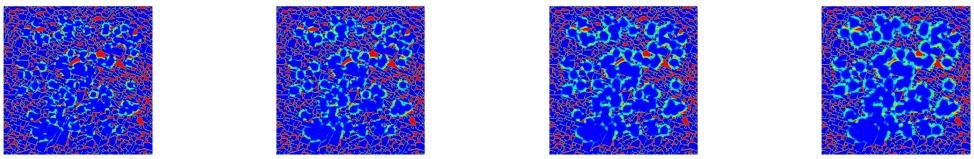

(a) t= 0.0025 (b) t= 0.0050 (c) t= 0.0075 (d) t= 0.0100

Figure 4.63: Solid binder contours at initial shock loading of $\eta = 0.75$ heterogeneous material system at various time steps under R_M loading condition.

Figures 4.64(a) and 4.64(b) show the average pressure and average temperature as a function of time for each loading condition. Average responses were taken by integrating over the previous plots and those shown in Appendix E.1. Figure 4.64(a) shows the pressure response of the $\eta = 0.75$ material system to all loading conditions. The first observation is that three of the loading conditions follow a similar trend, while the R_m loading condition deviates from the other trends. Although the material system initiated with the same average pressure and average temperature, the response is different for varying loading conditions. All curves initiate from the shock pressure of $P_{avg} = 5.0GPa$. As time increases all trends show pressure increasing. The loading conditions C_2 and B_y initially decrease in pressure, going below $P_{avg} = 5.0GPa$. As time increases pressure recovers and reaches a final value near $P_{avg} = 8.0GPa$. These trends align due to their similar hot volume percentages (V_{hot}/V) described in the previous section. This shows that percentage of hot volume can be an indicator for how the material may perform. The C_1 loading condition does not decrease in pressure initially, however, the overall trend is similar to that of the C_2 in B_y loading conditions. Since there is no initial offset pressure, the C_1 loading condition is able to achieve a higher maximum pressure near $P_{avg} = 9.0GPa$. Finally, the R_m loading condition is observed to have a vastly different trend than the previous loading

conditions. In fact, the trend is opposite in that it is concave rather than convex. The rate at which temperature increases is much higher than the previously discussed loading conditions. Pressures above $P_{avg} = 10.0GPa$ are reached within $t = 0.05\mu s$, while the other loading conditions take the duration of simulation to reach values near this. This shows that loading conditions play a significant role in material responses. Although hot spot interactions were considered in the B_y loading condition it is apparent that multiple hot spot interactions provide a more reactive environment for the material.

Next Figure 4.64(b) shows temperature as a function of time. Again the C_1, C_2 and B_y loading conditions follow a similar trend while the R_m condition is vastly different. The C_2 and B_y loading condition are aligned through the duration of the simulation. The C_1 condition is slightly higher than these loading conditions and achieves a higher temperature at the end of the simulation. However, the slopes of these lines, or the rate at which temperature increases, are similar. It is also observed that the percentage of hot volume does not have a significant effect on these temperature profiles as they do with the pressure profiles. Finally, the random loading condition is considered. The rate at which temperature increases is significantly higher than the other loading conditions. The material system reaches on average temperature values near $T_{avg} = 2000K$ by $t = 0.05\mu s$. Again, this shows that loading conditions where multiple hot spot interactions occur are much more suitable for rapid energy release and initiation.

To complete this section, the solid mass fractions of HMX and binder are investigated. Figures 4.65(a)-4.65(b) show average mass fractions as a function of time for all loading conditions. Solid HMX mass fraction is shown on figure4.65(a). All curves initiate from the initial mass fraction of $\eta = 0.75$. As the solution progressives mass fraction decreases in all cases. Loading conditions C_2 and B_y perform similarly, where the rate of consumption of HMX is the smallest. The C_1 loading condition follows a similar trend however the rate of consumption of HMX is greater. The R_m case rapidly consumes HMX and has solid mass fractions below 30%. All other cases never fall below 40%. Again, this shows that multiple hot spot interactions are highly reactive. Figure 4.65(b) shows mass fraction of binder as a function of time. All trends initiate from $1 - \eta = 0.25$ binder content. As the solution progresses the binder is consumed with the loading conditions C_2 and B_y consuming the least amount of binder for the duration of the simulation. Again C_1 follows a similar trend but more binder is consumed. The final loading condition R_m shows a high consumption rate of average binder mass fraction. Binder fraction values reach below 9% while other simulations never fall below 13%. Again, these plots show that hot volume percentage may indicate material behavior however only for certain loading cases. Although all loading conditions started with the same average pressure and average

temperature, loading cases for heterogeneous material are a significant factor in responses especially where multiple hot spot interactions occur.

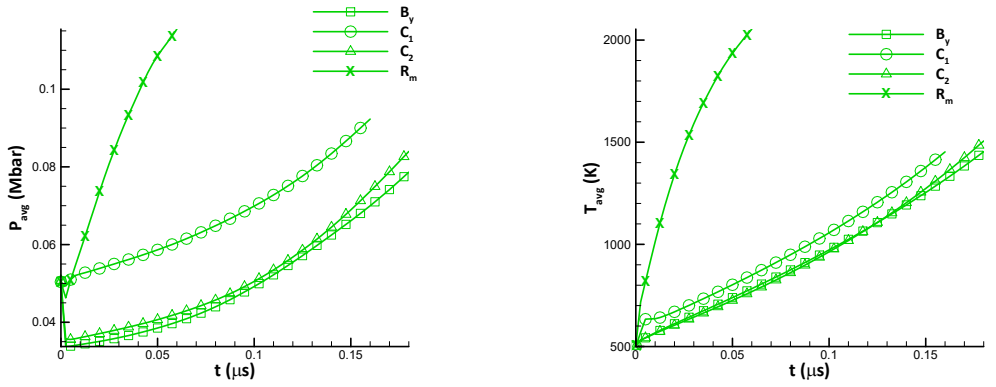

(a) Pressure (b) Temperature

Figure 4.64: Average pressure and temperature of the $\eta = 0.75$ material system as a function of time for each loading condition. Material response is different for varying loading conditions.

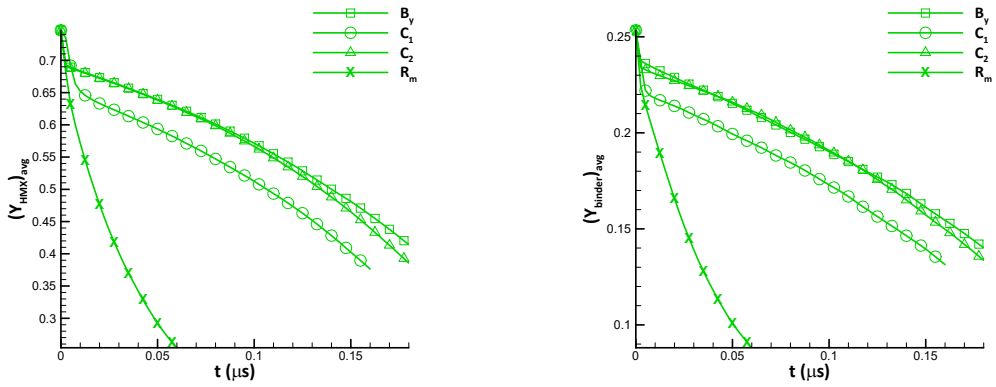

(a) HMX (b) Binder

Figure 4.65: Average mass fractions of the $\eta = 0.75$ material system as a function of time for each loading condition. Material response is different for varying loading conditions.

4.3.2 Numerical Results: $\eta = 0.85$

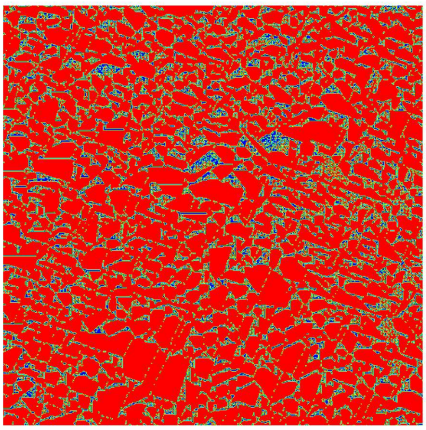

Figure 4.66: Computational representation of heterogeneous $\eta = 0.85$ material system where red represents HMX and blue represents binder.

In this section DNS results are presented for shock loading on the heterogeneous material system with a HMX mass fraction of $\eta = 0.85$. Contour plots of pressure, temperature, HMX mass fraction and binder fraction are shown on Figures 4.67(a)-4.82(d). These figures show the material response within $t = 0.01\mu s$ for all loading conditions. Contour plots for the remaining duration of the simulation are found in Appendix E.2.

Figures 4.67(a) through 4.68(d) show pressure and temperature contours for the C_1 loading condition. Like the previous case, material heterogeneity is displayed through non-uniform pressure and temperature distributions. Hot spots form in both plots with values reaching $50GPa$ and $3000K$. Figures 4.69(a) through 4.70(d) show solid mass fractions for HMX and binder. At the initial displayed time step, both HMX and binder are present in the shocked region. At the following time step, only a mixture of solid HMX in the shocked region is present while binder is fully burnt up. As the solution progresses HMX continues to be consumed.

Figures 4.71(a) through 4.74(d) show the C_2 loading condition. Pressure contours shown on 4.71(a) reach values near or above $50GPa$ again. The pressure contour shows a non uniform distribution however the temperature contour, with values above $3000K$, is uniform. Unlike the previous case the mass fractions for HMX and solid are fully converted to gaseous product by the initial displayed time step as shown on figures 4.73(a) and

4.74(a). Non-uniform pressure distributions are on display for the B_y loading condition on Figures 4.75(a) through 4.75(d), however uniform temperature distributions are shown on Figures 4.76(a) through 4.76(d). For the binary loading condition HMX and binder are fully converted to gaseous product within the shocked region by the initial displayed time step, as shown on Figures 4.77(a) through 4.78(d). The last loading condition, R_m is shown on Figures 4.79(a) through 4.82(d). Again the multiple hots pots produce non uniform distributions, and pressure and temperature values reach $50GPa$ and $3000K$. For the initial displayed time step a mixture of solid HMX is still present however binder is fully reacted within the multiple shocked regions. Average values for pressure, temperature and mass fraction are calculated from these plots and from the plots shown Appendix E.2.

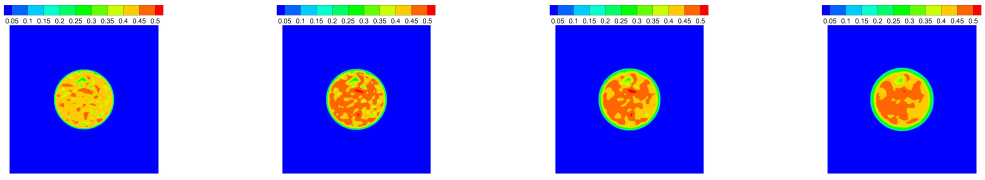

(a) t= 0.0025 (b) t= 0.0050 (c) t= 0.0075 (d) t= 0.0100

Figure 4.67: Pressure contours at initial shock loading of $\eta = 0.85$ heterogeneous material system at various time steps under C_1 loading condition

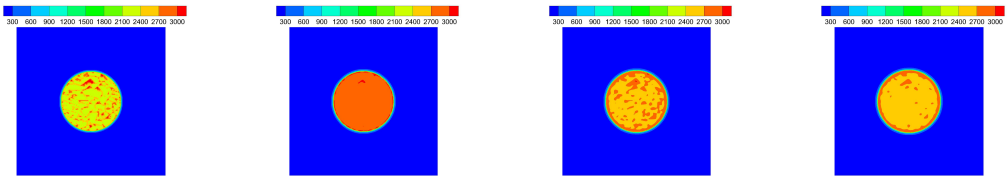

(a) t= 0.0025 (b) t= 0.0050 (c) t= 0.0075 (d) t= 0.0100

Figure 4.68: Temperature contours at initial shock loading of $\eta = 0.85$ heterogeneous material system at various time steps under C_1 loading condition

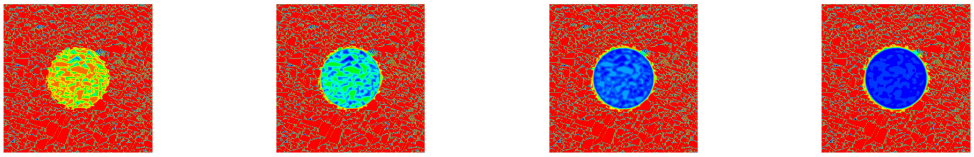

(a) t= 0.0025 (b) t= 0.0050 (c) t= 0.0075 (d) t= 0.0100

Figure 4.69: Solid HMX mass fraction contours at initial shock loading of $\eta = 0.85$ heterogeneous material system at various time steps under C_1 loading condition

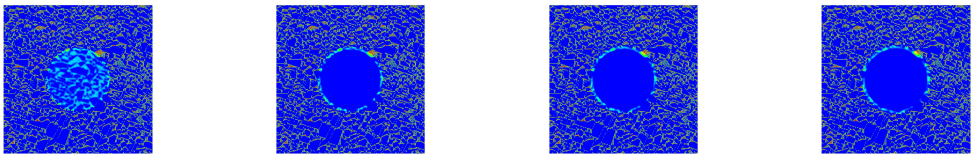

(a) t= 0.0025 (b) t= 0.0050 (c) t= 0.0075 (d) t= 0.0100

Figure 4.70: Solid binder contours at initial shock loading of $\eta = 0.85$ heterogeneous material system at various time steps under C_1 loading condition.

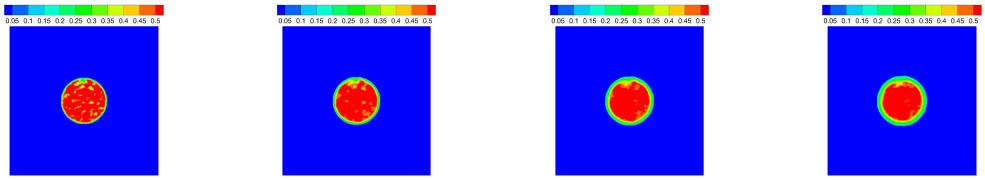

(a) t= 0.0025 (b) t= 0.0050 (c) t= 0.0075 (d) t= 0.0100

Figure 4.71: Pressure contours at initial shock loading of $\eta = 0.85$ heterogeneous material system at various time steps under C_2 loading condition

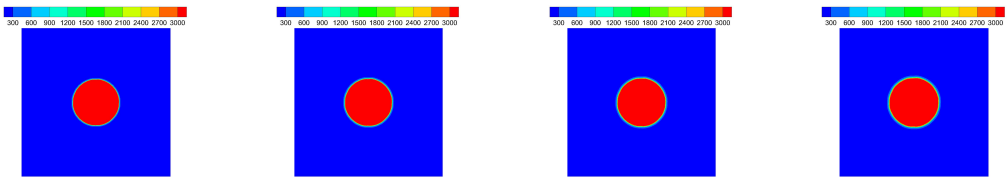

(a) t= 0.0025 (b) t= 0.0050 (c) t= 0.0075 (d) t= 0.0100

Figure 4.72: Temperature contours at initial shock loading of $\eta = 0.85$ heterogeneous material system at various time steps under C_2 loading condition

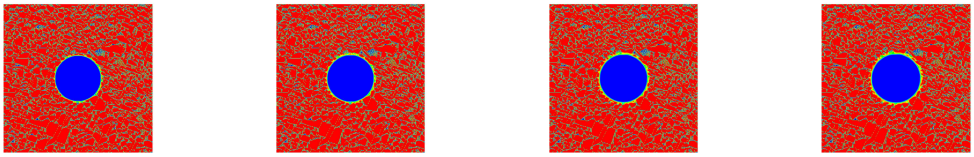

(a) t= 0.0025 (b) t= 0.0050 (c) t= 0.0075 (d) t= 0.0100

Figure 4.73: Solid HMX mass fraction contours at initial shock loading of $\eta = 0.85$ heterogeneous material system at various time steps under C_2 loading condition

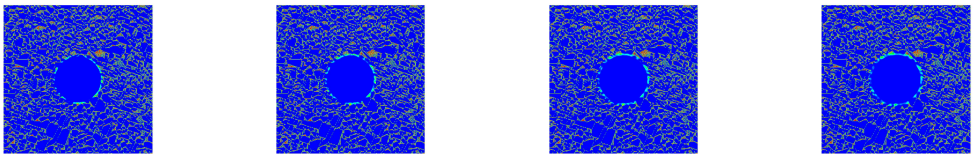

(a) t= 0.0025 (b) t= 0.0050 (c) t= 0.0075 (d) t= 0.0100

Figure 4.74: Solid binder contours at initial shock loading of $\eta = 0.85$ heterogeneous material system at various time steps under C_2 loading condition.

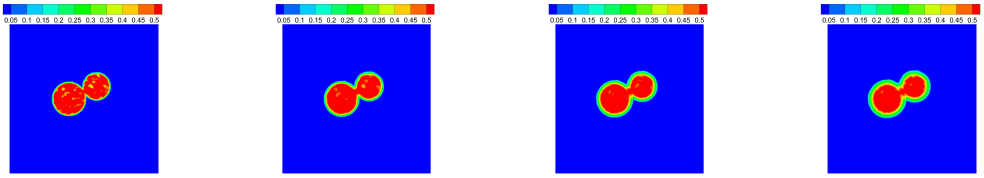

(a) t= 0.0025 (b) t=0.0050 (c) t= 0.0075 (d) t= 0.0100

Figure 4.75: Pressure contours at initial shock loading of $\eta = 0.85$ heterogeneous material system at various time steps under B_Y loading condition

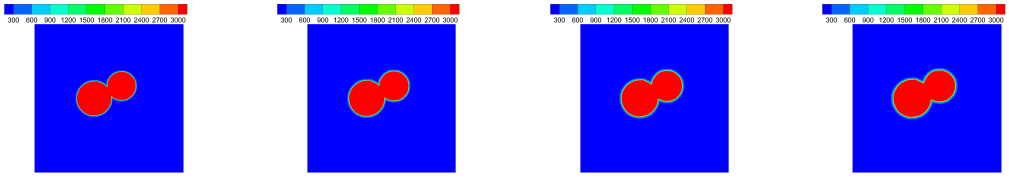

(a) t= 0.0025 (b) t= 0.0050 (c) t= 0.0075 (d) t= 0.0100

Figure 4.76: Temperature contours at initial shock loading of $\eta = 0.85$ heterogeneous material system at various time steps under B_Y loading condition

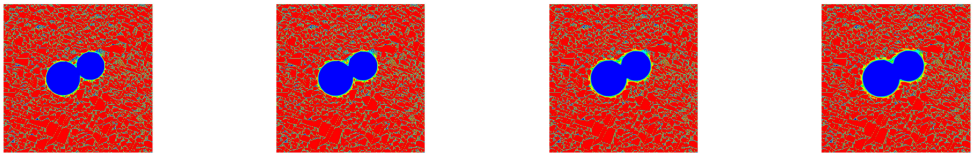

(a) t= 0.0025 (b) t= 0.0050 (c) t= 0.0075 (d) t= 0.0100

Figure 4.77: Solid HMX mass fraction contours at initial shock loading of $\eta = 0.85$ heterogeneous material system at various time steps under B_Y loading condition

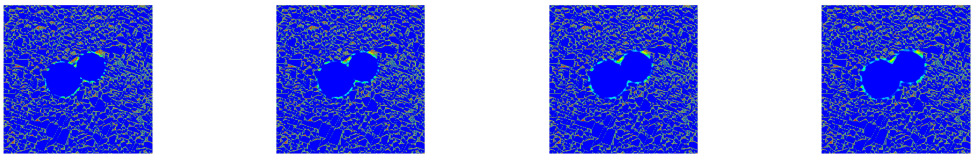

(a) t= 0.0025 (b) t= 0.0050 (c) t= 0.0075 (d) t= 0.0100

Figure 4.78: Solid binder contours at initial shock loading of $\eta = 0.85$ heterogeneous material system at various time steps under B_Y loading condition.

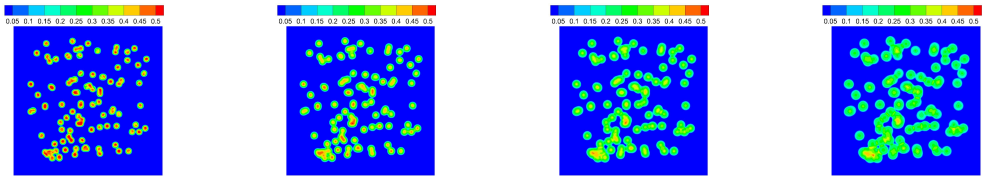

(a) t= 0.0025 (b) t=0.0050 (c) t= 0.0075 (d) t= 0.0100

Figure 4.79: Pressure contours at initial shock loading of $\eta = 0.85$ heterogeneous material system at various time steps under R_M loading condition

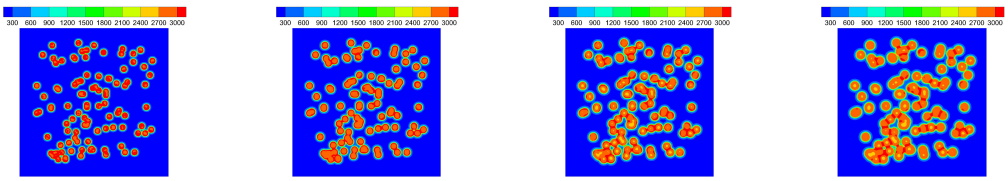

(a) t= 0.0025 (b) t= 0.0050 (c) t= 0.0075 (d) t= 0.0100

Figure 4.80: Temperature contours at initial shock loading of $\eta = 0.85$ heterogeneous material system at various time steps under R_M loading condition

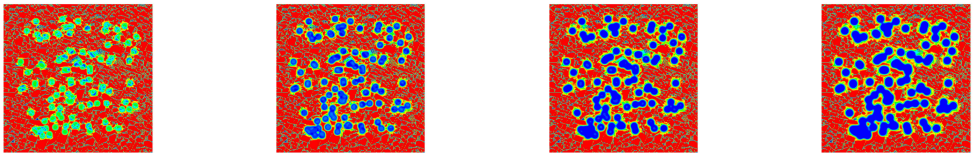

(a) t= 0.0025 (b) t= 0.0050 (c) t= 0.0075 (d) t= 0.0100

Figure 4.81: Solid HMX mass fraction contours at initial shock loading of $\eta = 0.85$ heterogeneous material system at various time steps under R_M loading condition

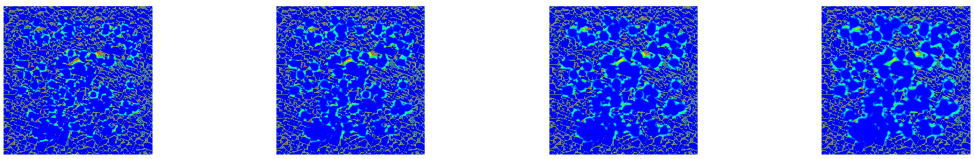

(a) t= 0.0025 (b) t= 0.0050 (c) t= 0.0075 (d) t= 0.0100

Figure 4.82: Solid binder contours at initial shock loading of $\eta = 0.85$ heterogeneous material system at various time steps under R_M loading condition.

Average values for pressure and temperature are shown for the $\eta = 0.85$ heterogeneous material system on Figures 4.83(a) and 4.83(b). Figure 4.83(a) shows pressure as a function of time. All pressures initiate from the initial average pressure of $P_{avg} = 5.0GPa$. As the solution progresses the C_2 and B_y loading conditions decrease in pressure. The pressure value recovers and begins to increase with time. Again these loading conditions align due to their percentages of hot volume. Unlike the previous loading cases the C_1 condition does not decrease in pressure and increases initially. As the solution progresses this loading condition reaches average values near $P_{avg} = 12.0GPa$, while the previous loading conditions reach $P_{avg} = 10.0GPa$. The rates at which pressure increases for the C_1, C_2 and B_y loading conditions are similar. The random loading condition, R_m is significantly different than the previous three loading conditions. The rate at which pressure increases is greater than C_1, C_2 and B_y. Near a value of $t = 0.05\mu s$ the R_m loading condition reaches $P_{avg} = 12.0GPa$. It takes an additional $0.1\mu s$ for the C_1 loading condition to achieve the same average value. Again this shows that loading conditions with multiple hot spot interactions provide significantly higher pressure increases.

Figure 4.83(b) shows average temperature as a function of time for all loading conditions. All curves initiate from the initial temperature of $500K$. The rate of increase is

similar for the C_1, C_2 and B_y loading conditions. However, the final temperature output achieved by the C_2 and B_y systems are less than that of the C_1 system. Again, percentages of hot volume may indicate material response for certain loading conditions. In the case of the temperature profile disparities of hot volume between the C_1, C_2 and B_y loading conditions aren't as significant as with the pressure profile. The rate at which the temperature increases for the R_m condition is significantly higher than the previous three loading conditions. The values achieved by this loading condition are never met by the other three conditions. This shows that loading conditions with multiple hot spot interactions play a role in the average performance for heterogeneous materials.

Finally Figures 4.84(a) and 4.84(b) show the rate of consumption for solid HMX and solid binder. Figure 4.84(a) shows solid mass fraction of HMX as a function of time where all curves initiate from the initial mass fraction of 85%. As time increases solid binder is consumed in all cases with the total amount of consumption for the R_m case being the fastest. For a total solid mass fraction near 30% the C_1 condition requires a duration near $t = 0.15\mu s$. However the same solid HMX content is achieved with the R_m condition within $t = 0.05\mu s$. The C_2 and B_y conditions never achieve a mass fraction below 40% in the given time. Figure 4.84(b) shows similar trends for the consumption of binder. All curves generate from the initial binder fraction of 15%.

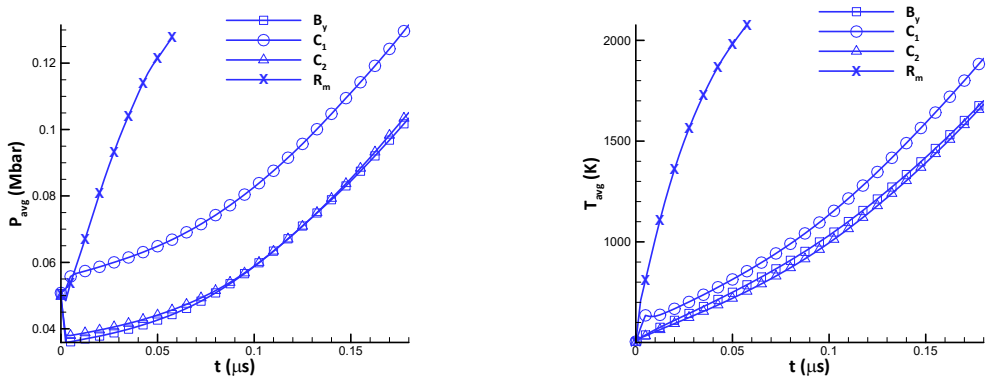

(a) Pressure

(b) Temperature

Figure 4.83: Average pressure and temperature of the $\eta = 0.85$ material system as a function of time for each loading condition. Material response is different for varying loading conditions.

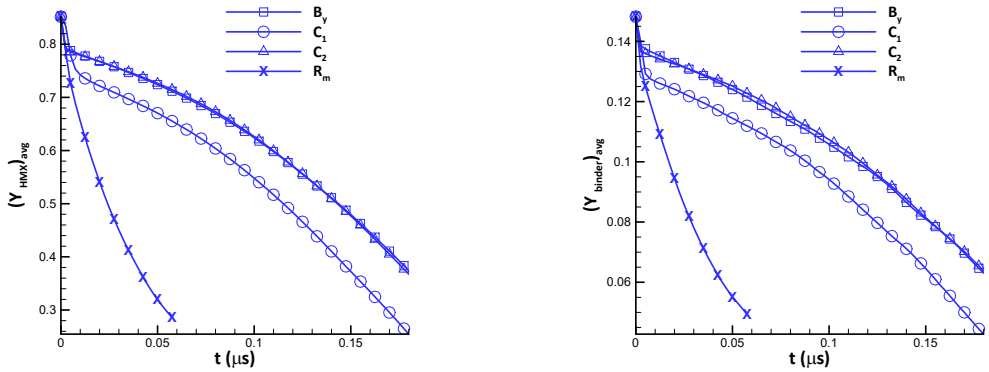

(a) HMX (b) Binder

Figure 4.84: Average mass fractions of the $\eta = 0.85$ material system as a function of time for each loading condition. Material response is different for varying loading conditions.

4.3.3 Numerical Results: $\eta = 0.95$

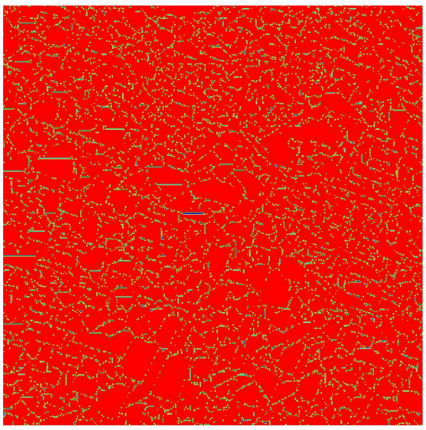

Figure 4.85: Computational representation of heterogeneous $\eta = 0.95$ material system where red represents HMX and blue represents binder.

In this section DNS results are presented for shock loading on the heterogeneous material system with a HMX mass fraction of $\eta = 0.95$. Contour plots of pressure, temperature, HMX mass fraction and binder fraction are shown on Figures 4.86(a)-4.101(d). These

figures show the material response within $t = 0.01\mu s$ for all loading conditions. Contour plots for the remaining duration of the simulation are found in Appendix E.3.

Figures 4.86(a) through 4.87(d) show contour plots for pressure and temperature for the C_1 loading condition. Although the material response is non uniform the values are not as varied as with the previous material systems. This is due to the fact that HMX content is dominating the material system, so the medium is nearly homogeneous. Pressure values reach $45GPa$ while temperature values exceed $2700K$ near the shock front. Figures 4.88(a) through 4.89(d) show the HMX and binder content of the material system. Initially both HMX and binder are present within the shocked region in the displayed time step. As time increases the HMX and binder are consumed, however binder is consumed at a much faster rate than the HMX. Figures 4.90(a) through 4.93(d) show the C_2 loading condition. Both pressure and temperature are uniformly distributed unlike the previous two material systems. Both HMX and binder fractions, shown on Figures 4.92(a) through 4.93(d), are fully converted within the initial displayed time step. Pressure and temperature profiles for the B_y loading condition shown on Figures 4.94(a) through 4.95(d), again, display a uniform distribution with values reaching $50GPa$ and $3000K$. Similar to the previous loading condition HMX and binder are fully reacted within the shocked region at the initial displayed time. Finally the R_m loading condition is displayed on Figures 4.98(a) through 4.101(d). Material heterogeneity is shown through pressure and temperature profiles. Hot spots are generated as non-uniform pressure and temperature distributions are displayed. HMX and binder mass fractions are shown on the final two plots where solid HMX is present on the initial plotted time step, and binder is fully consumed within the shock region.

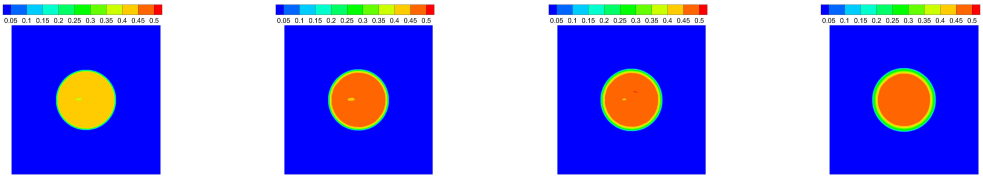

(a) t= 0.0025 (b) t= 0.0050 (c) t= 0.0075 (d) t= 0.0100

Figure 4.86: Pressure contours at initial shock loading of $\eta = 0.95$ heterogeneous material system at various time steps under C_1 loading condition

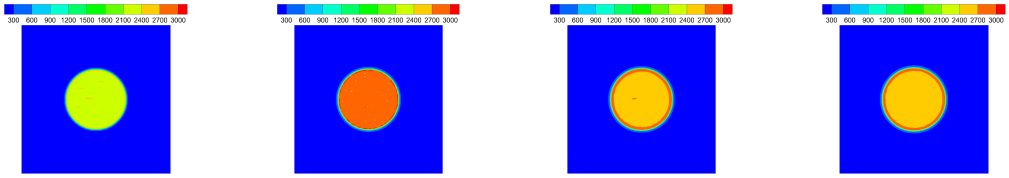

(a) t= 0.0025 (b) t= 0.0050 (c) t= 0.0075 (d) t= 0.0100

Figure 4.87: Temperature contours at initial shock loading of $\eta = 0.95$ heterogeneous material system at various time steps under C_1 loading condition

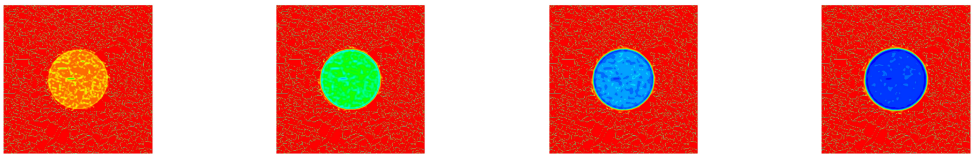

(a) t= 0.0025 (b) t= 0.0050 (c) t= 0.0075 (d) t= 0.0100

Figure 4.88: Solid HMX mass fraction contours at initial shock loading of $\eta = 0.95$ heterogeneous material system at various time steps under C_1 loading condition

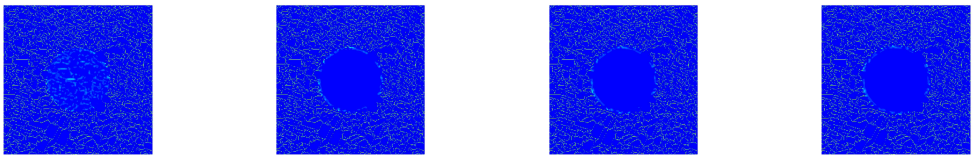

(a) t= 0.0025 (b) t= 0.0050 (c) t= 0.0075 (d) t= 0.0100

Figure 4.89: Solid binder contours at initial shock loading of $\eta = 0.95$ heterogeneous material system at various time steps under C_1 loading condition.

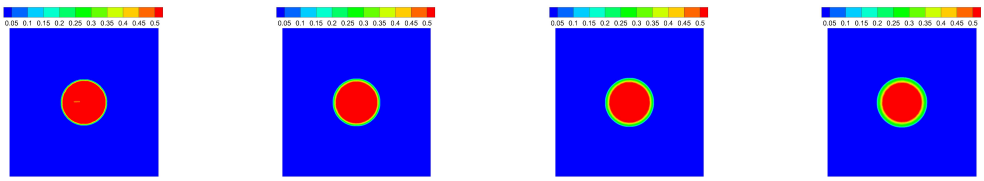

(a) t= 0.0025 (b) t= 0.0050 (c) t= 0.0075 (d) t= 0.0100

Figure 4.90: Pressure contours at initial shock loading of $\eta = 0.95$ heterogeneous material system at various time steps under C_2 loading condition

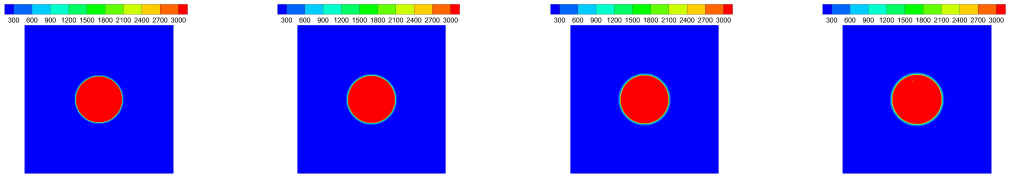

(a) t= 0.0025 (b) t= 0.0050 (c) t= 0.0075 (d) t= 0.0100

Figure 4.91: Temperature contours at initial shock loading of $\eta = 0.95$ heterogeneous material system at various time steps under C_2 loading condition

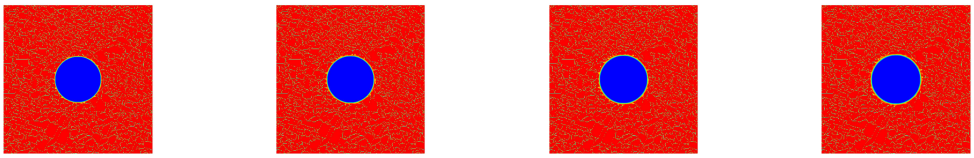

(a) t= 0.0025 (b) t= 0.0050 (c) t= 0.0075 (d) t= 0.0100

Figure 4.92: Solid HMX mass fraction contours at initial shock loading of $\eta = 0.95$ heterogeneous material system at various time steps under C_2 loading condition

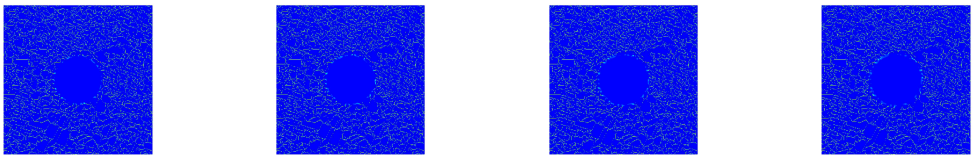

(a) t= 0.0025 (b) t= 0.0050 (c) t= 0.0075 (d) t= 0.0100

Figure 4.93: Solid binder contours at initial shock loading of $\eta = 0.95$ heterogeneous material system at various time steps under C_2 loading condition.

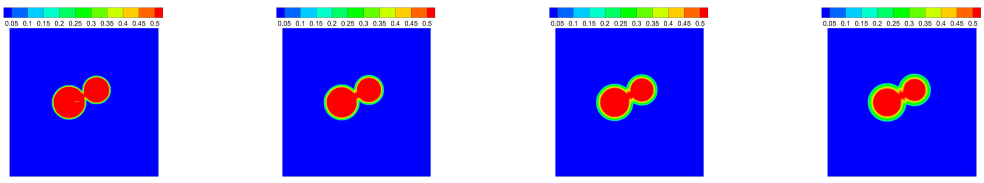

(a) t= 0.0025 (b) t=0.0050 (c) t= 0.0075 (d) t= 0.0100

Figure 4.94: Pressure contours at initial shock loading of $\eta = 0.95$ heterogeneous material system at various time steps under B_Y loading condition

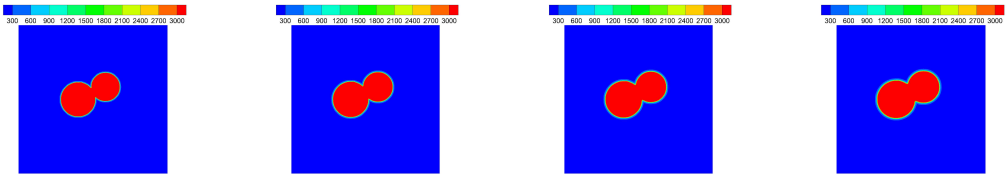

(a) t= 0.0025 (b) t= 0.0050 (c) t= 0.0075 (d) t= 0.0100

Figure 4.95: Temperature contours at initial shock loading of $\eta = 0.95$ heterogeneous material system at various time steps under B_Y loading condition

(a) t= 0.0025 (b) t= 0.0050 (c) t= 0.0075 (d) t= 0.0100

Figure 4.96: Solid HMX mass fraction contours at initial shock loading of $\eta = 0.95$ heterogeneous material system at various time steps under B_Y loading condition

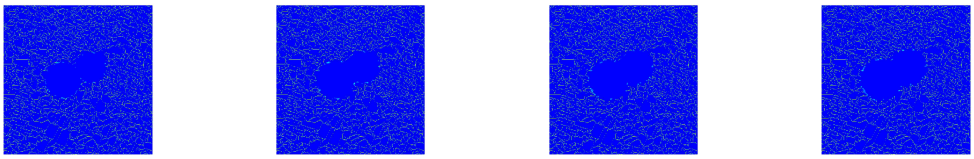

(a) t= 0.0025 (b) t= 0.0050 (c) t= 0.0075 (d) t= 0.0100

Figure 4.97: Solid binder contours at initial shock loading of $\eta = 0.95$ heterogeneous material system at various time steps under B_Y loading condition.

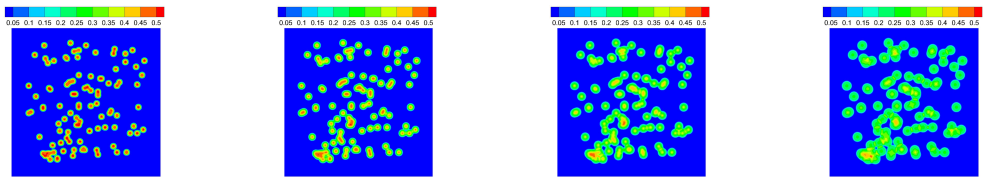

(a) t= 0.0025 (b) t=0.0050 (c) t= 0.0075 (d) t= 0.0100

Figure 4.98: Pressure contours at initial shock loading of $\eta = 0.95$ heterogeneous material system at various time steps under R_M loading condition

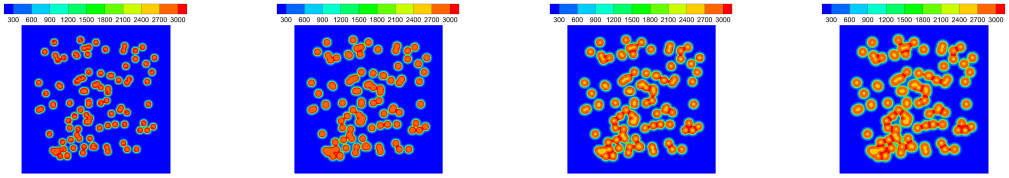

(a) t= 0.0025 (b) t= 0.0050 (c) t= 0.0075 (d) t= 0.0100

Figure 4.99: Temperature contours at initial shock loading of $\eta = 0.95$ heterogeneous material system at various time steps under R_M loading condition

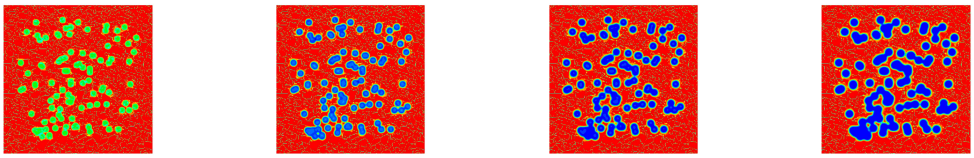

(a) t= 0.0025 (b) t= 0.0050 (c) t= 0.0075 (d) t= 0.0100

Figure 4.100: Solid HMX mass fraction contours at initial shock loading of $\eta = 0.95$ heterogeneous material system at various time steps under R_M loading condition

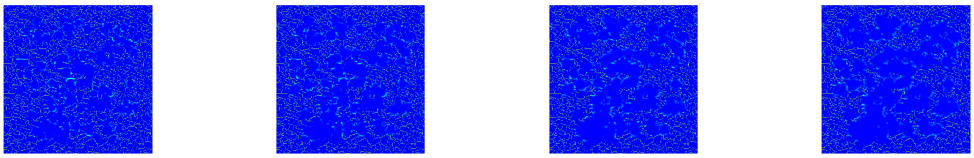

(a) t= 0.0025 (b) t= 0.0050 (c) t= 0.0075 (d) t= 0.0100

Figure 4.101: Solid binder contours at initial shock loading of $\eta = 0.95$ heterogeneous material system at various time steps under R_M loading condition.

Average values for pressure temperature and mass fractions are reported on a Figures 4.102(a) through 4.103(b). These averages were calculated from the previous plots and the plots shown in Appendix E.3. Figure 4.102(a) shows pressure as a function of time. All curves initiate from the initial average pressure of $P_{avg} = 5.0GPa$. As time increases pressure decreases for the C_2 and B_y loading condition. These loading conditions align throughout the duration of the simulation. The C_1 loading condition achieves higher pressure values than those observed by the previous two loading conditions. However the rates at which pressure increases for these loading conditions are similar. Again, the random

loading condition is significantly different than the other pressure profiles. The rate at which pressure increases is significantly greater than the previous loading conditions. An average value near $P_{avg} = 13.0GPa$ is achieved through the R_m loading condition by $t = 0.05\mu s$. The C_1 loading condition takes $t = 0.15\mu s$ to achieve this value and the C_2 and B_y loading conditions never reach this value within the simulation duration.

Temperature profiles are shown on Figure 4.102(b) for all loading conditions, where each curve initiates from an average temperature of $T_{avg} = 500K$. As the solution progresses C_2 and B_y loading condition align. The C_1 loading condition follows a similar trend but reaches greater temperature values than the previous two conditions. Again the rates of change in temperature are similar for these three conditions. The R_m loading condition achieves higher temperatures at a faster rate than the three previous conditions. The peak temperature achieved by the random loading condition is never met by the C_2 or B_y condition and takes a significantly longer time for the C_1 loading condition to reach this value.

Finally the rates at which solid HMX and binder are consumed are studied on Figures 4.103(a) and 4.103(b). 4.103(a) shows HMX content initiating from 95%. As time increases HMX is consumed and is converted to gaseous product. The lowest values achieved during this study are by the C_2 and B_y loading conditions. The rate at which HMX is consumed for these conditions is similar to the C_1 loading condition while the random loading condition consumes HMX at a much faster rate. The same trends are seen for binder consumption on Figure 4.103(b). Similar conclusions are drawn from those in the previous studies where loading conditions with similar hot volume content may behave similarly and loading conditions with multiple hot spot interactions produce the highest values of pressure and temperature.

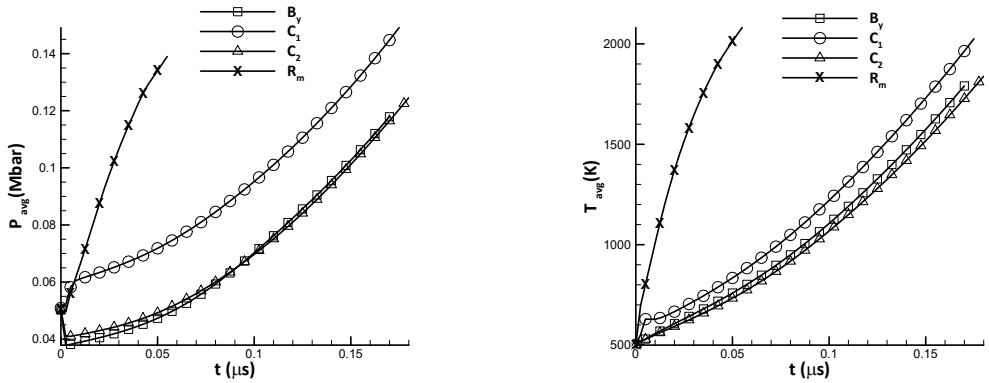

(a) Pressure (b) Temperature

Figure 4.102: Average pressure and temperature of the $\eta = 0.95$ material system as a function of time for each loading condition. Material response is different for varying loading conditions.

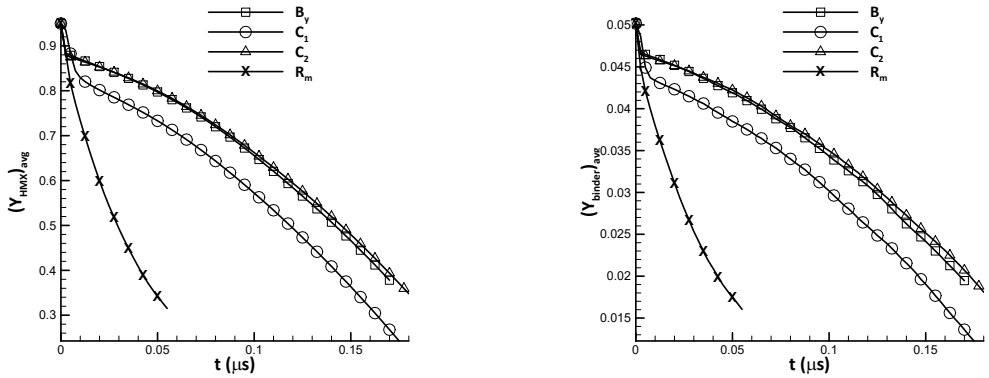

(a) HMX (b) Binder

Figure 4.103: Average mass fraction of the $\eta = 0.95$ material system as a function of time for each loading condition. Material response is different for varying loading conditions.

4.3.4 Numerical Results: Comparison

In this section, all material systems are compared including the continuum model. The continuum uses global reaction rates and the equation of State for PBX 9501. Reaction rates are shown on Table 3.4, from reference [106]. Pressure temperature and solid mass fractions are shown for all material systems for the C_1 loading condition on Figures 4.104(a), 4.104(b) and 4.105. Figure 4.104(a) shows average pressure as a function of time. The

first observation is that all material systems follow the same trend. All trends initiate from the initial average pressure of $P_{avg} = 5.0GPa$. Here the material system with 95% HMX produces the highest average pressure output, while the continuum produces the least. The continuum material system never achieves the pressure values obtained by the material systems that are heterogeneous. This shows that explicitly modeling the microstructure affects the average pressure output. The continuum performs most similarly to the heterogeneous material with the most binder content, $\eta = 0.75$. These two materials systems required the most energy per unit volume to achieve the desired average pressure of $P_{avg} = 5.0GPa$; however, they achieved the lowest pressure values. In other words, the continuum and the $\eta = 0.75$ material systems produce the least return in energy investment. Among heterogeneous material all systems follow the same trends. Increasing the HMX content increases the pressure output for the given duration. Increasing HMX in the composite, or decreasing binder content, increases sensitivity in terms of average pressure.

Figure 4.104(b) shows temperature profiles for the C_1 loading condition. Here the plots originate from the average temperature of $T_{avg} = 500K$. The continuum produces the least amount of average temperature output similar to the pressure profile. This shows that incorporating microstructural information leads to higher temperature values on average. Heterogeneous material systems perform similarly during the initial stages of the simulation however as time progresses these trends begin to diverge with $\eta = 0.75$ acting as the lower bound and $\eta = 0.95$ the upper. Increasing HMX mass fraction in the composite increases the sensitivity of the material in an average sense. Also observed is that the $\eta = 0.85$ and $\eta = 0.95$ material systems are more tightly bound then the $\eta = 0.75$ and $\eta = 0.85$ material systems showing the effects of more binder content.

Figure 4.105 shows the solid mass fraction of the C_1 loading condition for all material systems. The continuum explicitly solves the burn fraction transport equation in the Euler equations. The solid mass fractions for the composite materials are taken by summing the solid species of HMX in binder. Initially all materials consist of a pure solid composition. As time increases each material begins to react. Again for the heterogeneous materials the 75% and 95% HMX systems act as bounds. Higher binder content material shows smaller chemical reaction. The continuum model reacts the least within the given duration while the highest HMX content material reacts the most with close to 25% of the material converted to a pure gas. From these trends it is clear that microstructure plays an important role in average output for different quantities and that the continuum model under predicts the values when compared to the heterogeneous materials. These results also demonstrate the effect of binder content on average responses with composites with higher HMX fractions generating higher pressure, temperature and faster chemical reaction.

Figures 4.106(a), 4.106(a) and 4.105 show the C_2 loading condition for all material systems. Figure 4.106(a) shows pressure as a function of time. Initially the heterogeneous materials decrease from the initial average pressure. As time increases these values recover and begin to increase with time. The divergence between these curves begins to increase as a simulation continues with the $\eta = 0.95$ material system producing an upper bound of average pressure and the $\eta = 0.75$ material producing the lower bound. Again higher average pressure is achieved with materials with higher HMX content. During the simulation the $\eta = 0.95$ material system reaches a pressure near $P_{avg} = 12GPa$ while the $\eta = 0.75$ material system reaches $P_{avg} = 8GPa$. Initially the continuum system does not exhibit the same characteristics as the heterogeneous material systems; pressure only slightly decreases initially. As time progresses the continuum model crosses the heterogeneous materials and for the duration of $t = 0.1\mu s$ falls within the values of the heterogeneous material systems. In the previous loading condition these curves never achieved similar values. However the material system diverges after $t = 0.1\mu s$. Material systems that incorporate microstructural information show higher pressure values on average than those that do not for this loading condition.

Figure 4.106(a) shows average temperature for C_2 loading condition. Unlike the previous loading condition temperatures are indistinguishable within the first $t = 0.5\mu s$ of the simulation. It is assumed that because the loading condition requires a higher average per unit volume input than the previous case the, material responses are similar, as the effects of the microstructure do not have time to influence the materials response. However the effects of the microstructure can be seen as the simulation continues. Here the continuum method acts as a lower bound performing similarly to the heterogeneous material with the highest binder content. The composite with the most HMX content acts as the upper bound. It is also observed that the continuum system has a near-constant increase in the rate of temperature while the rate for the heterogeneous material systems are increasing. Heterogeneous material systems reach values near $T_{avg} = 1900K$ while the continuum system reaches a value near $T_{avg} = 1900K$.

Mass fractions of solid material are investigated on Figure 4.105. Here the HMX heavy composite is much more volatile than all other material systems with over 40% of the material reacting and becoming a gaseous product. The continuum reaches values near 75%. Again this demonstrates the drastic effect of including microstructural information in reactive burn models. Similar to the temperature profiles initially the rates at which solid material is consumed are indistinguishable and as a solution progresses these trends begin to diverge. The rate at which the continuum model changes is near-constant while the rate for the heterogeneous material systems increase with time.

Next the binary system is considered on Figures 4.108(a), 4.108(a) and 4.109. Due to their similar hot volume fractions this loading condition performs similarly to the previous C_2 loading condition. Therefore the same conclusions can be drawn. However for the R_m loading condition shown on Figures 4.110(a), 4.110(b) and 4.111 the same conclusions cannot be drawn when comparing to the similar hot volume fraction from C_1.

Figure 4.110(a) shows pressure as a function of time. All material systems follow similar trends where initially the pressure decreases with the greatest pressure decrease coming from the continuum system. Similar to the previous loading conditions the HMX heavy composite produces the highest average pressures with the continuum approach producing the lowest. However unlike the other loading conditions the continuum approach and the heterogeneous material with the largest binder content ($\eta = 0.75$) converge. This shows that for this loading condition the continuum model can achieve the same pressure values as a model that explicitly incorporates microstructural information. Figure 4.110(b) shows temperature as a function of time. Initially all heterogeneous material systems align for the first $t = 0.02\mu s$ of the simulation. After this point in time, the effects of the microstructure influence the trends with $\eta = 0.75$ and $\eta = 0.95$ material systems acting as the lower and upper bounds. The continuum model produces less temperature on average than the heterogeneous models for the majority of the duration of the simulation. However the gap between these values begins to close as time increases. Again the continuum model is able to achieve values near the heterogeneous model for this loading condition. Finally mass fractions for this loading conditions are studied on Figure 4.111. Initially all heterogeneous material systems align. Near the same point in time, the effects of the microstructure take over and these trends begin to deviate with the $\eta = 0.95$ system becoming the most volatile. Similar to the previously studied loading conditions, the continuum model consumes the least amount of solid mass fraction. This shows that the continuum model on average can produce similar pressure and temperature profiles to those of heterogeneous material systems while being the least reactive. These plots show that microstructural information plays a role in average material performance for varying loading conditions. For certain loading conditions the continuum model is vastly different than the heterogeneous material systems and may never achieve pressure, temperature and burn fractions as those for heterogeneous material systems. However, for loading conditions with multiple hot spot interactions it is possible. These trends also show that increasing binder content decreases the sensitivity of each heterogeneous material. Material systems that require higher input energy per unit volume have the lowest performance in terms of pressure and temperature output showing a higher return on energy investment for HMX heavy content materials. This study showed that material systems with the same average initial conditions behave

differently depending on how the material is loaded. These results have implications for material by design.

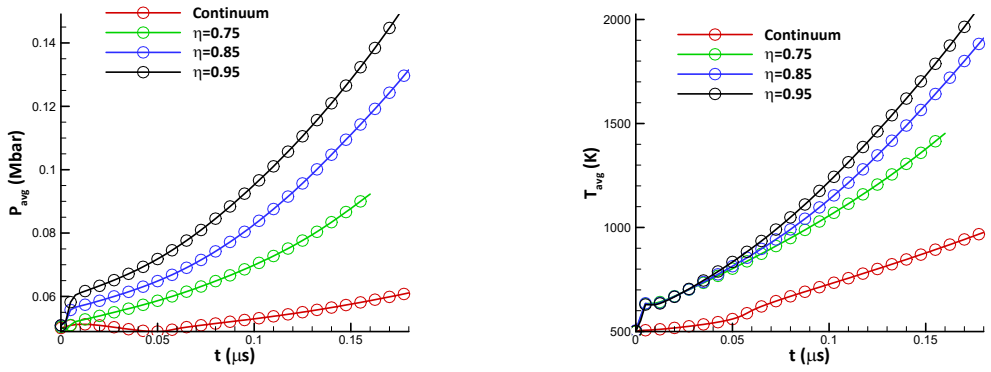

(a) C_1 Pressure (b) C_1 Temperature

Figure 4.104: Average pressure and temperature of all material systems as a function of time for C_1 loading condition. Response varies for each material system.

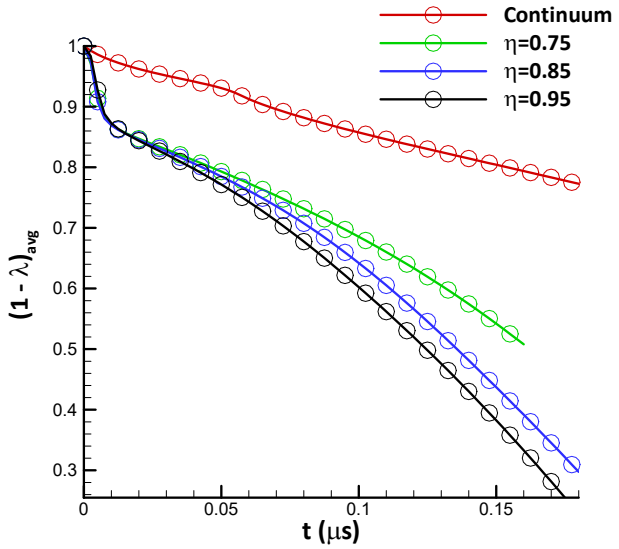

Figure 4.105: Average mass fraction of all material systems as a function of time for C_1 loading condition. Response varies for each material system.

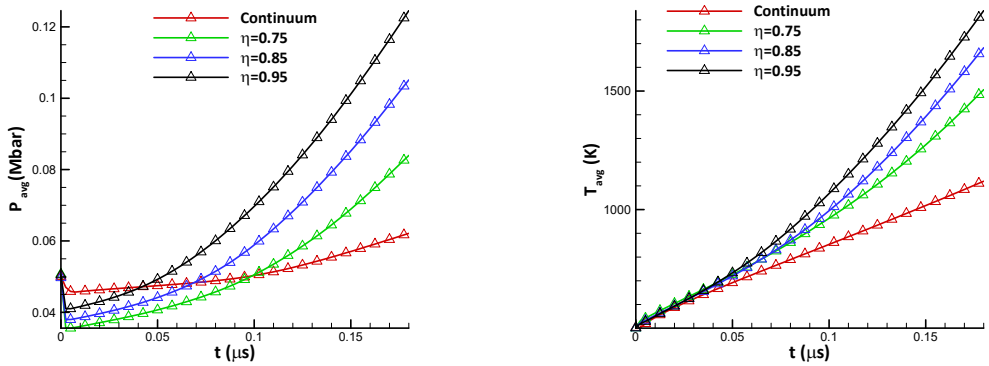

(a) C_2 Pressure (b) C_2 Temperature

Figure 4.106: Average pressure and temperature of all material systems as a function of time for C_2 loading condition. Response varies for each material system.

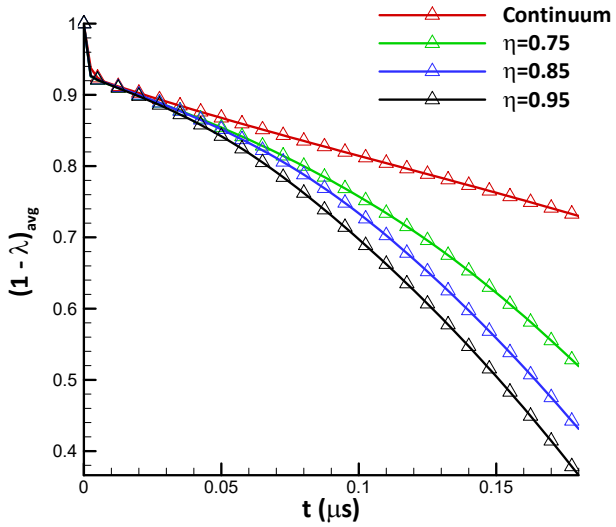

Figure 4.107: Average mass fraction of all material systems as a function of time for C_2 loading condition. Response varies for each material system.

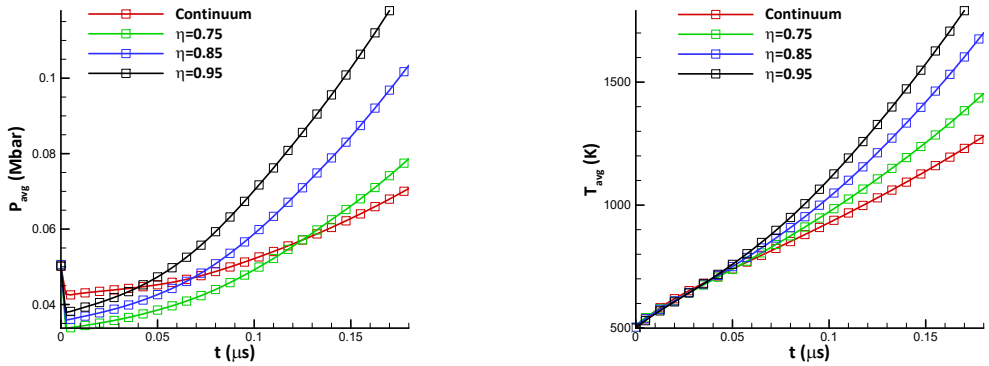

(a) B_y Pressure

(b) B_y Temperature

Figure 4.108: Average pressure and temperature of all material systems as a function of time for B_y loading condition. Response varies for each material system.

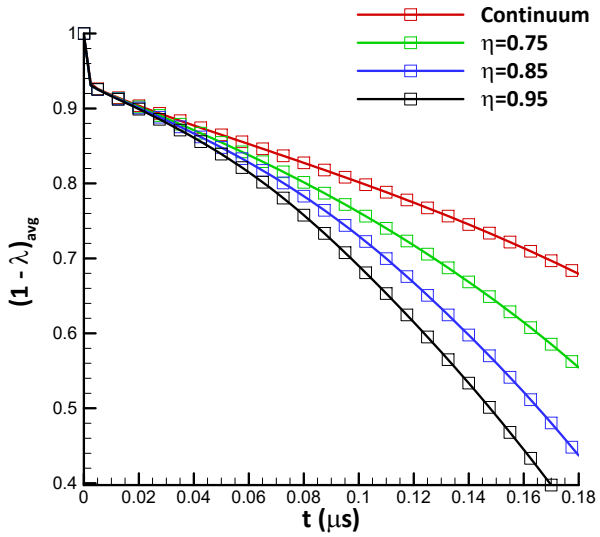

Figure 4.109: Average mass fraction of all material systems as a function of time for B_y loading condition. Response varies for each material system.

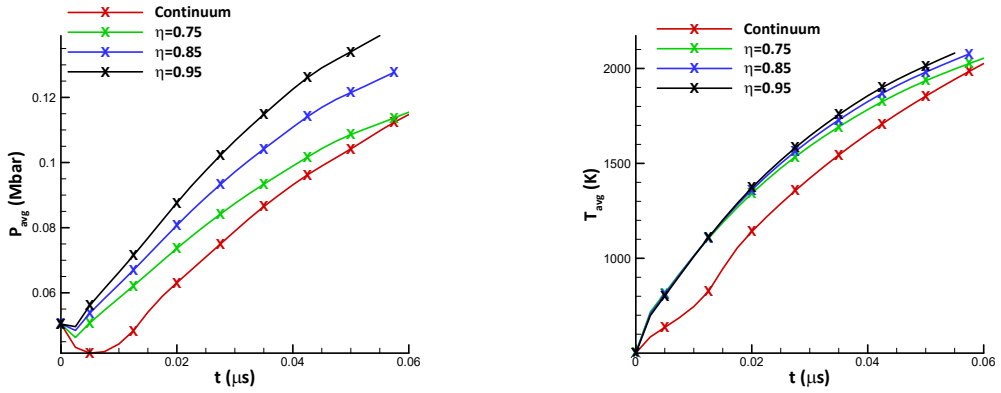

(a) R_m Pressure

(b) R_m Temperature

Figure 4.110: Average pressure and temperature of all material systems as a function of time for R_m loading condition. Response varies for each material system.

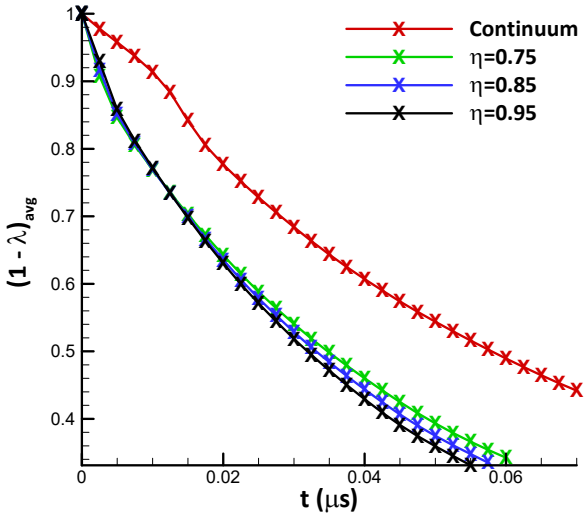

Figure 4.111: Average pressure and temperature of all material systems as a function of time for R_m loading condition. Response varies for each material system.

To close out this Chapter, performance and safety are investigated for each material. Figures 4.112(a) and 4.112(b) show pressure and temperature as a function of initial average energy per unit volume. Here, the pressure and temperature values reported are for $t = 0.16\mu s$ for the C_1, C_2 and B_y loading conditions. For the much more volatile R_m loading condition the values reported are for $t = 0.05\mu s$. These plots give a "snap shot"

of material performance, measured in pressure and temperature, and safety, measured in input average energy per unit volume. Note, there is not distinction between loading conditions on these plots. The ideal explosive would be safe (require less input energy) and high performing (high pressure and temperature values). In general these plots show that performance and safety are at competition with each other, where the relationship is linear. Safer materials require higher input energy per unit volume. Higher performing materials produce larger pressure and temperature values at the reported time. Of the material systems studied, it is observed that the HMX heavy materials have better performance than the materials with more binder content. However, these high performing material systems require much less initial energy per unit volume to reach these values, indicating that they are less safe. On the other side of the spectrum are materials with higher binder content. These material systems ($\eta = 0.75$) require much more initial input energy per unit volume, indicating that accidental detonation is much less likely to occur. However their output pressures and temperatures are not as high as the HMX heavy materials.

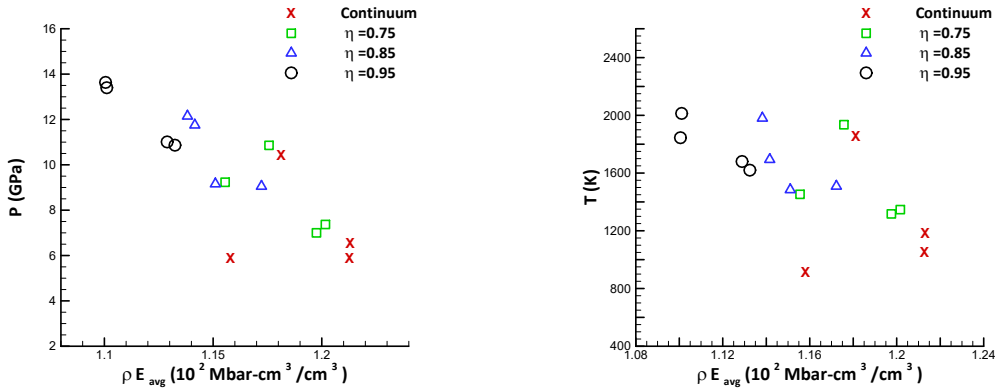

(a) Pressure

(b) Temperature

Figure 4.112: "Snap shot" of material performance, measured in pressure and temperature, and safety, measured in input average energy per unit volume for all material systems. Performance and safety are at competition.

4.4 Summary

This chapter presented Direct Numerical Simulation (DNS) of shock loading of polymer bonded explosives. Material heterogeneities were explicitly modeled through synthetic microstructures generated using a Markov Random Field approach. Synthetic microstructures were generated with varying HMX/binder content. Initiation of these microstructures

and a continuum were studied for four different loading conditions. Results showed that material systems with the same average initial conditions behave differently depending on how the material is loaded. Material systems with higher binder content required more energy per unit volume to achieve the same average pressures and temperatures reached by other heterogeneous material systems. It was also observed that the continuum model performed similarly to higher binder content material systems upon initiation. Numerical results showed that hot volume percentage may indicate material behavior however only for certain loading cases. Although all loading conditions started with the same average pressure and average temperature, loading cases for heterogeneous material are a significant factor in responses especially where multiple hot spot interactions occur. Hot volume percentages do not correlate to performance. For certain loading conditions the continuum model was vastly different than the heterogeneous material systems and never achieved pressure, temperature and burn fractions values like those of the heterogeneous material systems. However, for loading conditions with multiple hot spot interactions it was possible. These results also showed that increasing binder content decreases the sensitivity of the heterogeneous material. Material systems that require higher input energy per unit volume have the lowest performance in terms of pressure and temperature output showing a higher return on energy investment for HMX heavy content materials. This shows the material performance is at competition with material safety.

CHAPTER 5

First-Order Multiscale Modeling

This chapter presents First-Order Multiscale modeling of shock loading of polymer bonded explosives. These methods explicitly model material heterogeneities in the average sense. Section 5.1 presents the multiscale approach used where varying resolutions of the microstructure are considered. Section 5.2 presents numerical results for all material systems under various loading conditions. These results are compared to results obtained using the Direct Numerical Simulation approach discussed in Chapter 4. The Chapter closes by comparing performance versus safety results for all methodologies, including the continuum approach. Finally, computational cost for each methodology is investigated.

5.1 Multiscale Approach

The multiscale linking methodology considered here is called "computational homogenization" [97, 98, 100, 101]. The approach is general and allows one to embed micro-scale simulations into continuum simulations. The idea of computational homogenization is to start with a continuum problem and find the missing information in the form of material properties by performing local simulations of the microscale models. Properties at a point in the coarse-scale(continuum) can be obtained from a fine-scale unit cell (with finite volume). In this work, the continuum fields are passed to the micro-scale and uniformly distributed. Continuum fluxes and properties (at all integration points) are computed from the underlying microstructural sub-problem using averaging schemes. The term"First-Order" signifies that volume averages are used to measure the effects of the microstructure, as opposed to "Full-Order" where equilibrium is enforced on the micro-scale. The approach used in this work allows for straightforward incorporation of physical and geometrical nonlinearities in material response and is based on the direct extraction of the constitutive behavior from the heterogeneity of a material. This provides significantly faster computational time than a direct numerical simulation.

To further illustrate the differences between the previous methodologies considered in this work, all approaches are graphically depicted on Figures 5.1(a) -5.1(c). Here the finite element mesh is represented by the red grid over the domain. Figure 5.1(a) depicts the continuum approach described in Chapter 3. Continuum methods are most common in engineer applications as they require the lease amount of fidelity. This is due to the fact that no microstructural information included as homogenized material properties are considered. Within each finite element, material properties are uniform. Furthermore, within the entire domain material properties are uniform. Figure 5.1(b) depicts the Direct Numerical Simulation (DNS) approach described in Chapter 4. DNS requires the highest fidelity among presented methods and is computationally intractable at engineering levels. High fidelity is required as the microstructure is explicitly modeled. This method is assumed to be the most accurate as it takes the full effects of the microstructure in to account. Within each finite element, and over the entire domain, material properties vary. Figure 5.1(c) shows the multiscale approach considered in this chapter. In general, the First-Order model attempts to capture the "best of both worlds"; the computational efficiency of the continuum approach and the microstructural effects of DNS. Microstructural effects are found by taking volume averages of quantities at each integration point within the finite element mesh. However, unlike DNS, a homogenized transport equation for burn fraction(λ), or a global rate, is considered, and each species is not explicitly modeled.

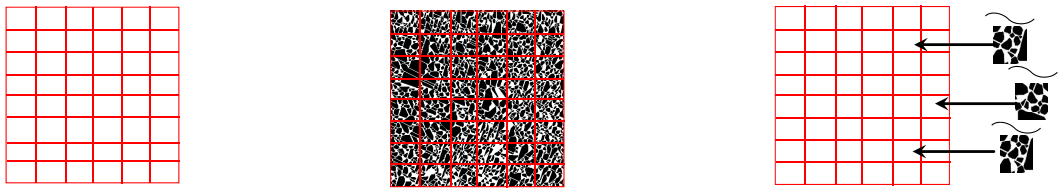

(a) Continuum (b) DNS (c) First-Order

Figure 5.1: Schematic of methodologies considered in this work. Continuum methods(a) require the least amount of fidelity and use modified material constants and treat HMX and binder as one material. Direct Numerical Simulation(b) requires the highest amount of fidelity and explicitly models the microstructure. First-Order multiscaling(c) approach uses volume averaging schemes to incorporate micro-scale effects.

For First-Order Multiscaling, the Euler Equations 2.18 are numerically solved using the Taylor-Galerkin Scheme described in Chapter 2.2. The microstructure is not explicitly modeled and two species exist: solid unreacted explosive and fully reacted gaseous products. Here, λ represents the fractions of gaseous product with in the cell or element.

However, microstructural effects are incorporated by taking volume averages of pressure and temperature. The 2D reactive Euler equations for the multiscale model are given as

$$\mathbf{U} = \begin{bmatrix} \rho \\ \rho u \\ \rho v \\ \rho E \\ \rho \lambda \end{bmatrix}, \qquad \boldsymbol{F_1} = \begin{bmatrix} \rho u \\ \rho u^2 + \widetilde{P} \\ \rho uv \\ (\rho E + \widetilde{P})u \\ \rho u \lambda \end{bmatrix}, \qquad \boldsymbol{F_2} = \begin{bmatrix} \rho v \\ \rho vu \\ \rho v^2 + \widetilde{P} \\ (\rho E + \widetilde{P})v \\ \rho v \lambda \end{bmatrix},$$

$$and \quad \mathbf{S} = \begin{bmatrix} 0 \\ 0 \\ 0 \\ q\rho\dot{\lambda} \\ \rho\dot{\lambda} \end{bmatrix} \tag{5.1}$$

where

$$\widetilde{P} = \frac{1}{V}\int_V P\, dV \tag{5.2}$$

the volume average of pressure. The global reaction rate is a function of local temperature where subscripts denote the material; thus,

$$\dot{\lambda} = \frac{1}{V}\int_V (1-\lambda)_H Z_H e^{-E_{H1}/RT_H}\, dV + \frac{1}{V}\int_V (1-\lambda)_B Z_B e^{-E_{B1}/RT_B}\, dV. \tag{5.3}$$

Averages are taken by considering equations of state for solid HMX, fully reacted gaseous HMX, solid polymeric binder and gaseous polymeric binder. Weights for these averages are determined from the resolution parameter ϕ, where each mass fraction η has a corresponding resolution parameter. Essentially, the parameter ϕ further discretizes the microstructure by $\phi \times \phi$. As an example take the synthetic microstructure with the mass fraction of $\eta = 0.75$ from Figure 4.7(a). The microstructure, as represented here has a resolution parameter of $\phi = 640$, the number of pixels across the axis. This is shown Figure 5.2(a) and is the microstructure used in DNS simulations in the previous chapter. If the parameter is decreased, this coarsens the resolution of the microstructure. The binary representation is lost and material properties are weighted on the "darkness" of each cell, where black represents pure HMX(100%) and white represents pure binder(0%). Shades of grey lie in between these two extremes. Figures 5.2(b), 5.2(c) and 5.2(d) show the microstructure at varying ϕ levels (shown in caption). By reducing the resolution parame-

ter, material heterogeneity decreases and the material becomes more uniform; information from the micro-scale is lost. However, the percentage of HMX content on average remains the same, $\eta = 0.75$. Reducing the parameter further to $\phi = 1$ produces a microstructure where material parameters no longer vary spatially; i.e. a homogenized continuum. It is important to note that the resolution parameter ϕ has no effect on mesh density.

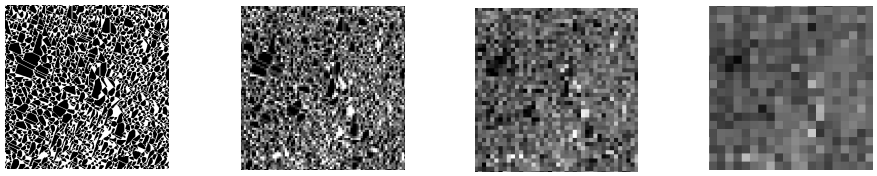

(a) $\phi = 640$ (b) $\phi = 80$ (c) $\phi = 40$ (d) $\phi = 20$

Figure 5.2: $\eta = 0.75$ synthetic microstructure with varying ϕ levels. Decreasing ϕ reduces material heterogeneity, however the overall HMX content remains unchanged.

In this work, two main resolution parameters are considered for all material systems and all loading conditions. The resolution parameter of $\phi = 50$ is selected to correspond to an order of magnitude difference in finite element mesh size (500×500 triangular elements), a common practice in multiscale modeling. The other resolution parameter considered is the extreme of $\phi = 1$, where all material heterogeneity is lost and the material properties are uniform. The other extreme of $\phi = 500$ is considered in special circumstances for investigative purposes later in the chapter as specified. The computational representation of the micro-scale information is shown on Figures 5.3(a), 5.3(b) and 5.3(c) for material systems with overall mass fractions of 75%, 85% and 95% respectively. Note the change in color map for the $\eta = 0.95$ case. Figures for the $\phi = 1$ cases are not shown as they would only be a single color.

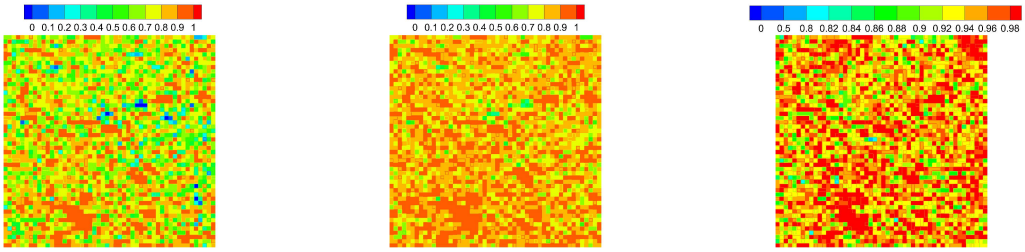

(a) $\eta = 0.75$ (b) $\eta = 0.85$ (c) $\eta = 0.95$

Figure 5.3: Computation representation of microstructural information for various material systems with resolution parameter $\phi = 50$.

Similar to the shock initiation experiments conducted in Section 4.2, density and total specific energy is varied to study the effects on average pressure and temperature over the entire domain. Contour plots for average pressure and average temperature are shown in Appendix F.1 for all material systems. These results are similar to the previous study and will not be explored further. The target values of $P_{avg} = 5GPa$ and $T_{avg} = 500K$ are considered again. Initial density and total specific energy are tabulated in Appendix F.1 for all material systems. The average energy per unit volume is reported on Figure 5.4 for all material systems and loading conditions. Note, the results for $\phi = 500$ are the same results reported for DNS on Figure 4.45. These results are similar to the previous study; therefore, similar conclusions are drawn. In general, percentage of hot volume plays a role. Next, numerical simulation is performed for all material systems and all loading conditions.

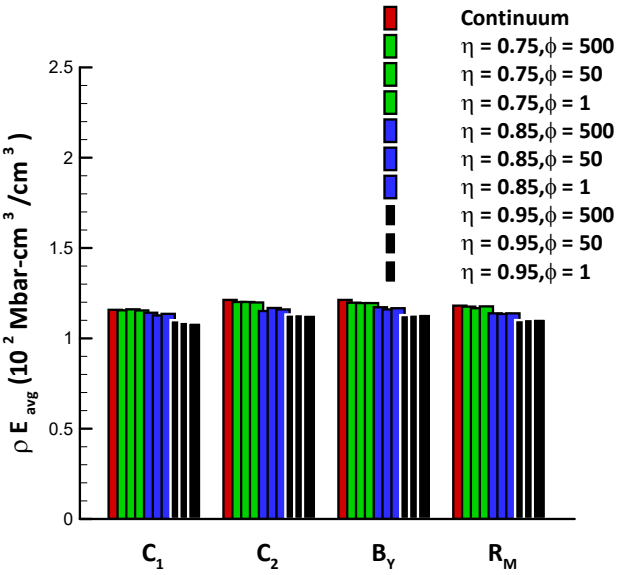

Figure 5.4: Average energy per unit volume of all material systems for each loading condition where $P_{avg} = 5GPa$ and $T_{avg} = 500K$. Resolution parameter ϕ has little no effect on the initiation.

5.2 First-Order Numerical Results

This section presents numerical results for shock loading on heterogeneous material systems using First-Order Multiscale approach. A uniform mesh, using 3-noded constant strain triangle elements, is considered with a mesh density of $2,000ELM/cm$. With 5 local degrees of freedom, and $251,001$ nodes the global number of degrees of freedom is

$1,255,005$. A constant time step of $\Delta t = 1e-5\mu s$ for a duration of $t = 0.16\mu s$. Computationally, the solution procedure for all results used 8 computational nodes with 16 cores each for a total number of 128 processes. Computational cost information for each study will be investigated in the final section.

5.2.1 Numerical Results: $\eta = 0.75$, $\phi = 1, 50$

In this section numerical results from the multiscale approach are presented for shock loading on the heterogeneous material system with a HMX mass fraction of $\eta = 0.75$. Here, resolution parameters of $\phi = 50$ and $\phi = 1$ are considered. Figures 5.5(a)-5.8(b) show pressure and temperature profiles for all loading conditions. Averages responses were obtained by integrating pressure and temperature contours over time. For the sake of brevity contour plots are not shown for each loading condition.

Figures 5.5(a) and 5.5(b) and show pressure and temperature plots for the C_1 loading condition. These figures show both the DNS approach and the multiscale approach. Figure 5.5(a) a shows average pressure as a function of time. Both methodologies show that the average pressure response initiates from the average pressure of $P_{avg} = 5GPa$. As time increases the responses begin to diverge. The DNS response produces lower pressure values than the multiscale approach in general. The difference between the resolution parameters $\phi = 50$ and $\phi = 1$ is attributed to the loss in material heterogeneity. As the resolution parameter decreases the material becomes more homogeneous and the response increases. On the other hand increasing the resolution parameter, $\phi = 50$, increases the material heterogeneity and the results are closer to the DNS approach which explicitly models than microstructure. Still there is a gap between the $\phi = 50$ parameter results and the DNS results. Again this can be attributed to the lack of heterogeneity in the information fed into the multiscale approach. This shows that between DNS and the multiscale approach information from the microstructure is lost since λ is the same for both HMX and binder in First-Order multiscale. Still, both approaches follow similar trends as pressure increases as a function of time; however, the rates at which pressure increases is significantly higher for the multiscale approach when compared to the DNS approach. Figure 5.5(b) shows the temperature profile as a function of time for the C_1 loading condition. Both methodologies originate from the initial average temperature of $T_{avg} = 500K$. As the solution progresses the methods begin to diverge similar to that of the pressure plot. Again the multiscale approaches are bound tightly together while the DNS approach is slightly less reactive. The rates at which temperature increase is higher for the multiscale approach than the DNS approach.

Figure 5.6(a) and 5.6(b) show the C_2 loading condition for both approaches. Figure 5.6(a) shows pressure as a function of time. Again all methodologies originate from the $P_{avg} = 5GPa$ initial loading condition. As time increases pressure decreases initially. Within the first $t = 0.05\mu s$ all approaches are tightly bound. In fact, the multiscale approach with the resolution parameter of $\phi = 50$ is nearly identical to the DNS approach. This shows that within this time span the difference in the material heterogeneity is not as crucial. However after this point the solutions diverge. The multiscale approach increases with pressure at a faster rate than the DNS approach similar to the previous loading condition. The multiscale approaches are tightly bound. The gap between these two results shows that the difference in material heterogeneity plays a role in material response. Again, by increasing the material heterogeneity in the multiscale approach, the solution approaches the DNS results, while decreasing the resolution parameter makes a material homogeneous and essentially a homogenized continuum.

Figure 5.6(b) shows temperature profiles as a function of time. All solutions initiate from the average temperature of $T_{avg} = 500K$. The solutions all follow similar trends again with temperature increasing as a function of time. All approaches are initially tightly bound however, unlike pressure, the multiscale approach with the highest resolution does not line up with the temperature profile of the DNS solution. However both multiscale approaches are nearly indistinguishable within the first $t = 0.1\mu s$. After this point the solutions diverge and the difference between the resolution parameters is small. Here the DNS approach produces lower temperature values then the multiscale approach.

Next the B_y loading condition is considered where Figure 5.7(a) and 5.7(b) show pressure and temperature profiles. Figure 5.7(a) a shows pressure as a function of time for all approaches. Again, these figures follow similar trends to the previous loading conditions. However, unlike the previous loading conditions, these pressure profiles do not line up within the initial $t = 0.05\mu s$s. Similar conclusions can be drawn from this plot as the two previous. Figure 5.7(b) shows temperature as a function of time. These results are similar to the previous two studies where the multiscale approaches are tightly bound in their response while the DNS approached diverges and produces smaller values for temperature within the given duration of the simulation. For both plots it observed that decreasing material heterogeneity increases both pressure and temperature profiles while increasing the resolution parameter, and thus increasing ϕ, the solution approaches the DNS results.

Finally the R_m loaning condition is studied on Figures 5.8(a) and 5.8(b). Figure 5.8(a) shows pressure profiles for both the DNS approach and the multiscale approach. Both methodologies follow a very similar trend in that pressure increases as a function of time. Although these solutions do not line up, the solutions are tightly bound and the differ-

ence between both approaches is less apparent than in the previous studies. Still the DNS approach produces smaller pressure values than the multiscale approach. The multiscale Solutions are tightly bound and the difference between the two solutions shows the effect of including microstructural information. Similarly, the temperature profile shown in figure 5.8(b) mimics this behavior.

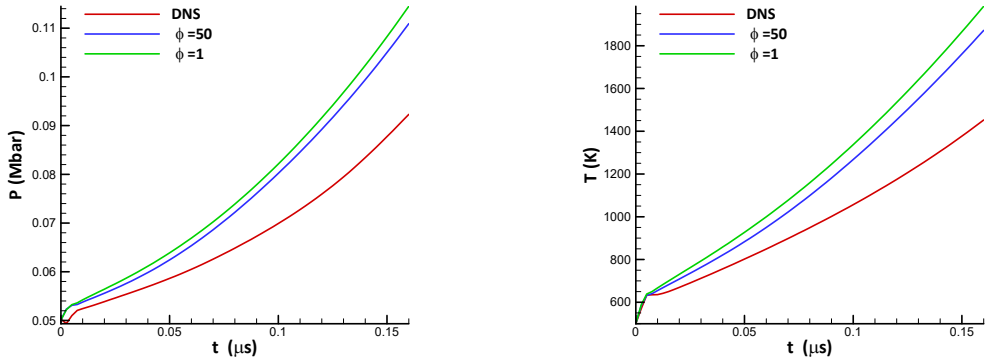

(a) Pressure (b) Temperature

Figure 5.5: Numerical results for First-Order Multiscale approach using resolution parameters $\phi = 50$ and $\phi = 1$. Results for $\eta = 0.75$ material system under C_1 loading conditions are compared to DNS.

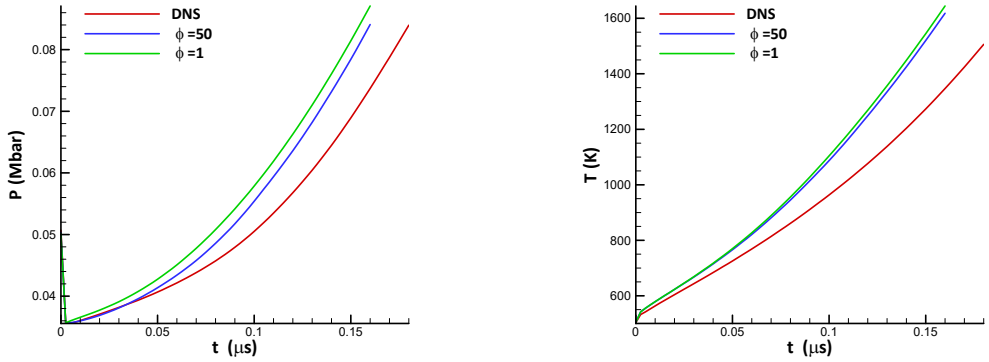

(a) Pressure (b) Temperature

Figure 5.6: Numerical results for First-Order Multiscale approach using resolution parameters $\phi = 50$ and $\phi = 1$. Results for $\eta = 0.75$ material system under C_2 loading conditions are compared to DNS.

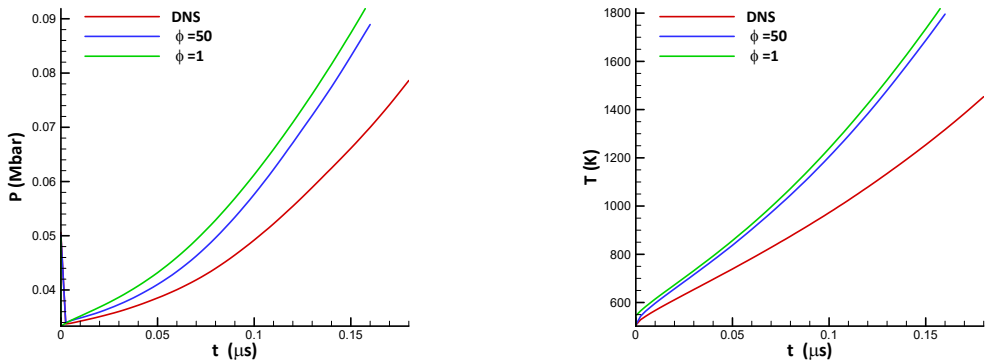

(a) Pressure (b) Temperature

Figure 5.7: Numerical results for First-Order Multiscale approach using resolution parameters $\phi = 50$ and $\phi = 1$. Results for $\eta = 0.75$ material system under B_y loading conditions are compared to DNS.

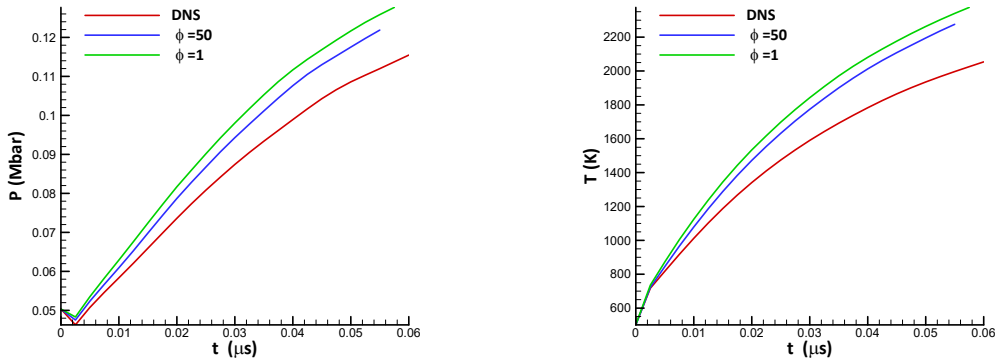

(a) Pressure (b) Temperature

Figure 5.8: Numerical results for First-Order Multiscale approach using resolution parameters $\phi = 50$ and $\phi = 1$. Results for $\eta = 0.75$ material system under R_m loading conditions are compared to DNS.

To further study this phenomenon, contour plots for pressure and temperature are shown on Figures 5.9(a) through 5.14(d) for the multiscale approaches and DNS. These results show the R_m loading condition from $t = 0.01 - 0.04\mu s$ in increments of $\Delta t_{plot} = 0.01\mu s$. Comparing the pressure contours for DNS and the multiscale approach using a resolution parameter of $\phi = 50$ it is observed that the responses are nearly identical within the first few plotted time steps. However the difference between both methodologies is apparent in

the final time step at $t_{plot} = 0.04\mu s$. Here both approaches produce peak pressures near the center of the domain close to $50GPa$. The main differences, though, can be seen in the cooler regions of the shocked explosive. Note, these regions are where the explosive has already been shocked, not where the material is still inert. For example by comparing the region and the upper left corner of the domain we can see that the material responses in both approaches are different in terms of pressure values. The DNS approach has smaller pressure values near $10GPa$ (shown in blue) while the multiscale approach also has low pressure values closer to $15GPa$. Similar regions like these exist throughout the explosive showing that shocked regions within DNS have lower pressure values than those from the multiscale approach, although peak pressures are similar.

When comparing the pressure contours between the multiscale methods, the difference is apparent within the first plotted time step. In general the pressure profile with the higher resolution parameter ($\phi = 50$) has higher pressure values (green) than the homogenized continuum(light blue). Comparing the final time step of $t_{plot} = 0.04\mu s$, shown on Figures 5.10(d) and 5.11(d) it is observed that the peak temperatures are different. While the multiscale model, with more micro structural information, has peak pressures near $50GPa$ the homogenized continuum has peak pressures closer to $45GPa$. However on average, according to Figure 5.8(a), the homogenized continuum has higher pressure values on average. Again this can be seen by comparing the upper left corner of the domain of both approaches. It is observed that higher pressure values are located in the homogenized continuum when compared to the multiscale model with a resolution parameter of $\phi = 50$.

Figures 5.12(a) through 5.14(d) show temperature contours for all approaches. Comparing all initial plotted time steps it is observed that the pressure profiles are non uniform. However by decreasing the resolution parameter the contour for the homogenized continuum shows near uniform pressure distributions. Again earlier conclusions show that hot spot mechanisms contribute to non uniform pressure distributions. Comparing the final plotted time step for all methods($t_{plot} = 0.04\mu s$) it is observed that the peak pressures are identical. However the amount of material that contains these peak pressures increases with decreasing resolution parameter ϕ; i.e. the homogenized continuum has more material with temperatures near or above $3000K$. The DNS approach shows that the average materials response is less reactive and produces a lower pressure and temperatures than the multiscale approach.

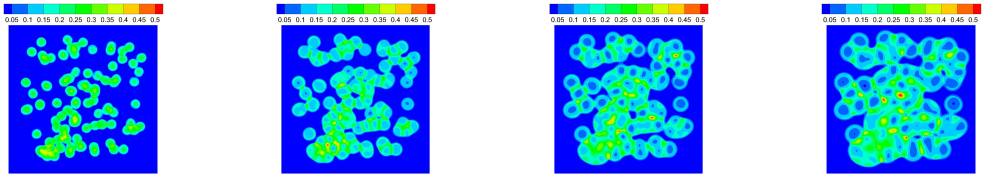

(a) t=0.01 (b) t=0.02 (c) t=0.03 (d) t=0.04

Figure 5.9: Pressure contours of $\eta = 0.75$ heterogeneous material under R_m loading conditions from $t = 0.010 - 0.014\mu s$. Results obtained using DNS.

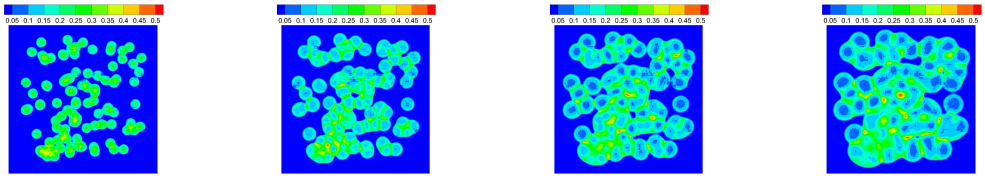

(a) t= 0.01 (b) t= 0.02 (c) t= 0.03 (d) t= 0.04

Figure 5.10: Pressure contours of $\eta = 0.75$ heterogeneous material system under R_m loading conditions from $t = 0.010 - 0.040\mu s$. Results obtained using multiscale method with $\phi = 50$

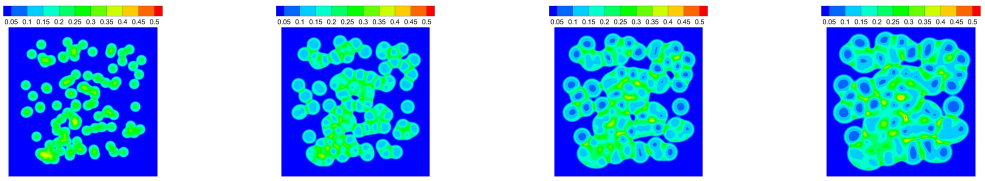

(a) t= 0.01 (b) t= 0.02 (c) t= 0.03 (d) t= 0.04

Figure 5.11: Pressure contours of $\eta = 0.75$ heterogeneous material system under R_m loading conditions from $t = 0.010 - 0.040\mu s$. Results obtained using multiscale method with $\phi = 1$

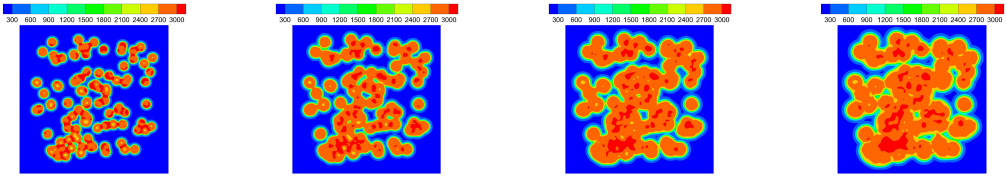

(a) t=0.01 (b) t=0.02 (c) t=0.03 (d) t=0.04

Figure 5.12: Temperature contours of $\eta = 0.75$ heterogeneous material under R_m loading conditions from $t = 0.010 - 0.040\mu s$. Results obtained using DNS.

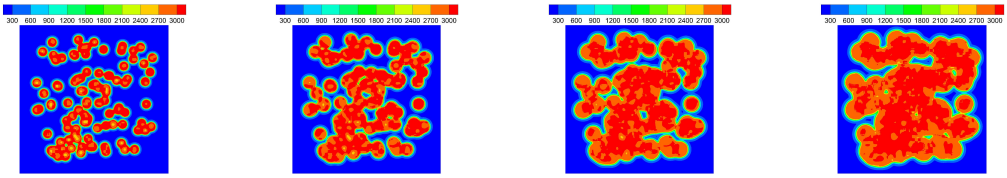

(a) t= 0.01 (b) t= 0.02 (c) t= 0.03 (d) t= 0.04

Figure 5.13: Temperature contours of $\eta = 0.75$ heterogeneous material system under R_m loading conditions from $t = 0.010 - 0.040\mu s$. Results obtained using multiscale method with $\phi = 50$

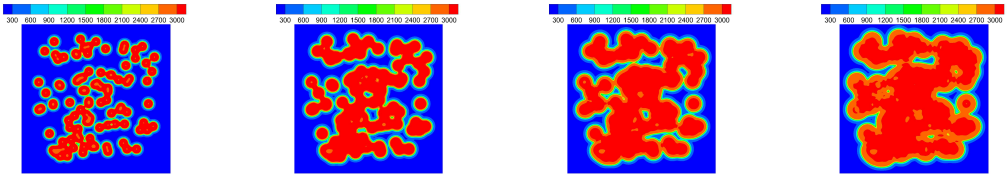

(a) t= 0.01 (b) t= 0.02 (c) t= 0.03 (d) t= 0.04

Figure 5.14: Temperature contours of $\eta = 0.75$ heterogeneous material system under R_m loading conditions from $t = 0.010 - 0.040\mu s$. Results obtained using multiscale method with $\phi = 1$

5.2.2 Numerical Results: $\eta = 0.85$, $\phi = 1, 50$

In this section numerical results from the multiscale approach are presented for shock loading on the heterogeneous material system with a HMX mass fraction of $\eta = 0.85$. Here, resolution parameters of $\phi = 50$ and $\phi = 1$ are considered. Figures 5.15(a)-5.18(b) show

pressure and temperature profiles for all loading conditions. Averages responses were obtained by integrating pressure and temperature contours over time. For the sake of brevity contour plots are not shown for any loading condition.

Figures 5.15(a) and 5.15(b) show pressure and temperature profiles for all for the C_1 loading condition. In general both plots show that the solutions follow similar trends. Figure 5.15(a) shows pressure as a function of time. Both methodologies originate from the initial average pressure of $P_{avg} = 5GPa$ and increase with time. Compared to the previous material system, it is observed that both methodologies are more tightly bound. By increasing HMX content from 75% to 85% this in general reduces material heterogeneity and explains the similarities in trends between both methodologies. This is also the reason why the solution parameter does not have as great an effect between the multiscale models. There is very little difference between the multiscale approaches. In fact when comparing the temperature profiles, as shown on Figure 5.15(b), the multiscale approaches align. This shows that for the 85% HMX content material system the microstructural information lost between $\phi = 50$ and $\phi = 1$ is negligible. However the differences in heterogeneity of the material between $\phi = 50$ and the DNS approach still plays a role as shown through the disparities between pressure and temperature profiles. Again the DNS approach produces lower pressure and temperature values for the given duration of the simulation.

Figures 5.16(a) and 5.16(b) show pressure and temperature profiles for the C_2 loading condition. Similar to the previous study, pressure and temperature profiles follow the similar trend where the gap between multiscale approaches and the gap between the multiscale approach and DNS approach closes due to the higher order of material homogeneity. The same conclusions are drawn for the B_y loading conditions shown in figure 5.17(a) and 5.17(b). In general pressure and temperature profiles for the DNS approach produce lower values than the multiscale approach, while the multiscale approaches align. Finally the R_m loading condition is studied on Figures 5.18(a) and 5.18(b). The same conclusions can be drawn from this previous study. Contour plots for this material system are not shown and will be shown for the following materials system to investigate the loss of material heterogeneity.

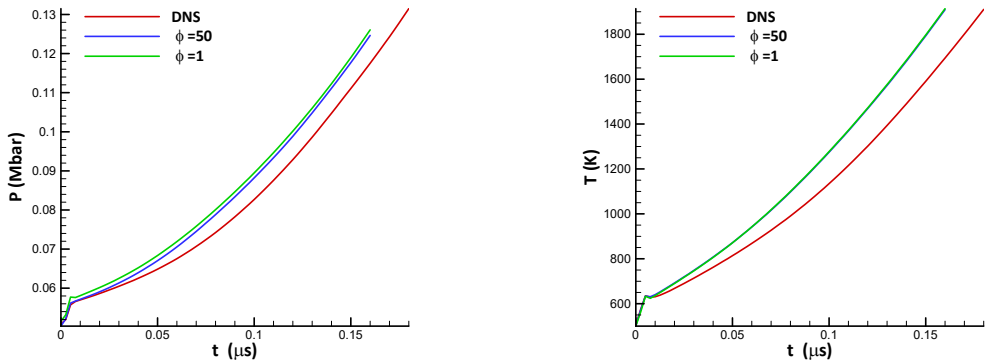

(a) Pressure (b) Temperature

Figure 5.15: Numerical results for First-Order Multiscale approach using resolution parameters $\phi = 50$ and $\phi = 1$. Results for $\eta = 0.85$ material system under C_1 loading conditions are compared to DNS.

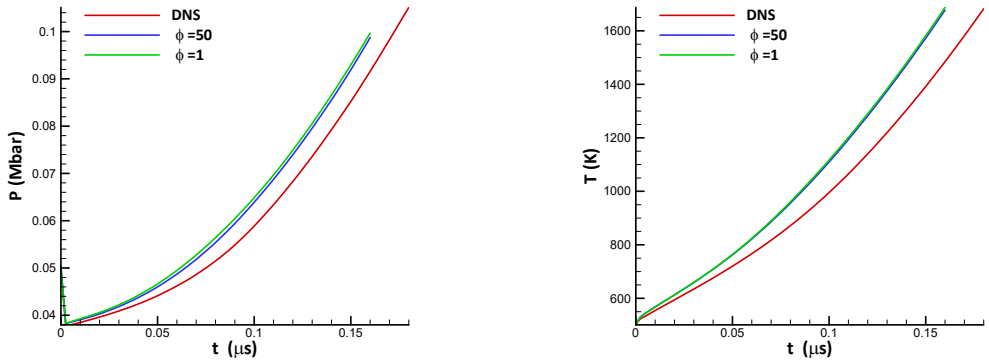

(a) Pressure (b) Temperature

Figure 5.16: Numerical results for First-Order Multiscale approach using resolution parameters $\phi = 50$ and $\phi = 1$. Results for $\eta = 0.85$ material system under C_2 loading conditions are compared to DNS.

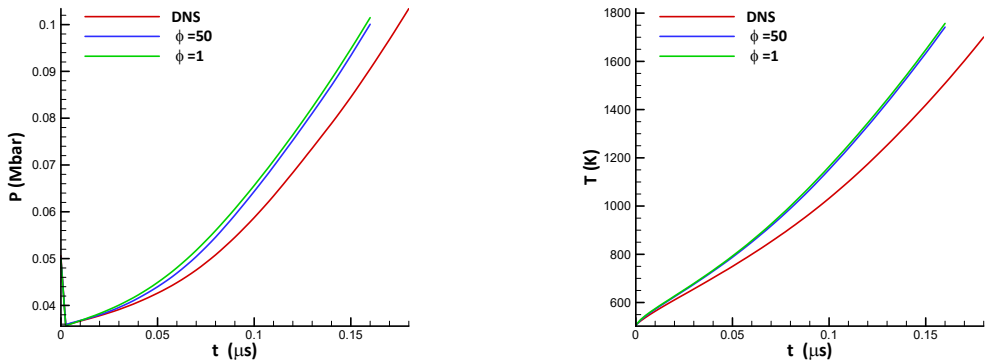

(a) Pressure (b) Temperature

Figure 5.17: Numerical results for First-Order Multiscale approach using resolution parameters $\phi = 50$ and $\phi = 1$. Results for $\eta = 0.85$ material system under B_y loading conditions are compared to DNS.

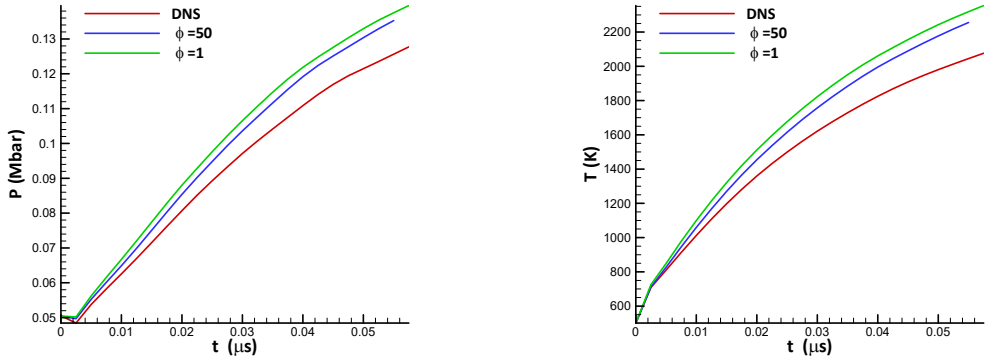

(a) Pressure (b) Temperature

Figure 5.18: Numerical results for First-Order Multiscale approach using resolution parameters $\phi = 50$ and $\phi = 1$. Results for $\eta = 0.85$ material system under R_m loading conditions are compared to DNS.

5.2.3 Numerical Results: $\eta = 0.95$, $\phi = 1, 50, 500$

In this section numerical results from the multiscale approach are presented for shock loading on the heterogeneous material system with a HMX mass fraction of $\eta = 0.95$. Here, resolution parameters of $\phi = 50$ and $\phi = 1$ are considered. Additionally, the resolution parameters of $\phi = 500$ is investigated for the random loading condition R_m. Figures

5.19(a)-5.22(b) show pressure and temperature profiles for all loading conditions. Averages responses were obtained by integrating pressure and temperature contours over time. For the sake of brevity contour plots are not shown for each loading condition.

Figures 5.19(a) and 5.19(b) show pressure and temperature profiles for all methodologies. Pressure is shown as a function of time in Figure 5.19(a). Here the multiscale approaches are nearly indistinguishable as they align throughout the duration of the simulation. Again this is attributed to the lack and heterogeneity in the material, as binder content is 5% of the material. This also affects the relationship between both approaches as the homogenized continuum is near the DNS approach. The gap between both methodologies again can be attributed to the loss of microscale information between both approaches. The same material behavior can be observed on the temperature plot, shown in Figure 5.19(b), where the multiscale plots are indistinguishable and the gap between the multiscale methodologies and DNS has closed. Comparing to the previous material systems, the 75% HMX content system had a larger disparity while the intermediate material system of 85% HMX content closed this gap. This material system further makes these approaches indistinguishable.

Figure 5.20(a) through 5.21(b) show numerical results for the C_2 and B_y loading conditions. Similar conclusions can be drawn from these experiments when compared to the first loading condition. The First-Order multiscale models are nearly indistinguishable while the gap between the multiscale approach and the DNS methodology has closed; however a gap still exists between these two approaches. To further investigate this gap, the resolution parameter of $\phi = 500$ is considered for the R_m loading condition.

These results are shown on Figure 5.22(a) and 5.22(b). Figure 5.22(a) shows the pressure profile as a function of time for all approaches including three multiscale models. Here, unlike the previous experiments, the homogenized continuum and the multiscale model with $\phi = 50$ do not align. Again this shows that loading conditions play a role in material response and that material heterogeneity is responsible for the behavior. For the previous loading conditions the material heterogeneity had no effect. Next, the resolution parameter is increased by an order of magnitude. By increasing the resolution parameter to match the size of the finite element mesh, it is observed that the response approaches the behavior of DNS. The gap between the $\phi = 500$ and $\phi = 50$ multiscale models is much smaller than the $\phi = 50$ and homogenized continuum($\phi = 1$). This shows that increasing microscale information by an order of magnitude does not always produce the same change in response; the inclusion of more information from the microscale provides little benefit. Although the gap between methodologies decreases, the multiscale model is never able to fully capture the results from the DNS approach. The same behavior can be seen in Figure

5.22(b) where temperature is plotted as a function of time. A gap still exists between multiscale models; however increasing the parameter ϕ by an order of magnitude provides no benefit to the multiscale model as the $\phi = 50$ results align with the $\phi = 500$ results. Again the gap between the homogenized continuum and the other multiscale models show that material heterogeneous plays a role for certain loading conditions.

To further study the material behavior under R_m loading, contour plots for each methodology, including the $\phi = 500$ multiscale model, are shown on Figures 5.23(a) through 5.30(d) for pressure and temperature. Comparing the pressure contours for each approach, it is observed that the profiles are nearly indistinguishable. The profiles at each time step are nearly identical between the DNS approach and the multiscale model.

All models produce localized hot regions near the center of the domain where pressure is near $50GPa$. Similarly the temperature contours shown on Figures 5.27(a) through 5.30(d) show similar material behavior for all approaches. Localized hot regions where temperatures exceed 3000 Kelvin are shown for the final plotted time step $t_{plot} = 0.04\mu s$. Here, the DNS approach produces less localized hot spots while the multiscale model in general produces more. The most localized hot regions are produced, again, by the homogenized continuum. This contributes to the overall material response where the DNS approach produces lower temperature output on average when compared to the multiscale methodologies.

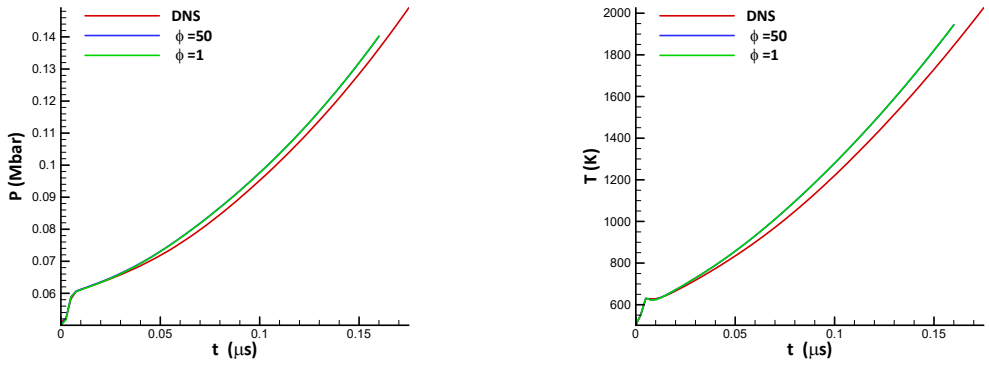

(a) Pressure

(b) Temperature

Figure 5.19: Numerical results for First-Order Multiscale approach using resolution parameters $\phi = 50$ and $\phi = 1$. Results for $\eta = 0.95$ material system under C_1 loading conditions are compared to DNS.

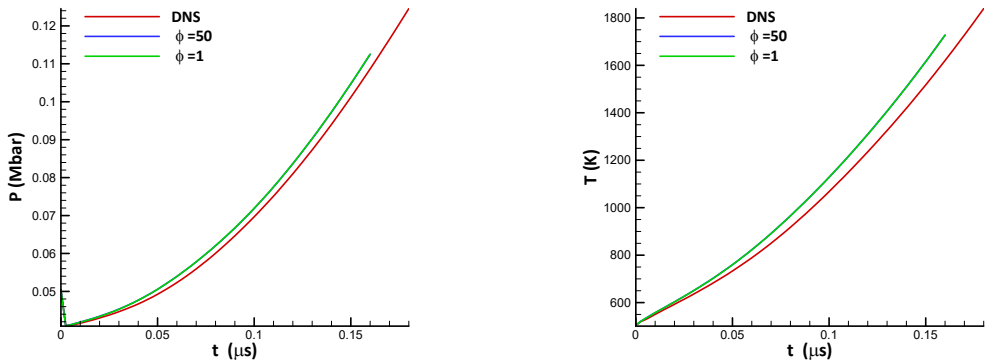

(a) Pressure (b) Temperature

Figure 5.20: Numerical results for First-Order Multiscale approach using resolution parameters $\phi = 50$ and $\phi = 1$. Results for $\eta = 0.95$ material system under C_2 loading conditions are compared to DNS.

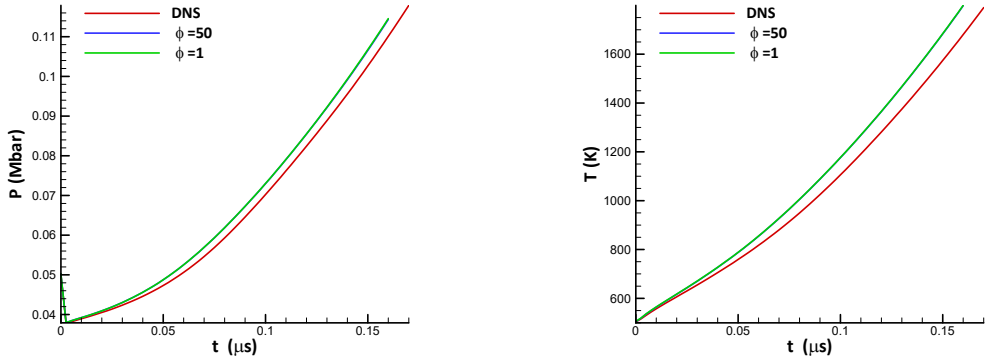

(a) Pressure (b) Temperature

Figure 5.21: Numerical results for First-Order Multiscale approach using resolution parameters $\phi = 50$ and $\phi = 1$. Results for $\eta = 0.95$ material system under B_y loading conditions are compared to DNS.

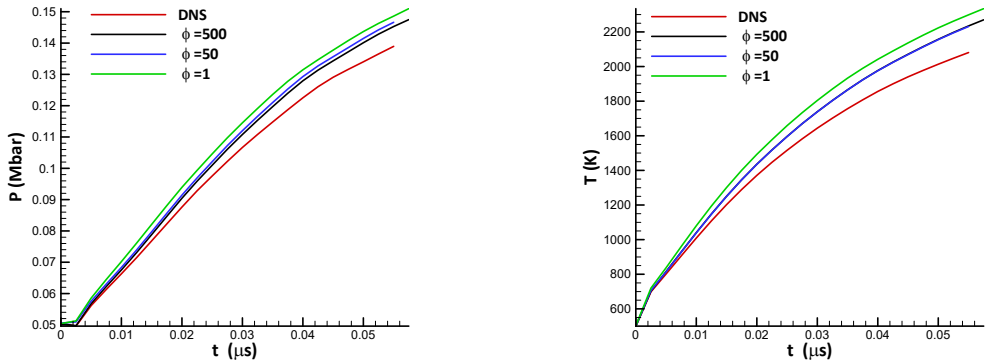

(a) Pressure (b) Temperature

Figure 5.22: Numerical results for First-Order Multiscale approach using resolution parameters $\phi = 50$ and $\phi = 1$. Results for $\eta = 0.95$ material system under R_m loading conditions are compared to DNS.

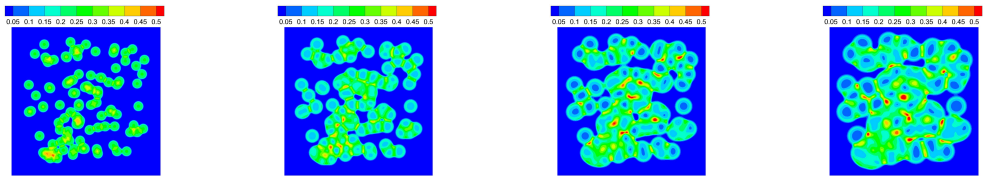

(a) t=0.01 (b) t=0.02 (c) t=0.03 (d) t=0.04

Figure 5.23: Pressure contours of $\eta = 0.95$ heterogeneous material under R_m loading conditions from $t = 0.010 - 0.040\mu s$. Results obtained using DNS.

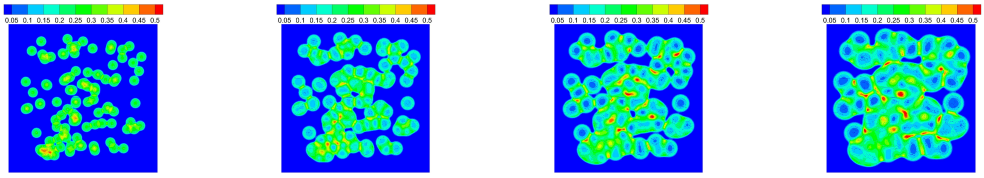

(a) t= 0.01 (b) t= 0.02 (c) t= 0.03 (d) t= 0.04

Figure 5.24: Pressure contours of $\eta = 0.95$ heterogeneous material system under R_m loading conditions from $t = 0.010 - 0.040\mu s$. Results obtained using multiscale method with $\phi = 500$

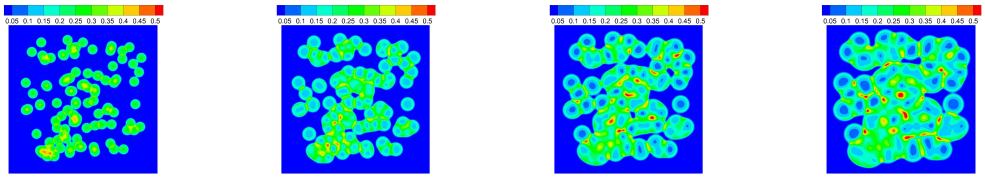

(a) t= 0.01 (b) t= 0.02 (c) t= 0.03 (d) t= 0.04

Figure 5.25: Pressure contours of $\eta = 0.95$ heterogeneous material system under R_m loading conditions from $t = 0.010 - 0.040\mu s$. Results obtained using multiscale method with $\phi = 50$

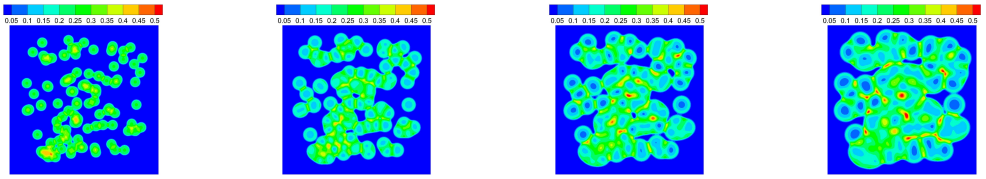

(a) t= 0.01 (b) t= 0.02 (c) t= 0.03 (d) t= 0.04

Figure 5.26: Pressure contours of $\eta = 0.95$ heterogeneous material system under R_m loading conditions from $t = 0.010 - 0.040\mu s$. Results obtained using multiscale method with $\phi = 1$

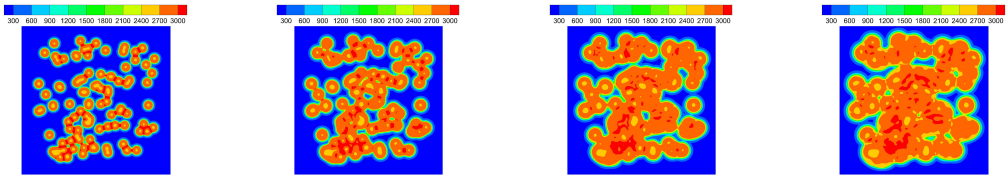

(a) t=0.01 (b) t=0.02 (c) t=0.03 (d) t=0.04

Figure 5.27: Temperature contours of $\eta = 0.95$ heterogeneous material under R_m loading conditions from $t = 0.010 - 0.040\mu s$. Results obtained using DNS.

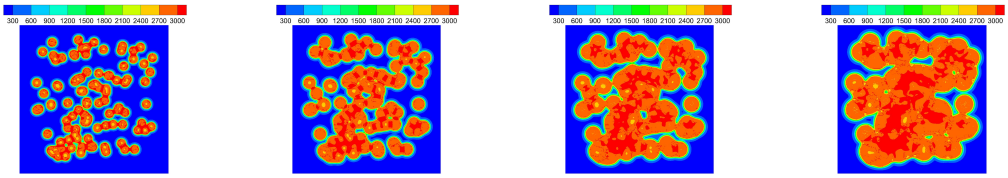

(a) t= 0.01 (b) t= 0.02 (c) t= 0.03 (d) t= 0.04

Figure 5.28: Temperature contours of $\eta = 0.95$ heterogeneous material system under R_m loading conditions from $t = 0.010 - 0.040s$. Results obtained using multiscale method with $\phi = 500$

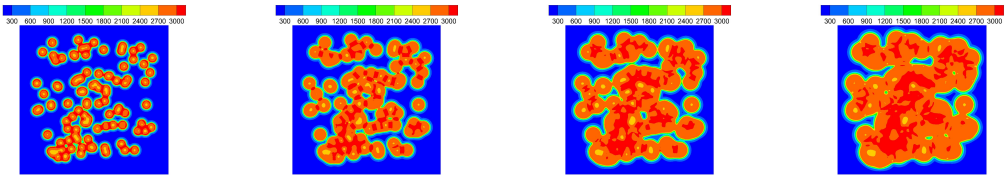

(a) t= 0.01 (b) t= 0.02 (c) t= 0.03 (d) t= 0.04

Figure 5.29: Temperature contours of $\eta = 0.95$ heterogeneous material system under R_m loading conditions from $t = 0.010 - 0.040\mu s$. Results obtained using multiscale method with $\phi = 50$

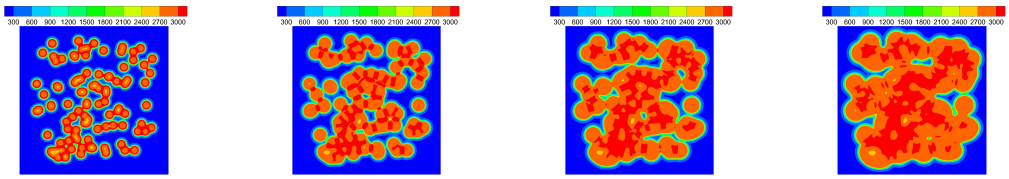

(a) t= 0.01 (b) t= 0.02 (c) t= 0.03 (d) t= 0.04

Figure 5.30: Temperature contours of $\eta = 0.95$ heterogeneous material system under R_m loading conditions from $t = 0.010 - 0.040\mu s$. Results obtained using multiscale method with $\phi = 1$

5.2.4 Numerical Results: All Material Systems

In this section, results from all material systems, loading conditions and methodologies are compared. Similar material behavior is observed using the First-Order approach when

compared to DNS; therefore, similar conclusions are drawn. Loading cases for heterogeneous material are a significant factor in responses especially where multiple hot spot interactions occur. Hot volume percentages do not necessarily correlate to performance. Increasing binder content decreases the sensitivity of the heterogeneous material. Material systems that require higher input energy per unit volume have the lowest performance in terms of pressure and temperature output showing a higher return on energy investment for HMX heavy content materials. Performance and safety is further investigated for each material using all methods. This is a continuation of the study performed in Section 4.3.4. Figures 5.31(a) and 5.31(b) show pressure and temperature as a function of initial average energy per unit volume. Here, the pressure and temperature values reported are for $t = 0.16\mu s$ for the C_1, C_2 and B_y loading conditions. For the much more volatile R_m loading condition the values reported are for $t = 0.05\mu s$. These plots give a "snap shot" of material performance, measured in pressure and temperature, and safety, measured in input average energy per unit volume. Note, there is not distinction between loading conditions on these plots. Similar to the previous study these plots show that performance and safety are at competition with each other, where the relationship is linear. HMX heavy materials have better performance than the materials with more binder content. However, these high performing material systems require much less initial energy per unit volume to reach these values, indicating that they are less safe. On the other side of the spectrum are materials with higher binder content. These material systems($\eta = 0.75$) require much more initial input energy per unit volume, indicating that accidental detonation is much less likely to occur. However their output pressures and temperatures are not as high as the HMX heavy materials. These results corroborate the results shown in the previous study. In general, it is better to over predict the response than under predict the response due to safety concerns.

To close out this Chapter, computational cost of each methodology is studied. As a summary, a 2D uniform mesh using 3-noded constant strain triangle elements, was used with a mesh density of $2,000ELM/cm$ and $251,001$ nodes. A constant time step of $\Delta t = 1e-5\mu s$ was used for a duration of $t = 0.16\mu s$. Computationally, the solution procedure for all results used 8 computational nodes with 16 cores each for a total number of 128 processes. The Direct Numerical Simulation (DNS) solution has 8 local degrees of freedom producing a global number of degrees of freedom of $2,008,008$. The continuum solution procedure described in Chapter 3 and the First-Order approach described in this chapter each have 5 local degrees of freedom. These methodologies have a global number of degrees of freedom is $1,255,005$. Computational cost is measure in terms of seconds per iteration and is shown on Figure 5.32. For the duration of $t = 0.16\mu s$, $16K$ iterations were required. The continuum approach, is the fastest method, while DNS requires more

computational power. The performances of the continuum approach and the multiscale approach compare favorably. The First-Order approach requires more computational time due to the averaging schemes; however, there differences are negligible when compared to DNS. The DNS approach requires significantly more time per iteration. This disparity is due to the $753,003$ difference in global degrees of freedom; this amount of fidelity is required to explicitly model the microstructure. In the context of numerical results, the multiscale approach agreed favorably with the DNS results. At worst, the material trend we followed, and at best they were nearly indistinguishable. This shows that heterogeneous material responses to shock loading can be captured using the multiscale approach at the fraction of the cost associated with DNS.

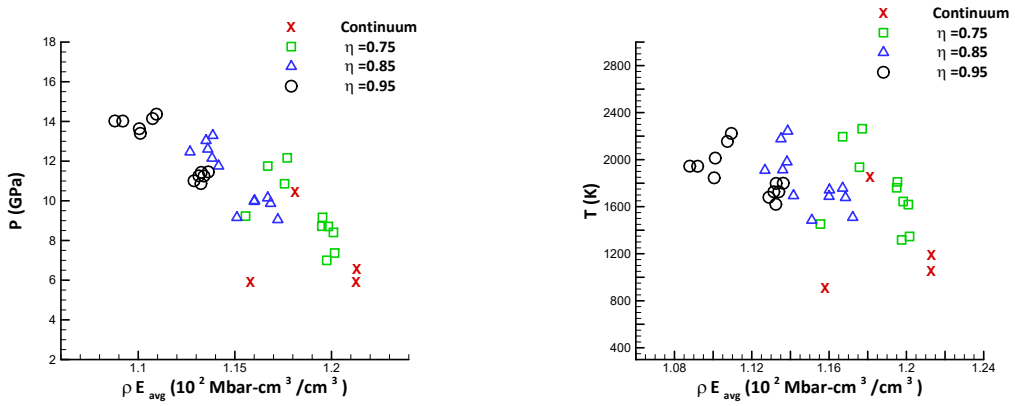

(a) Pressure

(b) Temperature

Figure 5.31: "Snap shot" of material performance, measured in pressure and temperature, and safety, measured in input average energy per unit volume for all material systems, using all methods. Performance and safety are at competition.

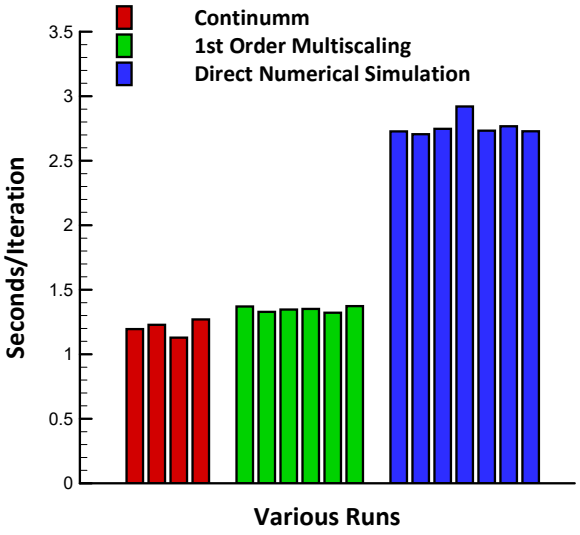

Figure 5.32: Computational cost for each methodology. DNS requires the most amount of computational power while the Continuum approach and the Multiscale model perform similarly.

5.3 Summary

This chapter presented First-Order Multiscale modeling of shock loading of polymer bonded explosives. These methods explicitly modeled material heterogeneities in the average sense using the resolution parameter ϕ. Essentially, this parameter describes material heterogeneity and represents information from the microscale. Resolution parameters of $\phi = 50$, a reduced order of magnitude from the finite element mesh and $\phi = 1$ were considered. The material system with $\phi = 1$ represented a homogenized continuum. Numerical results for all material systems and all loading conditions were presented and compared with results obtained via Direct Numerical Simulation (DNS). The DNS approach produces less localized hot spots while the multiscale model in general produces more. The most localized hot regions are produced by the homogenized continuum. This contributes to the overall material response where the DNS approach produces lower temperature output on average when compared to the multiscale methodologies. As the resolution parameter decreases among the multiscale approach, the material becomes more homogeneous and the response increases. On the other hand, increasing the resolution parameter, increases the material heterogeneity and the results are closer to the DNS approach which explicitly models than microstructure. Increasing HMX content among material systems reduces material hetero-

geneity and yields pressure and temperature trends that align within the multiscale models. Furthermore, these HMX heavy material systems close the gap between the multiscale approach and DNS. However, loading conditions still play a role in material response for all models. Performance versus safety results were investigated for all methodologies. HMX heavy materials have better performance than the materials with more binder content. However the benefits of binder are lost and safety of the material is compromised. The Chapter closes by investigating computational cost for each methodology. Heterogeneous material responses to shock loading can be captured using the multiscale approach at the fraction of the cost associated with DNS.